

FSI Methodology for Analyzing VIV on Subsea Pipeline Free Spans with Practical Boundary Conditions

A Thesis

Presented to

the Faculty of the Department of Mechanical Engineering Technology

University of Houston

In Partial Fulfillment

of the Requirements for the Degree

Masters of Science

in Engineering Technology

by

Marcus Aaron Gamino

July, 2013

FSI Methodology for Analyzing VIV on Subsea Pipeline Free Spans with Practical Boundary Conditions

Marcus Gamino

Approved:

Chairman of the Committee
Raymond E. Cline, Jr.
Associate Dean for Research and Graduate
Studies, College of Technology

Committee Members:

Co-Chairman of the Committee
Rares Pascali
Instructional Associate Professor
Mechanical Engineering Technology

Carlos Silva, Engineering Specialist
FMC Technologies

Alberto Rivas, Engineering Specialist
FMC Technologies

Raymond E. Cline, Jr. Associate
Dean for Research and Graduate
Studies, College of Technology

Heidar Malki,
Department Chair, Engineering Technology

Acknowledgements

Foremost, I would like to thank my family for their support. My deepest gratitude goes to my parents, F.C. and Ramona Gamino, for their support, encouragement and love throughout my educational pursuits.

Special thanks and appreciation must go to Dr. Marotta of FMC Technologies for his guidance throughout my research and for giving me the opportunity to work on this thesis with FMC Technologies' Multi-Physics Simulations Group. Additionally, I would like to thank Brad Maker of Simulia, Brian Donning of CD-adapco, and Dr. Florentina Popa of FMC Technologies for their technical support during my studies.

I do not forget to thank Professor Raresh Pascali. His guidance and encouragement helped me realize my potential.

Finally, thank you goes to my committee members, Dr. Ray Cline, Professor Raresh Pascali, Dr. Carlos Silva, and Dr. Alberto Rivas.

FSI Methodology for Analyzing VIV on Subsea Pipeline Free Spans with Practical Boundary Conditions

A Thesis

Presented to

the Faculty of the Department of Mechanical Engineering Technology

University of Houston

In Partial Fulfillment

of the Requirements for the Degree

Masters of Science

in Engineering Technology

by

Marcus Aaron Gamino

July, 2013

Abstract

The objective of this thesis is to develop a more realistic numerical model than current methodologies for free span stability of submarine pipelines based on fatigue analysis. A general assumption in performing vortex-induced vibration (VIV) analysis of pipeline free spans is that both ends of the free span are fixed and/or pinned in order to simplify computational simulations; however, Det Norske Veritas (DNV – translation to The Norwegian Truth) Recommended Practice F105 states that these boundary conditions must adequately represent the pipe-soil interaction and the continuity of the pipeline. To adequately simulate the free span's response to VIV, three-dimensional fluid-structure interaction (FSI) simulations are performed by coupling the computational fluid dynamics (CFD) codes from STAR-CCM+ with the finite element (FE) codes from ABAQUS. These FSI simulations in combination with separate coupled Eulerian-Lagrangian (CEL) simulations are modeled to mimic real world conditions by setting up the boundary conditions to factor in the effects of pipe-soil interaction at the ends of the span. Computational design of experiments (DOE) is utilized to determine the sensitivity of several input variables on the maximum stress response of the free span from VIV. The variables considered in this investigation include the soil density (1700-2000 kg/m³), length of pipe contact with the soil (20-200 inches), and the pipe embedment depth within the soil (0-10 inches). A Box-Behnken surface response design was used to capture the non-linear responses throughout the design space. These simulations show a mitigation of overall stresses to the free spans; as a result, the integration of pipe-soil

interaction in free span assessment may aid in the prevention of unnecessary corrective action.

Table of Contents

Acknowledgements.....	v
Abstract.....	v
1 Introduction.....	1
1.1 Focus of this Study.....	3
1.2 Assumptions.....	3
2.0 Background.....	4
2.1 Vortex-Induced Vibration.....	4
2.2 Review of Current Fatigue Assessment.....	5
3 Theory.....	8
3.1 FSI Governing Equations.....	8
3.2 Soil Plasticity Model.....	11
3.3 STAR-CCM+ Analysis of Von Karman Street.....	13
3.4 Benchmark Pipe-Soil Interaction Studies.....	24
4 Methodology.....	26
4.1 Free Span Data & Characteristics.....	28
4.2 Abaqus Modal Analysis.....	30
4.3 Screening.....	32
4.4 Fatigue Analysis.....	34
4.4.1 Fluid-Structure Interaction.....	34
4.4.1.1 Coupling of ABAQUS and STAR-CCM+.....	34
4.4.1.1.1 Implicit vs. Explicit Coupling.....	35
4.4.1.1.2 FSI Co-Simulation Setup.....	35
4.4.1.2 FSI Results.....	37
4.4.2 Integrating Pipe-Soil Interaction.....	38
4.4.2.1 Determining the Correct FE Model to Represent the Soil.....	39
4.4.2.2 The CEL Model.....	41
4.4.2.3 Computational Design of Experiments.....	43
5 Summary of Findings.....	47
5.1 DOE Screening Results.....	47
5.2 Findings from DOE Sensitivity Analysis.....	48
5.3 DOE Results.....	50

5.4 Fatigue	55
5.5 The Palmgren-Miner Rule	555
6 Conclusions.....	56
7 Recommendations and Future Work.....	577
References.....	59
VIV Vocab.....	Appendix A
VIV Equations and Definitions.....	Appendix B
Natural Frequency Results from ABAQUS.....	Appendix C
Final X, Y, and Z Displacement Data from FSI Simulations	Appendix D
Benchmark Pipe-Soil Interaction Procedure.....	Appendix E
Soil Sensitivity Studies	Appendix F
Free Span Sensitivity Studies.....	Appendix G
DOE Model Evaluation.....	Appendix H
Illustration of Input Ranges for Final Box-Behnken DOE	Appendix I
Detailed Final Box-Behnken DOE Results.....	Appendix J
Drained vs. Undrained Conditions of Soil	Appendix K
Validation of Soil Effects.....	Appendix L
Limitations of the Mohr-Coulomb Model	Appendix M

List of Figures

Figure 1.1 Function Structure	2
Figure 2.1 Velocity Vector Plot Depicting VIV	5
Figure 2.2 Line Model of Free Span on a Rigid Seabed (Cherif 2008)	7
Figure 3.1 Mohr-Coulomb Model.....	12
Figure 3.2 Sketch of the Physical Uniform flow and the Location of the Cylinder's Wake	14
Figure 3.3 The Modeling of the Wake at Different Reynolds Numbers.....	15
Figure 3.4 Sketch of Geometry Scene Created in STAR-CCM+	16
Figure 3.5 Tetrahedral Mesh Scene in STAR-CCM+ (5739 cells, 8535 faces)	17
Figure 3.6 Velocity Vector Scene of $Re = 30$	19
Figure 3.7 Velocity Vector Scene of $Re = 75$	20
Figure 3.8 Velocity Vector Scene of $Re = 200$	22
Figure 3.9 Velocity Vector Scene of $Re = 1000$	24
Figure 3.10 Pipe-Soil Interaction Representation with CEL	25
Figure 4.1 Flow Chart over Design Checks for a Free Span (DNV-RP-F105)	28
Figure 4.2 Visualization of Free Span for FSI and CEL Simulations.....	29
Figure 4.3 Mode-1 Shape for Free Span Model – Isometric View	31
Figure 4.4 In-line VIV Response Amplitude versus V_R and K_S (DNV-RP-F105).....	33
Figure 4.5 Maximum Displacement Results from FSI	37
Figure 4.6 Principle Stress vs. Time History for 2 Seconds Physical Time	38
Figure 4.7 Mimic of Von Mises Stress vs. Time History for 2 Seconds Physical Time	39
Figure 4.8 Distorted Mesh Failure with Soil Modeled with ALE Methods.....	41
Figure 4.9 Pipe-Soil Interaction Representation with CEL	41
Figure 4.10 CEL FE Free Span Model Setup	42
Figure 4.11 Comparison of Different 620 inch Pipe Cases	43
Figure 4.12 Location of the Design Points for the Box-Behnken Design (itl.nist.gov).....	45
Figure 4.13 Box-Behnken Design Space Setup	46
Figure 5.1 Screening Results from Commercial Software.....	48
Figure 5.2 Stress Results at Different Pipe Embedment	49
Figure 5.3 Stress Results at Different Pipe-Soil Contact Lengths	50

Figure 5.4 Box-Behnken Stress Estimates at the Corners.....	51
Figure 5.5 Prediction Profiler	52
Figure 5.6 Stress vs. Time Graph for Maximum Desirability.....	53
Figure 5.7 Interaction Profiles	54
Figure 7.1 Internal Slug Flow within a Subsea Pipeline.....	58

List of Tables

Table 2.1 Comparison of Different Methods to Model the Pipeline Free Span.....	7
Table 3.1 Physics Values and Parameters of $Re = 30$	18
Table 3.2 Physics Values and Parameters of $Re = 75$	19
Table 3.3 Physics Values and Parameters of $Re = 200$	22
Table 3.4 Physics Values and Parameters of $Re = 1000$	23
Table 4.1 Carbon Steel X65 Properties.....	29
Table 4.2 Free Span Natural Frequencies	31
Table 4.3 FSI Mesh Sensitivity Results	36
Table 4.4 Advantages and Disadvantages for Each Computational DOE Model.....	44
Table 4.5 Inputs for the Box-Behnken.....	46

1 Introduction

The phenomenon of vortex-induced vibration (VIV) continues to be a major interest of study in the design of subsea piping components. VIV arises when free vibration of the structure occurs due to the vortices that develop behind the structure. Alternating vortex shedding is responsible for oscillatory forces that generate structural vibrations (Blevins 1990). This free vibration is a major concern in fatigue analysis of subsea piping components including free spans of pipelines, which are subsea pipeline sections not supported by the seabed.

The oil and gas industry has great concerns on how VIV affects the fatigue life of subsea pipeline free spans. When corrective action is necessary to prevent fatigue damage for free spans, large amounts of resources are used to stabilize spans with rock damping, installation of mattresses, and the installation of grout bags (Palmer 2008).

Past studies have utilized analytical, experimental, and computational methods to study the VIV effects on subsea piping components. To increase simplicity of the models, researchers tend to impose fixed and/or pinned boundary conditions at the ends of the geometry. Although, Det Norske Veritas (DNV – translation to The Norwegian Truth) code approves the use of fixed and/or pinned connections in free span analysis, a more realistic model is necessary to represent the pipe-soil interaction and the continuity of the pipeline in order to achieve an optimal design.

In this thesis, a more realistic model for free span stability is developed by combining FSI and CEL modeling to determine the effects of pipe-soil interaction at the ends of the free span. This approach utilizes the FSI methodology discussed in Chica

(2012), where the FEA codes of ABAQUS are coupled with the CFD codes of STAR-CCM+, to be able to determine the stresses and displacements of free spans over time.

Once the load amplitude from the underwater current is determined from FSI modeling, CEL modeling is utilized to observe the interactions at the ends of the free span with the soil. Design of experiments (DOE) is utilized to determine the stress responses to different pipe embedment, various amounts of soil modeled, and different soil densities. The scope of this thesis is defined in a function structure (Figure 1.1), which takes a need and breaks this need down to lower functions. Figure 1.1 illustrates the breakdown of the scope of work for this thesis.

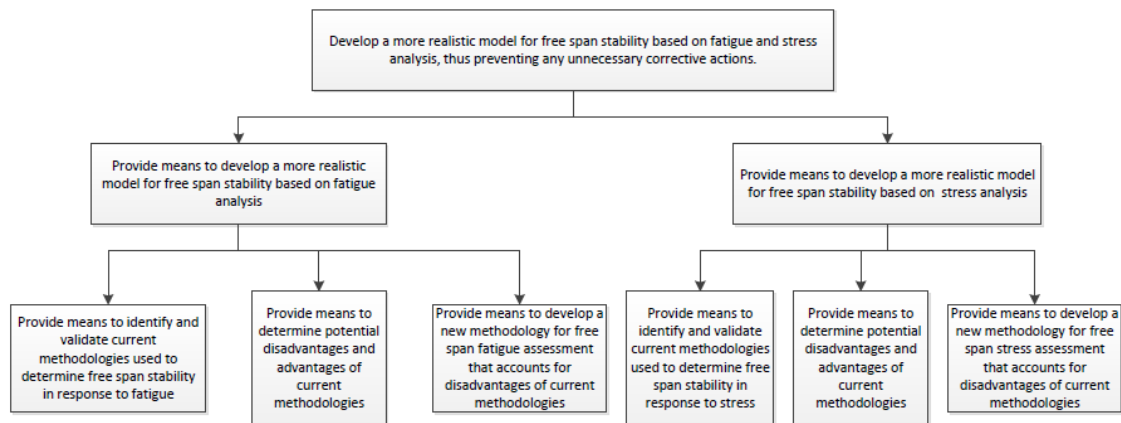


Figure 1.1 Function Structure

The purpose of this thesis is to provide means to develop a more realistic numerical model than current methodologies for free span stability of submarine pipelines based on fatigue analysis. This will be done by using commercial FE and CFD codes to determine the dampening effects from the pipe-soil interaction at the ends of a free span undergoing oscillation due to VIV. This thesis discusses the setup of the FSI

and CEL simulations, a methodology to incorporate pipe-soil interaction in free span analysis, and conclusions drawn.

1.1 Objective

The objective of this thesis is to provide means to develop a more realistic numerical model than current methodologies for free span stability of submarine pipelines based on fatigue analysis. This will be done by coupling the computational fluid dynamics (CFD) codes from STAR-CCM+ with the finite element analysis (FEA) codes from ABAQUS. These FSI simulations in combination with separate coupled Eulerian-Lagrangian (CEL) simulations are modeled to mimic real world conditions by setting up the boundary conditions to factor in the effects of pipe-soil interaction at the ends of the span.

The difficulty with free span assessment is the uncertainty. According to Wang, span analysis can be “challenging when soil uncertainty, concrete degradation, and unknown residual lay tension are considered in the analysis” (1). Although soil uncertainty was addressed in this thesis, other assumptions are made to simplify the finite element models.

1.2 Assumptions

Assumptions within the FSI and CEL analyses of this thesis include: single mode response, VIV dependent solely on underwater current, uniform current flow, no effect from underneath seabed distance to free span (i.e. no seabed under the free span exists in the simulations), axial tension has no effect on the natural frequency of the pipeline, an empty pipeline with no coatings, no marine growth, and even seabed topology.

Before the methodology discussing the development of a more realistic model for free span assessment is revealed, the following sections will discuss the background and theory behind free spans, soil, and vortex-induced vibration. All conclusions and future work are discussed after all findings from the FSI and CEL simulations and design of experiments (DOE) are listed.

2.0 Background

Two causes of fatigue damage to subsea pipeline free spans exist: waves and underwater current. Ideally, fatigue assessment models should account for the vibration of span due to both waves and underwater current. However, only VIV from underwater current will be investigated in this thesis due to the assumption that waves have no effect on the free span one-hundred meters or more below sea level.

2.1 Vortex-Induced Vibration

As previously noted, the phenomenon of VIV arises when the alternating vortices develop and shed past the body. The primary reason for the formation of these vortices is the frictional shear stress arising within the boundary layer, which is “a very thin layer in the neighborhood of the body” (Schlichting 1968). This phenomenon of alternating vortex shedding is depicted in a two-dimensional plane as shown in Figure 2.1.

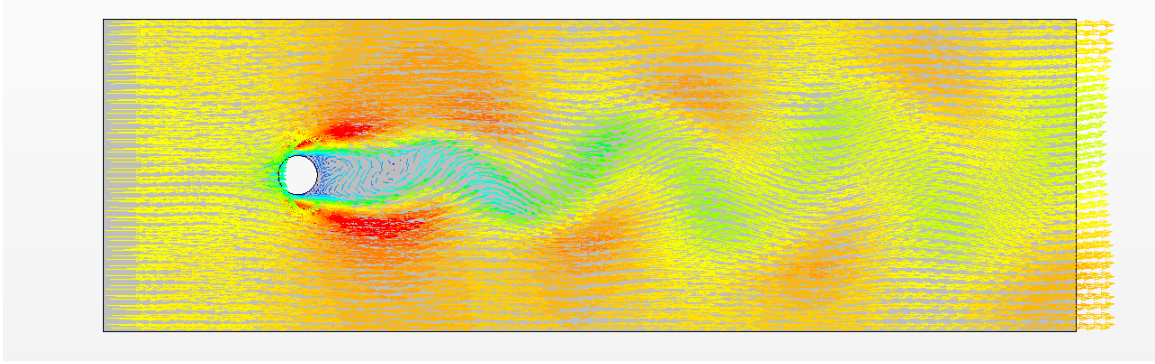


Figure 2.1 Velocity Vector Plot Depicting VIV

The vortices that develop past the cylinder produce a vortex shedding frequency (i.e. a frequency at which the vortices shed from the cylinder). If this frequency is close to the natural frequency of the body, maximum displacement of the body due to VIV occurs, which is also known as resonance (Blevins 1990). Current fatigue assessments utilize finite element models to determine what conditions will induce resonance.

2.2 Review of Current Fatigue Assessment

Current fatigue assessments of pipeline free spans are based upon internationally accepted codes (e.g. DNV-RP-F105). Within these codes, assumptions are made. For example, boundary coefficients are assumed based on fixed or pinned boundary conditions for fatigue assessment calculations within response models. According to DNV-RP-F105, these response models use empirical relations to derive a stress response from an assumed vibration mode (10). These and other conservative assumptions are made to ensure calculations based on response models do not overestimate fatigue life and to compensate for the limitations of these analyses.

The boundary coefficients used in these analyses have limitations, for they can only be used “under the assumption of small displacements and an isolated, single span on [the] seabed” (33). Unless more detailed empirical relations are derived by means of observation or expensive experimentation, another method must be developed to account for more complex situations. Furthermore, new methods can be developed to validate conservative assumptions made in response models.

Computational fluid dynamics (CFD) is presented as another option within DNV-RP-F105 as an alternative to response models. CFD simulations can be “applied for VIV assessment to overcome the inherent limitations of the state-of-practice engineering approach” (10).

State of the art techniques in CFD and FEA will be employed to develop a numerical model that limits conservative assumptions and overcomes limitations of current methodologies. The primary assumption investigated within this thesis is the boundary conditions listed in DNV-RP-F105 for free span fatigue assessment, which allows for the assumption of fixed-fixed or fixed-pinned boundary conditions in free span assessment.

Currently, documented work is lacking in integrating pipe-soil interaction at the boundary conditions in free span VIV assessment. However, the modeling of the seabed within finite element models is not a new practice. Previous analyses in strength assessment have modeled the seabed as rigid surface to determine stress response to the pipeline’s own submerged weight. According to Palmer (2008), traditional stability

design methods treat the seabed stationary and immovable. Figure 2.2 illustrates a case where the pipeline free span is modeled as a line model on a rigid seabed.

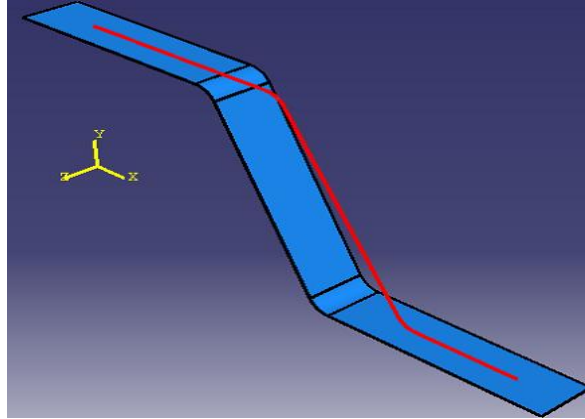


Figure 2.2 Line Model of Free Span on a Rigid Seabed (Cherif 2008)

In the case of Figure 2.2, a line model is utilized to model the span to more quickly compute stress responses. Table 2.1 details the advantages and disadvantages of different types of pipeline free span models.

Table 2.1 Comparison of Different Methods to Model the Pipeline Free Span

Type of Model	Advantages	Disadvantages
Line Model	<ul style="list-style-type: none"> • Fastest Computational Time versus Shell and Solid model 	<ul style="list-style-type: none"> • Only gives the average stress values along the length of the free span
Shell Model	<ul style="list-style-type: none"> • Able to visualize the difference in stress values along the circumference of the pipeline • Faster Computational Time versus the Solid model 	<ul style="list-style-type: none"> • Slower Computational Time versus the Line model • Cannot determine the stress values throughout the thickness of the pipeline
Solid Model	<ul style="list-style-type: none"> • Able to ascertain the entire stress tensor at all locations across the thickness and along the pipe circumference 	<ul style="list-style-type: none"> • Slowest Computational Time versus Line and Shell Model

Although a rigid surface is sufficient in representing the seabed in free span strength assessment, it cannot be utilized model the effects of soil degradation or conditions where the ends of the span are embedded within the soil.

To more adequately model the pipeline free span, the FEA and CFD simulations analyzed in this thesis will model the free span as an elastic solid and the soil as an Eulerian mesh capable of deforming in response to the vibration of the free span.

3 Theory

Analyzing VIV requires the fundamental equations of solid and fluid mechanics to be solved. When using CEL to model soil behavior within the commercial software ABAQUS, a full understanding plasticity theory is also essential. To ensure proper response from the software, benchmark CFD and CEL analyses were performed.

3.1 FSI Governing Equations

Finite element analysis and computational fluid dynamics must adhere to fundamental equations of elasticity theory and fluid mechanics respectively. This thesis examines these fundamental equations briefly to establish a base of FEA and CFD.

According to Newton's 2nd Law, the sum of all forces acting on a body equals the body's mass times its acceleration. In the absence of acceleration, the sum of all forces acting on a body must be zero, so equilibrium is achieved. The following set of equations summarizes the previous statement:

$$\frac{\partial \sigma_x}{\partial x} + \frac{\partial \tau_{xy}}{\partial y} + \frac{\partial \tau_{xz}}{\partial z} + X_b = 0$$

$$\frac{\partial \tau_{xy}}{\partial x} + \frac{\partial \sigma_y}{\partial y} + \frac{\partial \tau_{yz}}{\partial z} + Y_b = 0$$

$$\frac{\partial \tau_{xz}}{\partial x} + \frac{\partial \tau_{yz}}{\partial y} + \frac{\partial \sigma_z}{\partial z} + Z_b = 0$$

where σ is the normal stress, τ is the shear stress, X_b , Y_b , and Z_b are body forces in units of force per unit volume.

When an object under a load deforms, strain energy develops. Strain energy is potential energy created within an object as a result of a load deforming the object. Strain energy may also be viewed as the area under the load-deflection curve.

$$U = \int_L (P)(\Delta d)$$

Energy must be conserved in solid mechanics. FEA packages use energy to track convergence. For example, ABAQUS monitors the total energy of the system while the simulation is running. If the total energy does not differ by orders of magnitude from one time step to another, the solution is converging.

In addition to monitoring the physics, STAR-CCM+, the CFD software, monitors residuals as one indicator for convergence. If the residuals of the continuity equations approach zero, this usually means the solution is converging. Even though these residuals may approach zero, analysts must ensure the solution adheres to the fundamental laws of nature.

The fundamental equations describing the behavior of fluids include the conservation of mass, conservation of energy, and conservation of momentum.

Conservation of mass:

$$\frac{\partial \rho}{\partial t} + \nabla(\rho V) = 0$$

where ρ is density, V is the fluid velocity vector field, and ∇ is divergence of the velocity

vector and is defined as: $\nabla = \frac{\partial}{\partial x} \mathbf{i} + \frac{\partial}{\partial y} \mathbf{j} + \frac{\partial}{\partial z} \mathbf{k}$

Conservation of momentum:

$$\text{X Component: } \frac{\partial(\rho u)}{\partial t} + \nabla(\rho u V) = -\frac{\partial p}{\partial x} + \frac{\partial \tau_{xx}}{\partial x} + \frac{\partial \tau_{xy}}{\partial y} + \frac{\partial \tau_{zx}}{\partial z} + \rho f_x$$

$$\text{Y Component: } \frac{\partial(\rho v)}{\partial t} + \nabla(\rho v V) = -\frac{\partial p}{\partial y} + \frac{\partial \tau_{xy}}{\partial x} + \frac{\partial \tau_{yy}}{\partial y} + \frac{\partial \tau_{zy}}{\partial z} + \rho f_y$$

$$\text{Z Component: } \frac{\partial(\rho w)}{\partial t} + \nabla(\rho w V) = -\frac{\partial p}{\partial z} + \frac{\partial \tau_{xz}}{\partial x} + \frac{\partial \tau_{yz}}{\partial y} + \frac{\partial \tau_{zz}}{\partial z} + \rho f_z$$

where p is pressure, u , v , and w are the velocity components in x , y , and z direction

respectively, τ is the stress tensor, and f is other body forces.

Conservation of Energy:

$$\begin{aligned} & \frac{\partial}{\partial t} \left[\rho \left(e + \frac{V^2}{2} \right) \right] + \nabla \left[\rho \left(e + \frac{V^2}{2} \right) V \right] \\ &= \rho q + \frac{\partial}{\partial x} \left(k \frac{\partial T}{\partial x} \right) + \frac{\partial}{\partial y} \left(k \frac{\partial T}{\partial y} \right) + \frac{\partial}{\partial z} \left(k \frac{\partial T}{\partial z} \right) - \frac{\partial(u p)}{\partial x} - \frac{\partial(v p)}{\partial y} - \frac{\partial(w p)}{\partial z} \\ &+ \frac{\partial(u \tau_{xx})}{\partial x} + \frac{\partial(u \tau_{yx})}{\partial y} + \frac{\partial(u \tau_{zx})}{\partial z} + \frac{\partial(v \tau_{xy})}{\partial x} + \frac{\partial(v \tau_{yy})}{\partial y} + \frac{\partial(v \tau_{zy})}{\partial z} \\ &+ \frac{\partial(w \tau_{xz})}{\partial x} + \frac{\partial(w \tau_{yz})}{\partial y} + \frac{\partial(w \tau_{zz})}{\partial z} + \rho f V \end{aligned}$$

Additionally, $e + \frac{V^2}{2}$ is thermodynamic internal energy, q is heat flux, k is the thermal

conductivity, and T is temperature.

When solving the fundamental equations of fluid mechanics, STAR-CCM+ uses an iterative process. The residuals of this iterative process are displayed during the solution, so analysts may observe if the problem is converging or diverging.

3.2 Soil Plasticity Model

In general terms, a material plastically deforms when it passes its yield stress limit. Before reaching its yield stress, the material elastically deforms (i.e. its strain response increases linearly as the applied stress increases). When a material elastically deforms it follows a linear relationship known as Hooke's Law:

$$\sigma = E * \epsilon$$

where:

E = the modulus of elasticity of the material

ϵ = the strain response of the material due to the stress applied

Soils do not deform elastically; therefore, a plasticity model must be used in the finite element models to adequately model soil response. Abaqus uses the Mohr-Coulomb model to determine yield, which “assumes that yield occurs when the shear stress on any point on a material reaches a value that depends linearly on the normal stress in the same plane” (ABAQUS 2007). Figure 3.1 illustrates the linear relationship between the shear stress and its dependence on the normal stress.

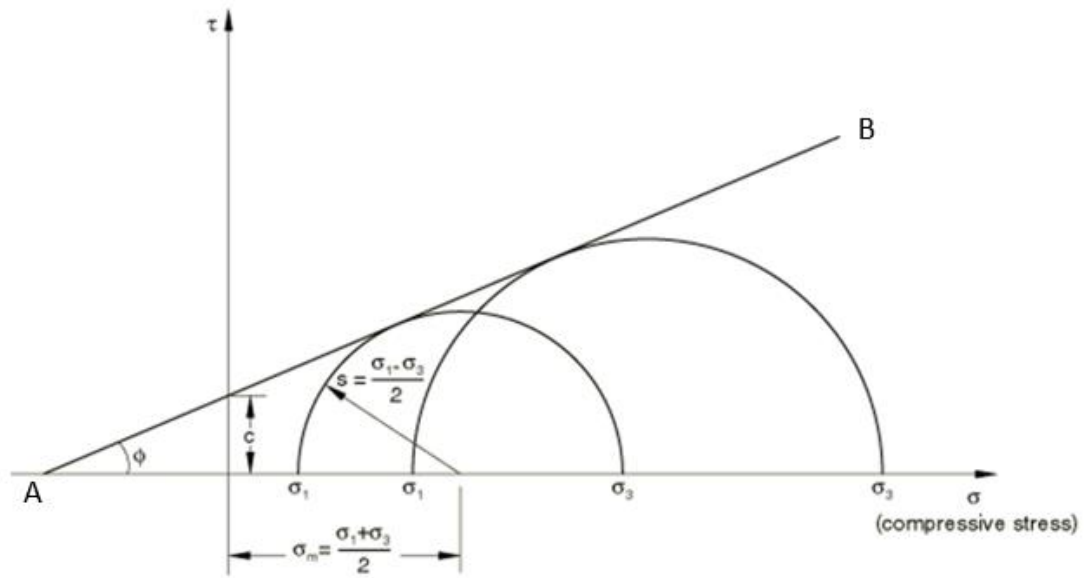


Figure 3.1 Mohr-Coulomb Model

A mathematical formula can be used to visualize the relationship between the soil shear strength and the applied compressive stress in the Mohr-Coulomb failure criterion.

$$\tau = c + \sigma \tan \phi$$

where:

- τ_f is the soil shear strength, which is the “shear resistance offered by the soil to overcome applied shear stresses” (Helwany 2007).
- c is the cohesion intercept of the soil
- σ is the applied normal effective stress
- ϕ is the internal friction angle of the soil

This above equation represents the yield curve (i.e. line AB in Figure 3.1) as a function of cohesion and angle of friction. The region of elasticity is below the yield curve. ABAQUS allows the user to directly manipulate the cohesion value and the angle of friction in the Mohr- Coulomb model. Additionally, ABAQUS gives the user the option to input a dilation angle, and the option is present to input a value for absolute plastic strain as a function of cohesion values, temperature, or a different variable. The dilation angle represents a change in volume (i.e. volumetric strain) as a result of shear loading. For clays, little to no dilation is present due to the undrained state of clay, so a value of zero can be used to represent the dilation angle, which means volume of soil is preserved throughout the simulations (PLAXIS GiC). Clays produce undrained conditions due to its ability to trap fluid while undergoing loading, and sands mimic drained conditions due to its permeability. Further information about the drained and undrained conditions of soil can be found in appendix K.

The Mohr-Coulomb model will be used to represent the soil in the CEL simulations analyzed in this thesis.

3.3 STAR-CCM+ Analysis of Von Karman Street

Numerous numerical and empirical methods have been studied in the analysis of uniform flow past a rigid 2D cylinder. One of the parameters engineers study is the formation of vortices behind the cylinders wake, which is illustrated in Figure 3.2.

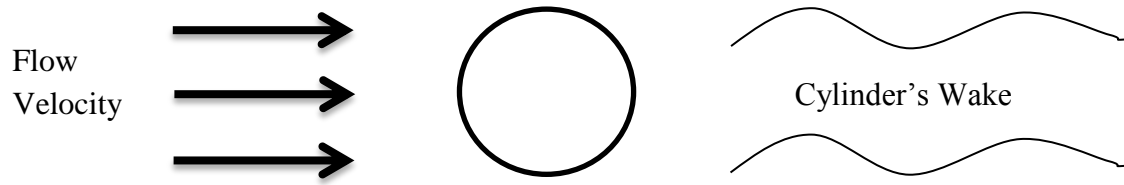


Figure 3.2 Sketch of the Physical Uniform flow and the Location of the Cylinder's Wake

Reynolds number (Re) is a non-dimensional parameter that greatly effects the development of vortexes behind bluff bodies. The value of Reynolds number depends on the velocity of the current (U), the outside diameter of structure (D), and the kinematic viscosity of the fluid (ν) according to Blevins (1990).

$$\text{Reynolds Number (Re)} = \frac{UD}{\nu} = \frac{\text{inertial force}}{\text{viscous force}}$$

As the Reynolds number increases, flow around and behind the cylinder undergoes tremendous changes. Reynolds number and other VIV vocabulary and equations are highlighted in Appendix A and B respectively.

When the Reynolds number is below five, the viscous forces dominate, and no separation occurs behind the cylinder as shown in Figure 3.3

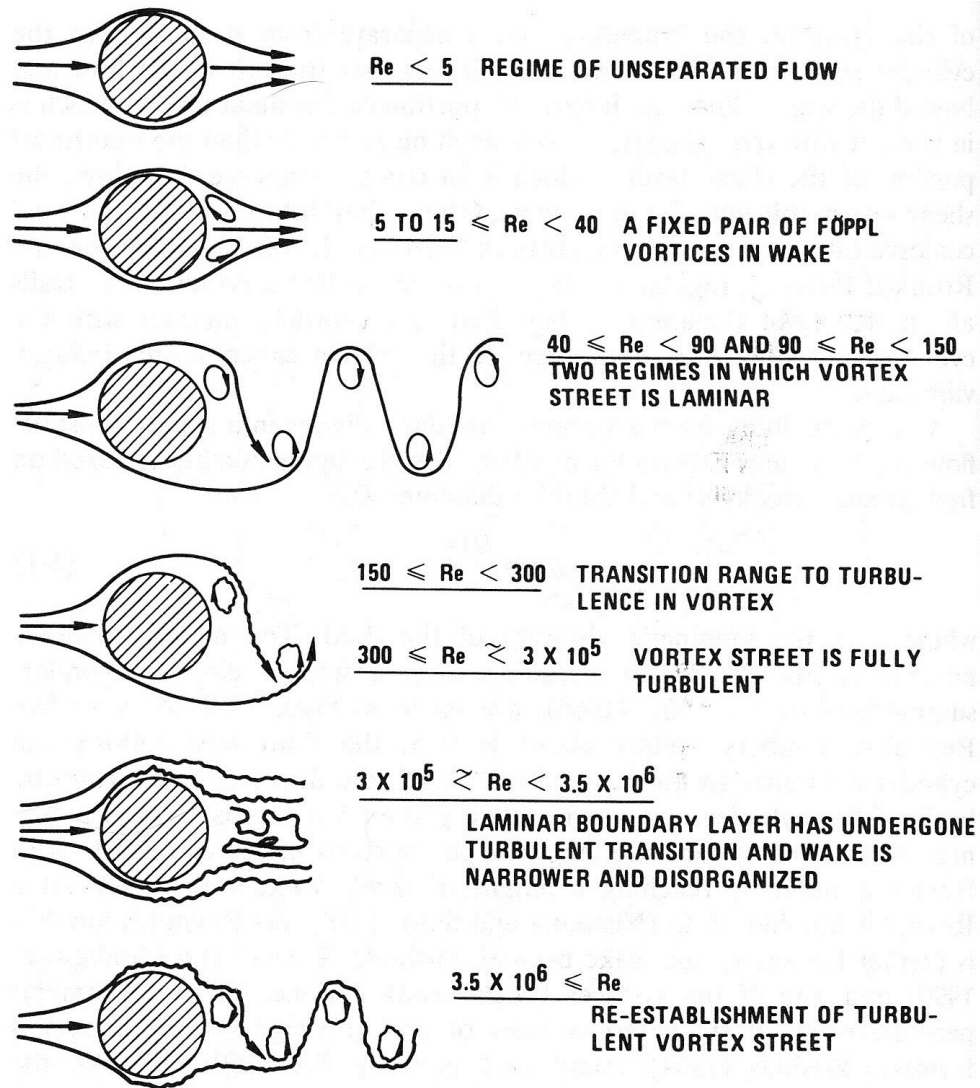


Figure 3.3 The Modeling of the Wake at Different Reynolds Numbers (Lienhard, 1966)

As the Reynolds number increases past five, fixed pair of symmetric vortices develop behind the cylinder, while the cylinder's boundary and wake remain laminar.

As a benchmark, 2D computational simulations were created with STAR-CCM+ to model flow past a rigid cylinder at different Reynolds numbers.

The first simulation modeled flow past the rigid cylinder at a Reynolds number of 30, which a pair of fixed symmetric vortices should form. Figure 3.4 represents the geometry scene created in STAR-CCM+.

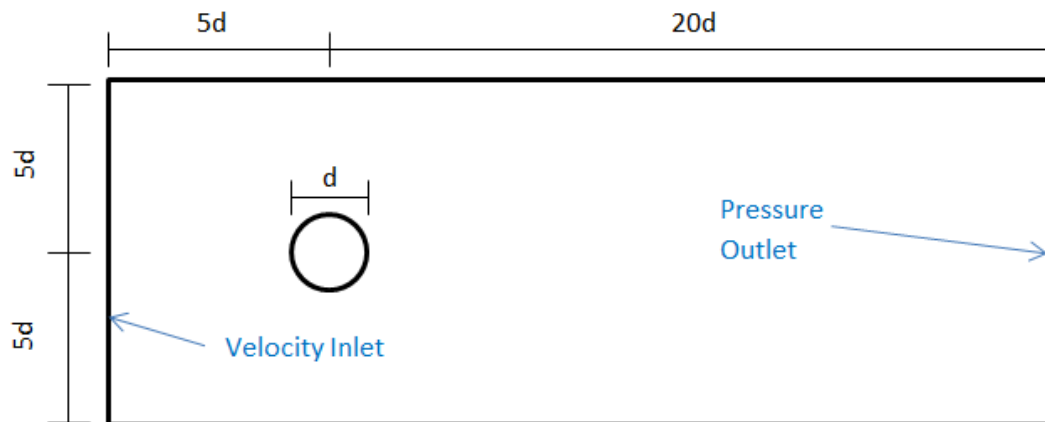


Figure 3.4 Sketch of Geometry Scene Created in STAR-CCM+

To view the flow behind the cylinder, a dense mesh scene is required. Figure 3.5 illustrates the mesh scene created in STAR-CCM+. Since CFD uses finite volume method, the number of cells used to mesh the environment directly affects the accuracy and length of time of the solution. To create this scene, 5,739 cells were used.

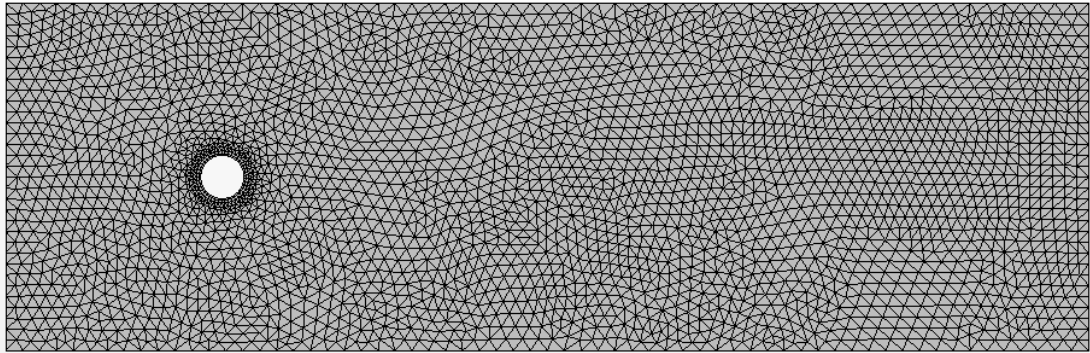


Figure 3.5 Tetrahedral Mesh Scene in STAR-CCM+ (5739 cells)

The Physics Models enabled in this simulation included:

1. Laminar Flow
 - a. The boundary layer around the cylinder and the area behind the cylinder remain laminar at $Re = 30$.
2. Constant Density
 - a. The assumption is constant density will not alter the results greatly while saving considerable computational time.
3. Segregated Flow
4. Liquid
 - a. Water is an incompressible liquid.
5. Implicit Unsteady
 - a. The Implicit Unsteady approach is used to observe the vortex shedding behind the cylinder, for this is a time-dependent problem (unsteady) and the governing equations used in this analysis are too complex to solve by explicit means. This method uses inner iterations to achieve convergence. The time step is updated after each cycle of inner iteration. The user must specify the physical time, the number of inner iterations, and the Courant number when setting the implicit unsteady model. Compared to the explicit integration, the implicit solver achieves faster convergence rates, but significantly larger storage requirements are necessary.
6. Two Dimensional
 - a. Three dimensional analysis is not required to view the vortices behind the cylinder since the cylinder is rigid. According to Al-

Jamal (2002), “the 3-D simulation is necessary for accurate results when the cylinder is vibrating.”

The parameters used for the main variables are summarized in Table 3.1.

Table 3.1 Physics Values and Parameters of $Re = 30$

Density	1 kg/m ³
Dynamic Viscosity	2×10^{-5} Pa*s
Diameter	0.01m
Reynolds Number	30 (Laminar Flow)
Inlet Velocity	0.06m/s
Time step	0.02s
Temporal Discretization	2 nd -order
Courant Number	5
Base Size of Mesh	0.003m
Maximum Inner Iterations	20
Maximum Physical Time	8s

The density and dynamic viscosity were altered to facilitate the altering of the Reynolds's number. Temporal discretization was set to 2nd-order (Newmark Method) compared to the 1st-order method (Euler method) to achieve more accurate results.

Figure 3.6 shows a good correlation between the results from STAR-CCM+ and those depicted in Figure 3.3.

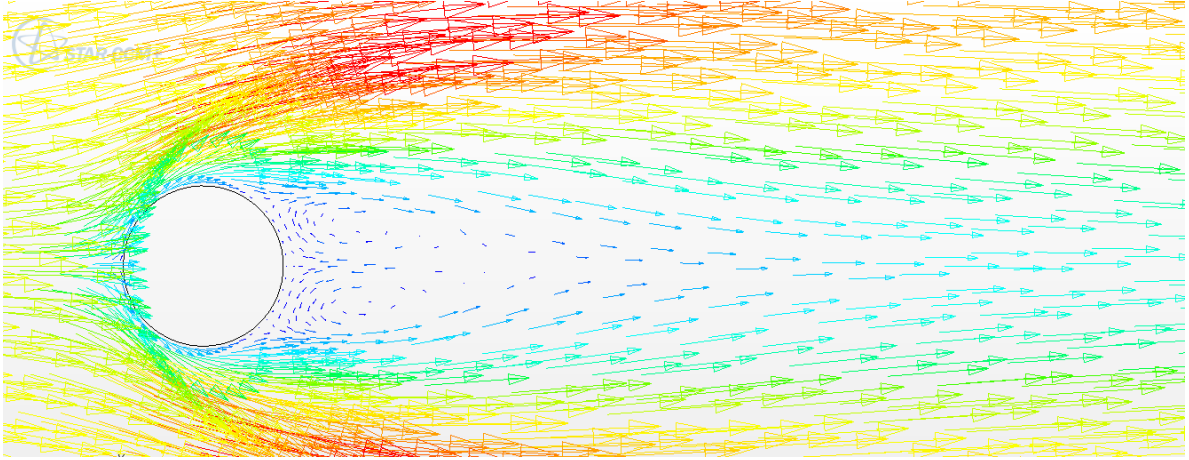


Figure 3.6 Velocity Vector Scene of Re = 30

In order to verify the mesh, another simulation was run with the Reynolds number increased to 75. To modify the Reynolds number, the inlet velocity was increased from 0.06m/s to 0.15m/s. All other parameters from the Re = 30 simulation remained the same as illustrated in Table 3.2.

Table 3.2 Physics Values and Parameters of Re = 75

Density	1 kg/m ³
Dynamic Viscosity	2x10 ⁻⁵ Pa*s
Diameter	0.01m
Reynolds Number	75 (Laminar Flow)
Inlet Velocity	0.15m/s
Time step	0.02s
Temporal Discretization	2 nd -order
Base Size of Mesh	0.003m
Maximum Inner Iterations	20
Maximum Physical Time	8s

The STAR-CCM+ simulation correctly displayed the von Karman Street behind the cylinder when Reynolds number equals 75 as shown in Figure 3.7.

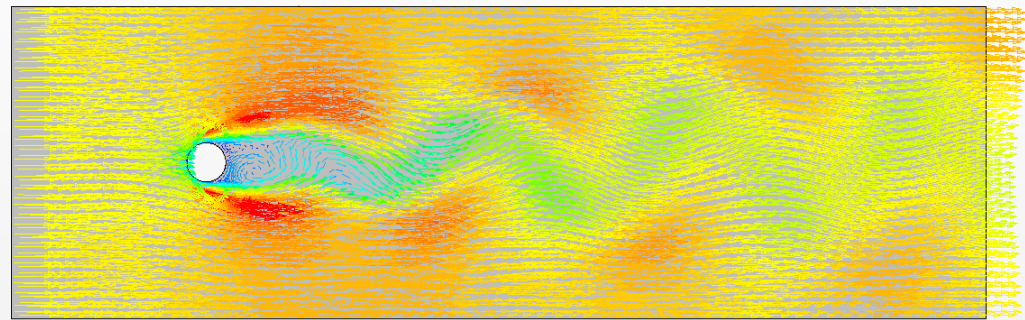


Figure 3.7 Velocity Vector Scene of $Re = 75$

Further benchmark analysis required simulating the von Karman Street at higher Reynolds numbers, turbulent flow was used instead of laminar, for “The transition to turbulence occurs in the wake region” when Re increases to 200 (Sumer 1997). STAR-CCM+ allows turbulence modeling with the Spalart-Allmaras Turbulence model, the K-Epsilon Turbulence model, and the K-Omega Turbulence model. The shear stress transport (SST) formulation of the K-omega turbulence model was the two-equation eddy-viscosity turbulence model chosen to run the simulations. The SST (Menter) K-

Omega Turbulence model was chosen due to its more accurate modeling of the near-wall region “with the free-stream independence of the standard k-epsilon model in the far field” (Izarra 2009).

The turbulent energy (k), the kinetic energy per unit mass of the turbulent fluctuations in a turbulent flow, is calculated with turbulence intensity and the mean flow velocity:

$$k = \frac{3}{2} (UI)^2$$

Where:

U = the mean flow velocity (0.35m/s), which is the average value of an unsteady flow

I = the turbulence intensity

The turbulence intensity measures the turbulence in the flow, and it is calculated by dividing the root mean square turbulence by the free stream fluid velocity (Blevins 1990):

$$\text{Turbulence Intensity: } \frac{u_{rms}}{U} = \frac{\text{root mean square turbulence}}{\text{free stream fluid velocity}}$$

The specific turbulent dissipation rate (ω or omega) is calculated by dividing the square root of the turbulent energy by the turbulent length scale:

$$\omega = \frac{\sqrt{k}}{l}$$

Where:

k = turbulent energy

l = turbulent length scale, which is typically used to estimate the turbulent properties of the inlets of CFD simulations

For $Re = 200$, K-Omega SST Turbulent Flow was used to model the von Karman Street.

Table 3.3 Physics Values and Parameters of $Re = 200$

Density	1 kg/m ³
Dynamic Viscosity	2×10^{-5} Pa*s
Diameter	0.01m
Reynolds Number	200 (K-Omega SST Turbulent Flow)
Inlet Velocity	0.4 m/s
Time step	0.02s
Temporal Discretization	2 nd -order
Base Size of Mesh	0.003m
Maximum Inner Iterations	20
Maximum Physical Time	8s

The STAR-CCM+ simulation as shown in Figure 3.8 accurately depicts the von Karman Street behind the cylinder at a Reynolds number of 200 when compared to Figure 3.3.

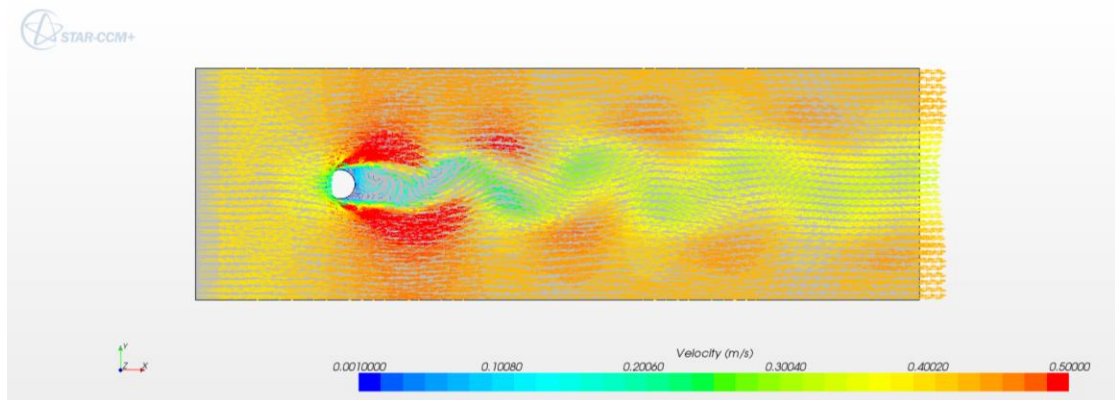


Figure 3.8 Velocity Vector Scene of $Re = 200$

Compared to Figure 3.7, the wake structure of velocity vector scene in Figure 3.8 is narrower. As the Reynold's number increases, the wake will become turbulent and narrower; additionally, the separation point around the cylinder will move further downstream of the cylinder cross-section due to an increase of momentum in the boundary layer arising from the turbulence of the free stream flow.

A final benchmark simulation was run with the Reynolds number increased to 1000. Sumer (1997) states that this region is known as the “subcritical critical flow regime” where the “wake is turbulent and the boundary layer remains laminar.” To modify the Reynolds number, the inlet velocity was increased from 0.4 m/s to 2.0 m/s. All other parameters from the $Re = 200$ simulation remained the same as illustrated in Table 3.4 except for the time step.

Table 3.4 Physics Values and Parameters of $Re = 1000$

Density	1 kg/m ³
Dynamic Viscosity	2×10^{-5} Pa*s
Diameter	0.01m
Reynolds Number	1000 (K-Omega Turbulent Flow)
Inlet Velocity	2.0 m/s
Time step	0.005s
Temporal Discretization	2 nd -order
Base Size of Mesh	0.003m
Maximum Inner Iterations	20
Maximum Physical Time	8s

When Reynolds number was increased from 200 to 1000, 0.02 seconds was not a sufficiently small value of time step to capture the formation of vortices in the cylinder's

wake. To accurately simulate the von Karman street, a time step of 0.005s was used.

Figure 3.9 illustrates the results of the $Re = 1000$ simulation.

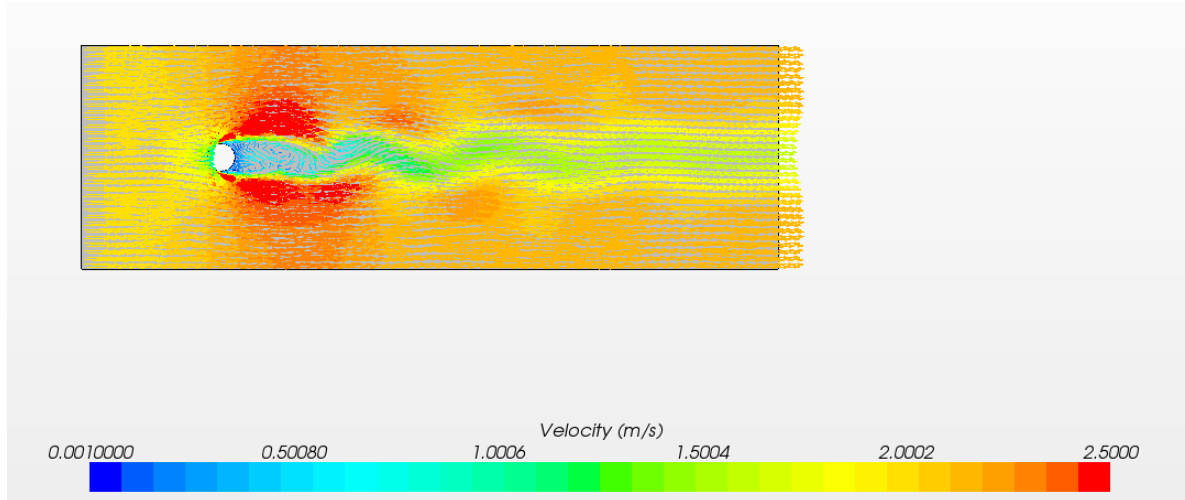


Figure 3.9 Velocity Vector Scene of $Re = 1000$

These two-dimensional analyses verify the VIV phenomenon is adequately modeled within STAR-CCM+, and they show how the parameters within the software must be set to effectively model turbulence.

3.4 Benchmark Pipe-Soil Interaction Studies

For the benchmarking of soil models, the soil was modeled as soft clay with the following parameters:

- The clay is almost incompressible ($\nu = 0.49$)
- The Coulomb-Mohr model was used to define yield criteria
- Cohesion was set at value of 0.0145 psi (100 Pa)
- The dilatation angle was set at 0°

- The friction angle was set at 0°
- The value of absolute plastic strain was set to zero, which means no plastic response of the soil was modeled. Only the elastic response of the soil was modeled to simplify the simulation.

Appendix E illustrates the benchmark pipe-soil interaction procedure used in ABAQUS and more information on the soil parameters within ABAQUS' Mohr-Coulomb model.

The soil's response to lateral displacement of a pipe depends on the submerged weight of the pipe, the soil shear strength, the interface friction coefficient, and the magnitude of the lateral displacement. As shown in Figure 3.10, berms are created as the pipe move side to side, and the pipe gradually lowers into the soil during the lateral movement, which matches the observations of Hesar (2004). The soil in Figure 3.10 was modeled within ABAQUS using the Coupled Eulerian-Lagrangian (CEL) approach, which is discussed further in section 4.4.2.1.

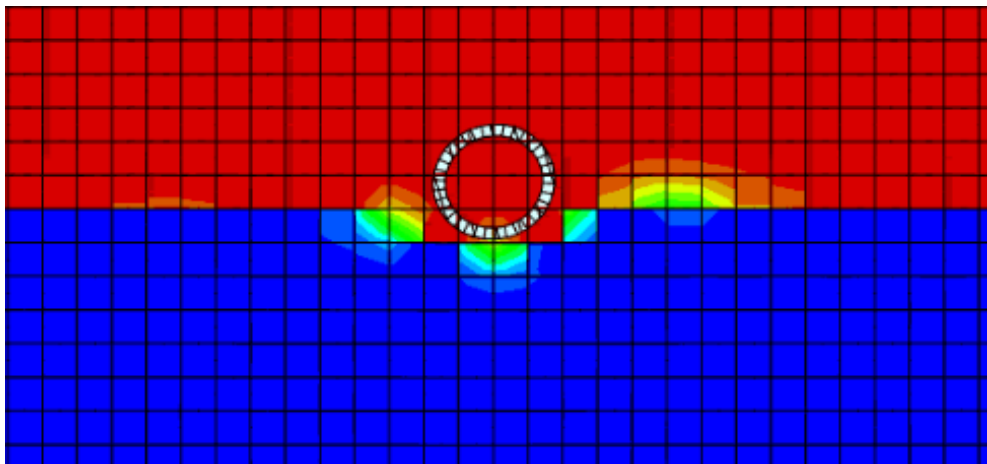


Figure 3.10 Pipe-Soil Interaction Representation with CEL

4 Methodology

The method presented in this thesis to incorporate the effects of pipe-soil interaction at the ends of a free span into computational simulations is broken down into three parts. First, the free span is simulated in a two-way FSI simulation without the effects of pipe-soil interaction to find the stresses and displacements of the span versus time. Second, the displacements resulting from the FSI simulation are tabulated. Third, a CEL model is developed to model soil at the ends of the free span. In this third step, the tabulated displacements from the FSI simulation are imposed on the free span in the CEL simulation to mimic the FSI deformations.

During the two-way FSI simulation, STAR-CCM+ solves for the pressures caused by the underwater current, and ABAQUS subsequently calculates the resulting displacements at each iteration. The deformed geometry of the free span is transferred back to STAR-CCM+ to solve the flow again and resulting pressure on the new geometry (Chica et al., 2012).

A text file is generated from the resulting output database file of the displacements at each time step of each section of the free span. The resulting displacements are tabulated and imported into the explicit CEL model to analyze the effects of integrating pipe-soil interaction on the stresses of the free span.

After various trials, the methodology described above is a current way to analyze the effects of pipe-soil interaction at the ends of the free span undergoing vortex-induced vibration. However, both fluid-structure interaction and pipe-soil interaction are complex problems to analyze and cannot be easily integrated due to difference in time dependency

and the large recorded deformations in pipe-soil interaction. For these reasons, FSI simulations with ABAQUS use the Dynamic/Implicit method, and CEL simulations with ABAQUS utilize Dynamic/Explicit to record large deformation soil response to interaction with the pipeline. An implicit analysis is different from an explicit analysis. In an explicit analysis, the solver is time-dependent, which means that the user must specify a small enough time step for the analysis to be stable. Explicit analysis is useful for solving time dependent problems (e.g. pipe clashing, car crash, etc.). The equations for implicit analysis are much more computationally difficult to handle; however, the user does not need to specify too small of a time step since implicit analysis is not as dependent on time as explicit analysis (i.e. there is not restriction on time step in implicit analysis). In order for implicit analysis to be accurate with larger time steps, the analysis must solve for equilibrium at each time step (or iteration), and this process can be accomplished with the Newton Raphson Method, which minimizes the residuals resulting from the implicit equations.

Before the two-way FSI simulation is started, initial conditions and free span characteristics must be defined. Figure 4.1 illustrates the methodology provided by DNV to correctly access the status of free span after installation. The screening method within DNV-RP-F105 takes into account the wave-induced flow velocity effects on the free span. This research takes into account only the effects of underwater current on the free span. Fatigue analysis is discussed in brief in the future work section. Ultimate limit state (ULS) check and span intervention analysis discussed in DNV-RP-F105 is not detailed in this research.

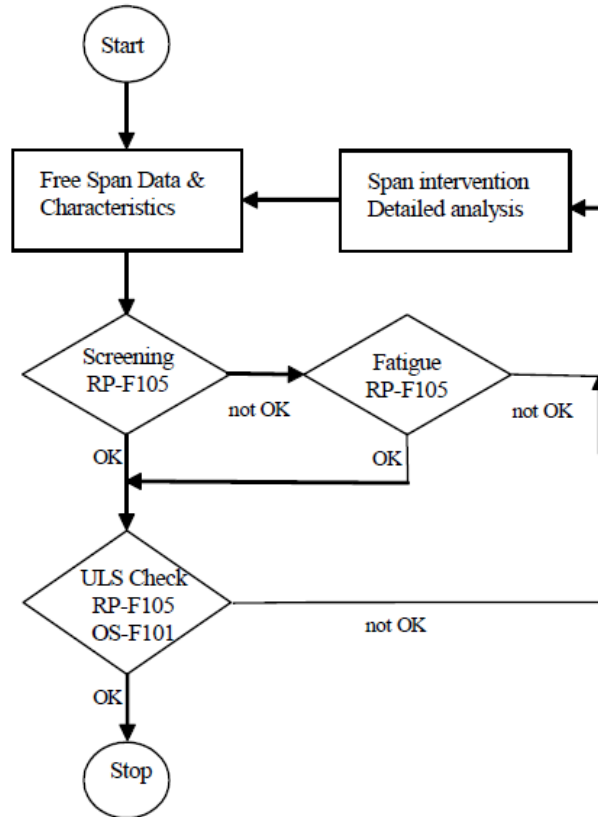


Figure 4.1 Flow Chart over Design Checks for a Free Span (DNV-RP-F105)

4.1 Free Span Data and Characteristics

Free spans can result from the pipeline installed over depressions in the seabed, or they can develop over time due to the subsea environment. Due to full exposure to underwater current, they are susceptible to fatigue damage caused by vortex-induced vibration. As the free span increases in length, the greater the concern becomes for failure due to fatigue caused by VIV.

The geometry used for both FSI and CEL simulations was a pipeline free span with a length of 10.2 meters (400 inches), an outside diameter of 0.254 meters (10

inches), and a thickness of 0.0254 meters (1 inch). The material of the free span is carbon steel grade X65, and its properties are listed in Table 4.1.

Table 4.1 Carbon Steel X65 Properties

Property	Value
Density	0.284 lb/in ³ (7861 kg/m ³)
Young's Modulus	30,000 ksi (207 GPa)
Poisson's Ratio	0.303

Typically, a free span of 400 inches (10.2 meters) in length will not require corrective action. According to Palmer (2008), free spans of up to 110 meters in length were left in operation for years after they were found. A free span of over 400 meters will more realistically represent a span in need of corrective action. However, this thesis uses a 400 inch span to present a new methodology of analyzing free spans while looking at the effects of pipe-soil interaction at the ends of the span.

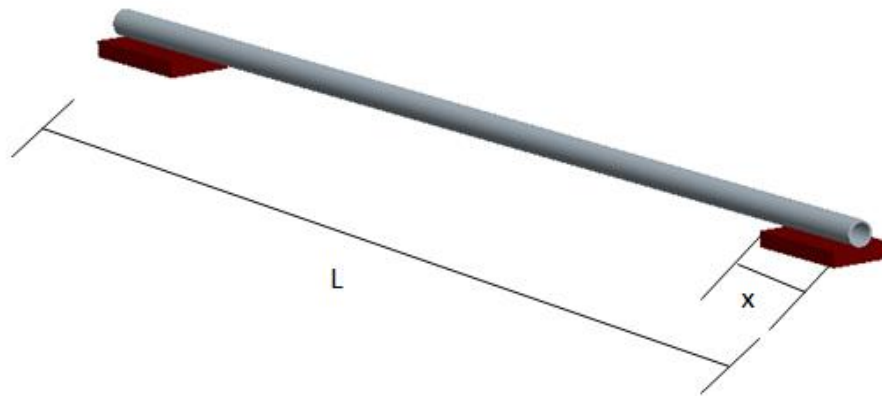


Figure 4.2 Visualization of Free Span for FSI and CEL Simulations

The FSI co-simulations and modal analyses only examined the 400 inch free span section of the pipeline (i.e. $L-2x$ in Figure 4.2). Sensitivity studies have shown that the

two additional 20 inch pipe sections have minimal effect on the value of the free span's natural frequency.

4.2 ABAQUS Modal Analysis

ABAQUS is a widely software in the modal analysis of pipelines, risers, and jumpers to obtain the natural frequencies and mode shapes due to its nonlinear capabilities. DNV Fatfree and Shear7 utilize the results from ABAQUS' modal analysis to examine the effects the vortex-induced vibration on subsea risers and pipes. Similarly, a computational fluid-structure interaction approach can use the results obtained from the modal analysis to determine if resonance is induced.

The non-dimensional natural frequency of a subsea piping component is determined by its geometry, its mass plus the added mass coefficient, and its boundary conditions (Blevins 1979). Common practice for determining the natural frequency of free spans is to analyze the effective span length, which is the length of an idealized fixed-fixed span having the same structural response as the real free span supported on soil (DNV-RP-F105 2006).

The free span analyzed in this paper is considered to be an isolated single span with single mode response. The FEA software ABAQUS was used to determine the natural frequencies of the pipeline free span. The free span was modeled with C3D8R (8-node brick) elements for a total of 16,560 nodes and 8,256 elements.

For a 400 inch empty free span with both ends fixed in all six degrees of freedom, the frequency of the first mode is equal to 0.72133 Hz. Table 4.2 shows the natural frequencies and periods for the first five modes of the free span.

Table 4.2 Free Span Natural Frequencies

Mode Number	Natural Frequency (Hz)	Period (s)
1	0.72133	1.3863
2	0.72133	1.3863
3	1.9689	0.50790
4	1.9689	0.50790
5	3.8112	0.26238

Appendix C illustrates more detail of the natural frequency results performed in ABAQUS.

The result window of the first mode shape in Figure 4.3 shows the highest displacement of the free span to be near the center of the free span when this mode is excited. The free span undergoes in-line deformation when mode 1 is excited.

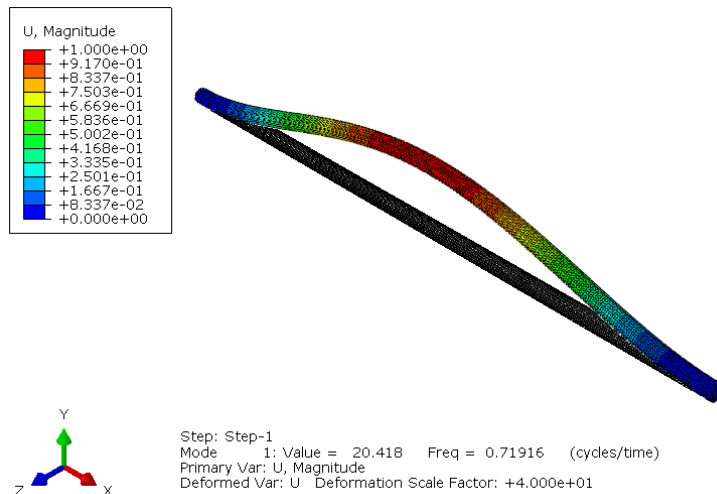


Figure 4.3 Mode-1 Shape for Free Span Model – Isometric View

Further research will need to be carried out to develop a model that will determine how much the natural frequency of the free span is affected by the soil.

4.3 Screening

To concentrate on examining the effects of pipe-soil interaction at the ends of subsea free spans, the Reduced Velocity and Reynolds number will be constant for all analysis.

As Reynolds number increases, the free span is more susceptible to the forces generated by the underwater current and vortices; however, higher Reynolds numbers do not guarantee higher response amplitude. The Reynolds number for this research was set at 52,000 due to the parameters given (i.e. the pipe diameter, the kinematic viscosity of water, and the current velocity calculated from the natural frequency).

While the response amplitude due to VIV of the free span is not necessarily dependent on the Reynolds number, this response amplitude is dependent on the free span's natural frequency, which is a non-dimensional parameter within the reduced velocity equation.

The reduced velocity parameter (V_R) is a non-dimensional parameter that is important in studying VIV:

$$V_R = \frac{U_c}{(f)(D)}$$

where f is the natural frequency, U_C is the combination of mean current velocity normal to the span and significant wave-induced flow velocity, and D is the outside diameter of

the pipe. For the purposes of this study, it is assumed waves have no significant effect (i.e. only the underwater current induces the VIV response of the free span).

When the Reduced Velocity reaches one, in-line VIV response is triggered. Cross flow VIV response does not occur until the Reduced Velocity reaches a value of at least two. Figure 4.4 illustrates the inline VIV amplitude dependence on the reduced velocity. For this study, the lock-in region (i.e. resonance) is to be assumed; therefore, the stability parameter (K_s) will be assumed to be zero.

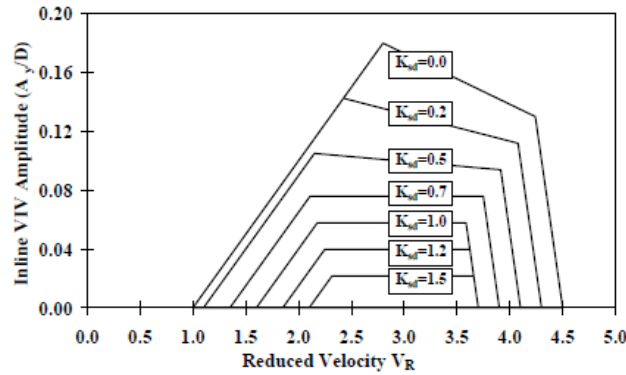


Figure 4.4 In-line VIV Response Amplitude versus V_R and K_S (DNV-RP-F105)

The K_{sd} parameter is the stability parameter with a damping factor.

$$K_{sd} = \frac{K_s}{\gamma_k}$$

where K_s is the stability parameter (i.e a parameter dependent on the structural, hydrodynamic, and soil dampening) and γ_k is the damping safety factor.

To mimic the lock-in response at mode one for the FSI co-simulation, the velocity was calculated when the reduced velocity was set to one and the frequency was set to the

free span's natural frequency at mode one. This procedure matches the vortex shedding frequency with the natural frequency of mode one. The resulting value of 0.183 m/s was set as the uniform current velocity value within the FSI co-simulation.

4.4 Fatigue Analysis

The procedure and results of the new methodology to analyze fatigue of pipeline free spans by factoring in the effects of soil response at the span's ends are presented.

4.4.1 Fluid-Structure Interaction

Fluid-structure interaction (FSI) occurs when a fluid flow interacts with a solid structure. A finite element (FE) code is used for structure analysis to capture the nodal displacement of the morphing geometry (i.e. the free span), and a CFD code uses the finite volume method to more accurately capture the fluid flow effects on the span. To perform the multi-physics analysis of FSI, one needs to couple these accepted methods to more realistically determine the displacements as a result of the fluid flow.

4.4.1.1 Coupling of ABAQUS and STAR-CCM+

Different methods exist to perform FSI. The first method is one-way coupling. To achieve one-way coupling, the model must first be prepared in both STAR-CCM+ and the 3rd party CAE software. STAR-CCM+ can perform FSI simulations with ABAQUS. After STAR-CCM+ runs the CFD analysis, the solution data is mapped into ABAQUS. ABAQUS then runs its analysis with the STAR-CCM+ data. Results are achieved. The disadvantage of one-way coupling is the process only accounts for one time-step. To

counter this disadvantage, two-way coupling of ABAQUS and STAR-CCM+ is necessary.

The primary difference between two-way and one-way coupling is that the data is automatically mapped back and forth between STAR-CCM+ and ABAQUS at each time-step or iteration.

4.4.1.1.1 Implicit vs. Explicit Coupling

This work presents the state of the art capability of using FSI by implicitly coupling the FEA codes of ABAQUS and the CFD codes of STAR-CCM+, which results in the transfer of information between the software at every iteration. Implicit coupling is used for the two-way FSI co-simulation due to the difficulty explicit coupling has in dealing with incompressible flows (e.g. water). The instability with explicit coupling occurs when a light and/or compliant structure interacts with incompressible fluid due data transferring at each time step instead of every iteration.

4.4.1.1.2 FSI Co-Simulation Setup

The geometry was created within ABAQUS and meshed with C3D8R brick elements. After the dynamic implicit model was set up within ABAQUS, an input file was generated to be linked to STAR-CCM+ during the co-simulation.

Similar to Chica et al. (2012), the CFD modeling was set up for FSI by applying adaptive mesh refinement and mesh morphing. The free span and the surrounding environment were modeled with polyhedral elements with thin element layers surrounding the outside diameter of the free span. The wall function used within STAR-

CCM+ was the all y^+ wall function, which successfully models wall treatment for when both y^+ is greater than thirty and y^+ is approaching zero.

A mesh sensitivity study was performed to achieve grid independence by adjusting the base size mesh. This study found that the optimum mesh produced a total of 1,309,032 cells for the free span plus the surrounding environment based on the computational capability available. Table 4.3 shows the results of the mesh sensitivity study done within STAR-CCM+.

Table 4.3 FSI Mesh Sensitivity Results

FSI Sensitivity Results (STAR-CCM+)*				
Base Size**	Number of Cells	Run Time (hours) ³	Run Time (hours) ⁴	Max Displacement ($\times 10^{-2}$ in) ³
7	241799	7.78	N/A	9.477
6	461895	8.33	N/A	11.32
5	723343	10	N/A	6.064
4	1309032	16.18	N/A	6.482
3	3643329	12.5***	12.83	N/A
* A seed edge of 16 for the Abaqus mesh was used in these simulations				
**A Box Volume Shap was drawn around the free span to increase mesh refinement around the span.				
*** Simulation failed at time = 2.34 seconds due to insufficient memory on a 8 core, 16GB RAM computer				
³ Amount of physical time is 5 seconds				
⁴ Amount of physical time is 0.75 seconds				

The simulation used the SST K- ω Reynolds-Average Navier-Stokes (RANS) turbulence model to capture pressure gradients and flow separation around the span. The physics models selected for this FSI simulation included: three dimensional, implicit unsteady, segregated flow, gravity, and cell quality remediation. The reference altitude (i.e. water depth) was set to 100 meters.

4.4.1.2 FSI Results

The results from the two-way FSI co-simulations illustrate how the free span structure interacts with the underwater current. Maximum displacement results for the FSI co-simulation are shown in Figure 4.5. This simulation was run for five seconds physical time.

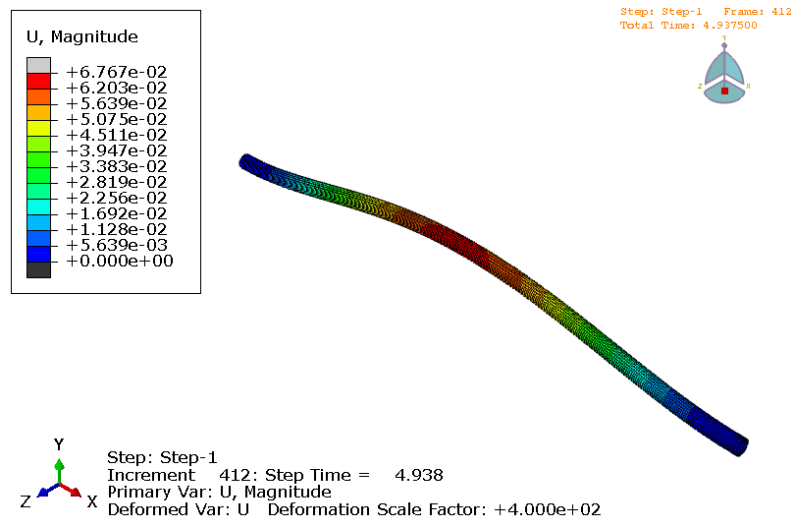


Figure 4.5 Maximum Displacement Results from FSI

Stress versus time graphs may also be obtained from these FSI results; as a result, fatigue life analysis based on ASTM standards may be performed in combination with the Palmgren-Miner rule to estimate the fatigue life. However, this approach does not factor in the effects of pipe-soil interaction at the ends of the free span. To effectively determine these effects, a method must be developed to transfer the displacements resulting from the two-way FSI co-simulation to a CEL model, which can effectively simulate pipe-soil interaction. Results for maximum principle stress at the effective

length of the span as a function time from the two-way FSI co-simulations are illustrated in Figure 4.6.

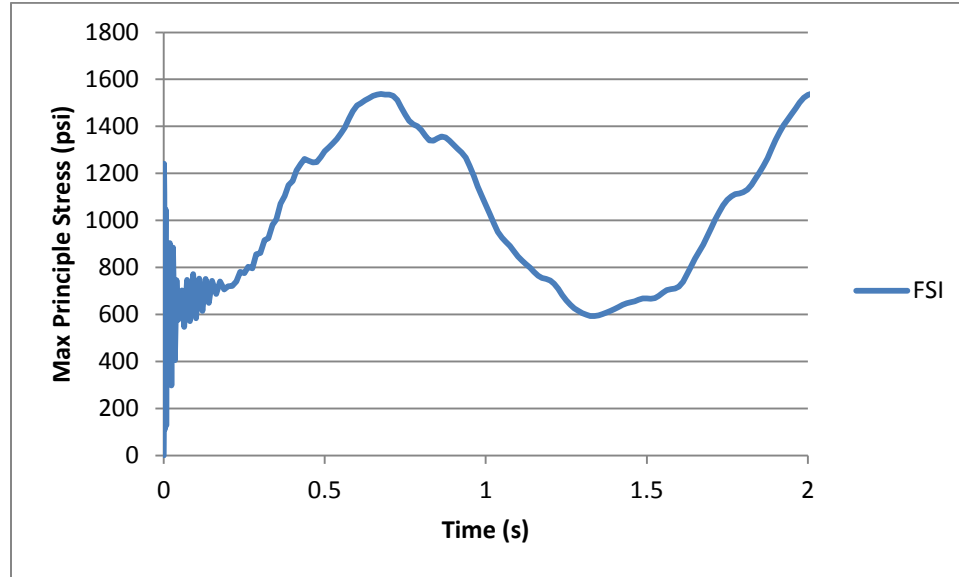


Figure 4.6 Principle Stress vs. Time History for 2 Seconds Physical Time

4.4.2 Integrating Pipe-Soil Interaction

As mentioned in the screening method, the FSI co-simulation between STAR-CCM+ and ABAQUS was set up to mimic the response of mode one. This was done to easily define the amplitude of displacement within the CEL model.

Resulting displacements from the two-way FSI co-simulation were recorded at every 0.1 seconds to be inputted into the CEL model.

Unfortunately, this method may prove tedious, as segments throughout the free span must have their displacement defined by the displacements resulting from the previous FSI co-simulation. For the CEL simulations in this thesis, one segment of the length equivalent to one outside diameter of the free span has its displacement amplitude

defined in the center of the span; however, more segments may need to be defined pending on the mode response and the length of the free span.

Since this research assumes single mode response, the imposing of a single segment's displacement in the center of the span proved to realistically reproduce the stress versus time maximums resulting from the FSI simulation as shown in Figure 4.7. These stress results were taken from a probe at the free span's effective length location (i.e. where the soil starts to support the free span).

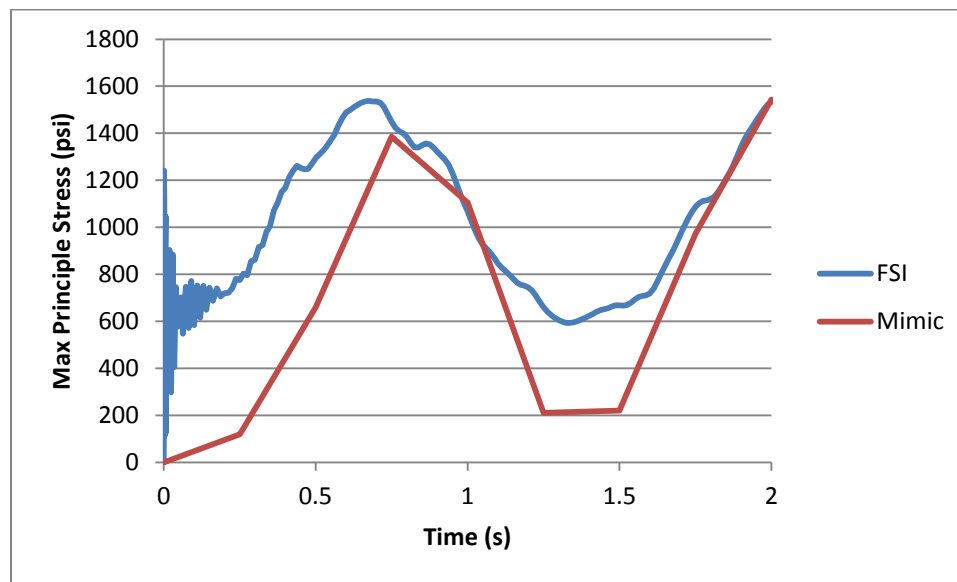


Figure 4.7 Mimic of Von Mises Stress vs. Time History for 2 Seconds Physical Time

4.4.2.1 Determining the Correct FE Model to Represent the Soil

Recent improvements in FEA software has resulted in improved engineering tools to analyze pipeline interaction with the seabed. Different methods to analyze the soil response were researched.

The principal advantage of a purely Lagrangian formulation is the fact that the interface between the pipe and target (i.e. the soil) is precisely defined and tracked. Unfortunately, large deformations within the soil region will lead to hopeless mesh tangling in purely Lagrangian reference plane (Abdalla 2009).

An Eulerian reference frame avoids the difficulty of mesh tangling in the soil but also loses the precise interface description provided by the Lagrangian formulation. Treating computational cells at the pipe-soil interface as mixtures of pipe and soil materials tends to dilute the material properties. This may result in excessive erosion of the pipe material in the soil (Silling 1993).

Arbitrary Lagrangian-Eulerian (ALE) methods are an alternative to pure Lagrangian analysis. These “adaptive meshing” methods combine the features pure Lagrangian and pure Eulerian analysis by constraining the mesh motion to the material motion at only the free boundaries (Abdalla 2009). However, ALE has trouble maintaining high quality meshes upon extreme deformation due to its inability to alter the connectivity of the mesh (Abdalla 2009) as shown in Figure 4.8.

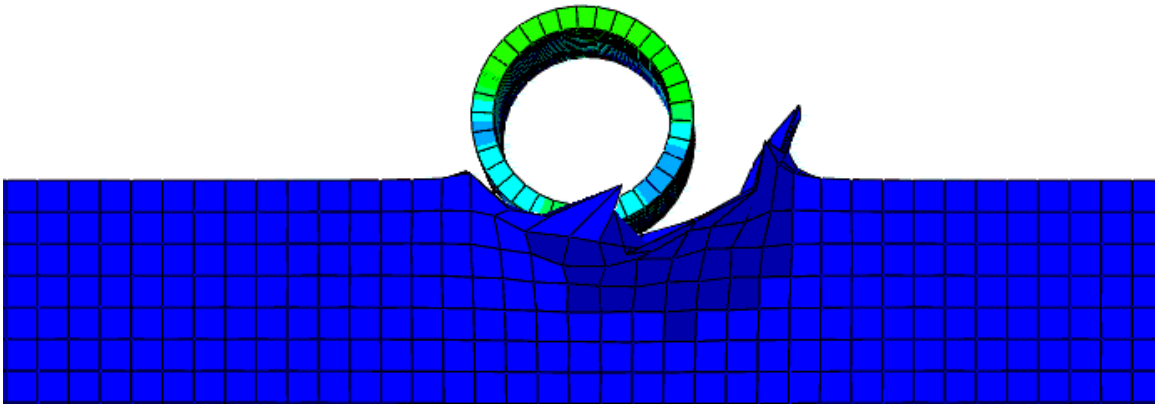


Figure 4.8 Distorted Mesh Failure with Soil Modeled with ALE Methods

The Coupled Eulerian-Lagrangian (CEL) method attempts to capture the strengths of the Lagrangian and Eulerian methods (ABAQUS Documentations, 2010). In general, a Lagrangian reference frame is used to discretize the pipe while an Eulerian frame is used to discretize the soil. Figure 4.9 illustrates a sample of benchmark studies analyzing the soil response to lateral pipe movement. The post-processing window illustrates the resulting volume of void and soil material, where void is represented by red elements and soil is represented by blue elements. The green and yellow areas represent a mixture of soil and void areas.

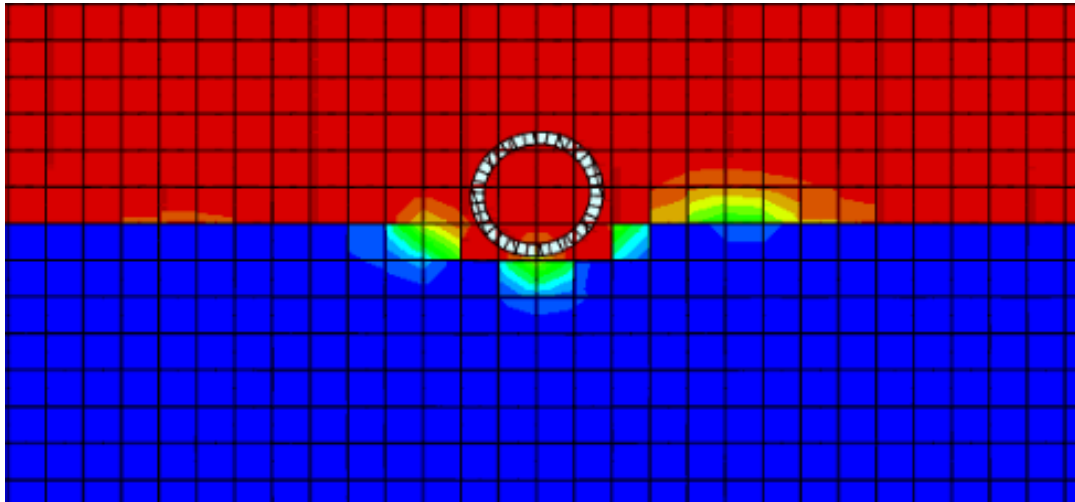


Figure 4.9 Pipe-Soil Interaction Representation with CEL

4.4.2.2 The CEL Model

The free span model for the CEL simulations included the 400 inch free span section from the FSI simulation and two additional pipe sections supported by the seabed. Figure 4.10 illustrates the initial setting of one end of the free span on the soil.

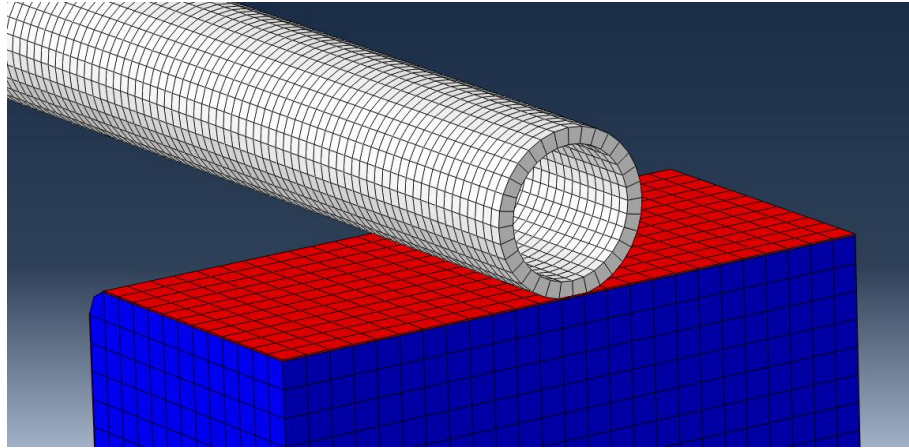


Figure 4.10 CEL FE Free Span Model Setup

Similar to the modal and FSI analysis, the free span was modeled with C3D8R (8-node brick) elements. The Eulerian mesh was modeled with linear hexahedral element type EC3D8R. Within the CEL model, the soil and free span picture in Figure 4.10 are encompassed by void elements. The interaction between the pipeline and soil is defined by general contact. For all CEL models, only the elastic response of the soil was modeled simplify the simulations. Future work should incorporate the soil's plastic response to loading.

To verify the soil's effect on the free span in the CEL models, separate explicit, dynamic models were ran without the modeling of the soil. Figure 4.11 shows the results of a span of 620 inches in length modeled without soil, with 110 inches of soil modeled below the pipe from the effective length of 400 inches to the either end, and with the pipe embedded in 110 inches of soil modeled from the effective length of 400 inches to either end. Figure 4.11 illustrates that the soil does have an effect on the pipe. Appendix L further shows different cases that further validates the soil's effect on the pipe.

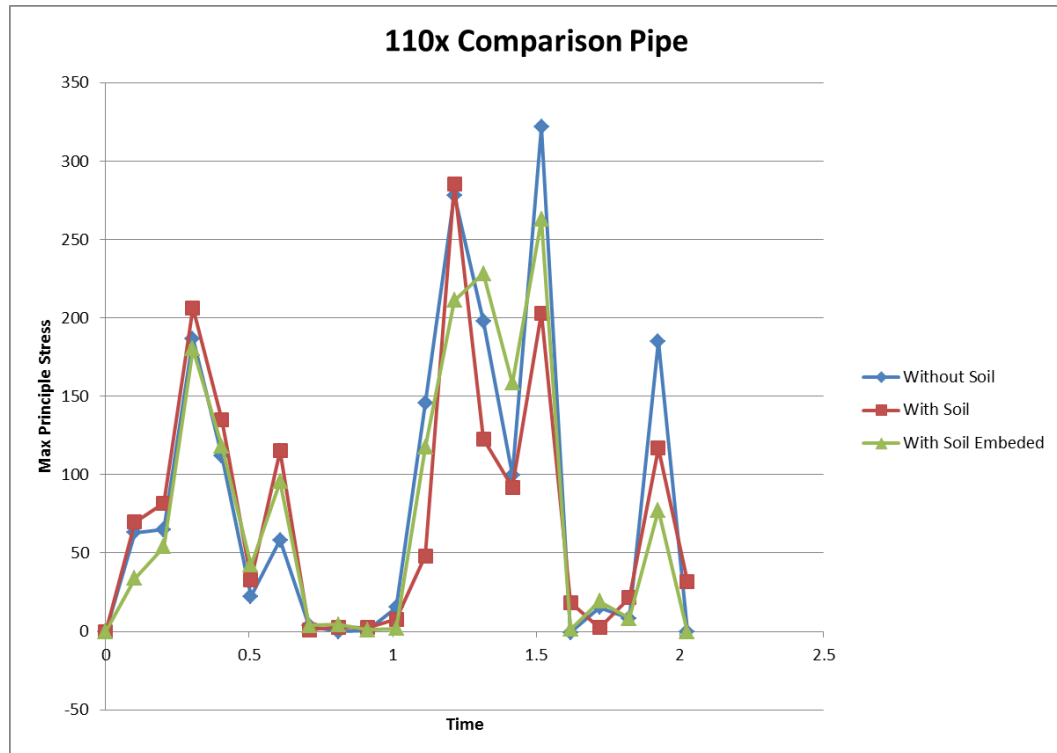


Figure 4.11 Comparison of Different 620 inch Pipe Cases

4.4.2.3 Computational Design of Experiments

In order to find the design of experiment (DOE) sensitivity of the range of different variables, a computational DOE was used to capture the results of each range of inputs. Three computational DOE models were used and compared to determine which one was more suitable for this particular problem. The three DOE models included a full factorial design at the corners, a space-filling design, and a surface response design. Table 4.4 portrays the advantages, disadvantages, and number of runs used for each DOE model. More information about each model and the results of a separate FSI DOE are discussed within the appendix H of this report.

Table 4.4 Advantages and Disadvantages for Each Computational DOE Model

DOE Model	Number of Runs	Advantages	Disadvantages
Full Factorial at the Corners	9 (8 at the corners + 1 at the midpoint)	<ul style="list-style-type: none"> Find responses at the maximum and minimum ranges of each design input If midpoint is analyzed, good for determining assumed linear responses and interactions throughout the design space 	<ul style="list-style-type: none"> May not correctly interpret responses not near the midpoint within the design space Not good for interpreting nonlinear responses throughout the design space
Space-filling Design (Latin Hypercube)	6 within the design space	<ul style="list-style-type: none"> The Latin hypercube design is “a way to generate designs that spread observations evenly over the range of each input separately” (Santner 127). 	<ul style="list-style-type: none"> If entire design space is not analyzed, values outside the region may not be correctly interpreted (e.g. the maximum and/or minimum responses at the corners of the design space)
Surface Response Design (Box-Behnken)	13 (12 points along the edges of the design space + 1 at the midpoint)	<ul style="list-style-type: none"> Good for interpreting nonlinear responses throughout the design space 	<ul style="list-style-type: none"> May have inaccurate interpretations at the design corners (i.e. at the combined factor extremes)

A benchmark computational DOE was performed to determine which computational DOE model best captured free span stress response from VIV. Appendix H details the evaluation of the models within the benchmark DOE. Due to its interpretation of nonlinear responses throughout the design space within the benchmark DOE, a Box-Behnken (Surface Response) design is chosen to capture the span’s stress

response to the prescribed VIV displacement amplitude and the soil interaction. Figure 4.12 illustrates how the design points are distributed for this model.

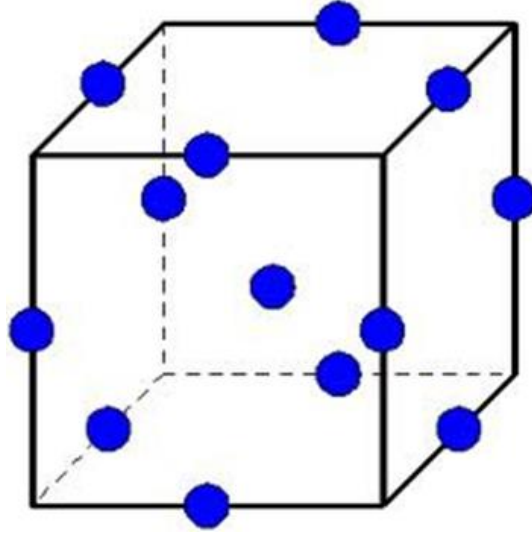


Figure 4.12 Location of the Design Points for the Box-Behnken Design (itl.nist.gov)

For this experiment, constraints and assumptions are made based on literature and to simplify the theory. Constraints within this experiment include:

- The effective length of the pipeline free span will remain constant.
- The physical time of each simulation will be set to a maximum of 2 seconds.
- The thickness will remain constant at 10% of the outside diameter.

Assumptions within this experiment include:

- The velocity of the flow will be uniform.

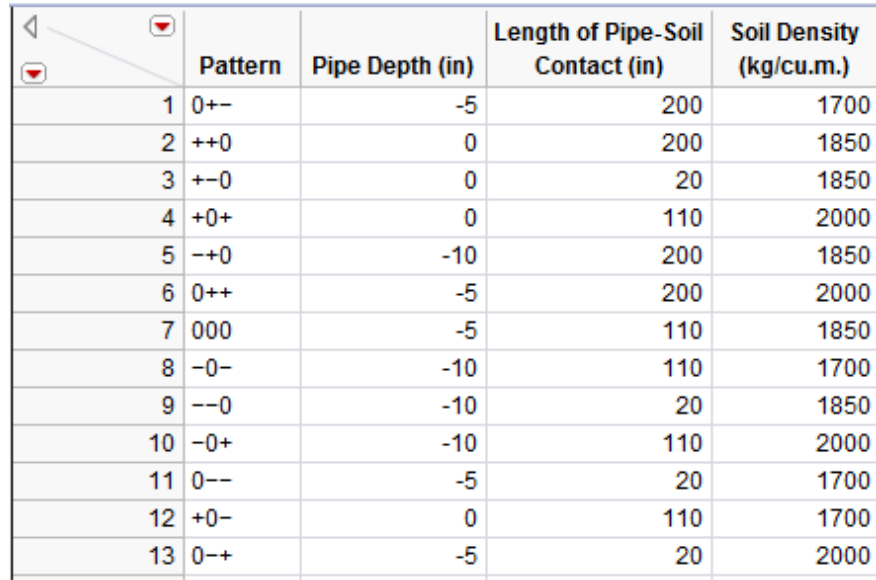
The three inputs for this DOE are listed in Table 4.5.

Table 4.5 Inputs for the Box-Behnken

Input	Range
Soil Density	1700-2000 kg/m ³
Pipe Embedment	0-10 inches
Pipe-Soil Contact at One End of the Span	20-200 inches

Appendix I illustrates the different pipe embedment and soil contact with the pipeline free span.

Similar to the benchmark DOE detailed in appendix H, JMP commercial software was used to calculate the design points of the Box-Behnken design. Figure 4.13 illustrates the design space setup from commercial software.



	Pattern	Pipe Depth (in)	Length of Pipe-Soil Contact (in)	Soil Density (kg/cu.m.)
1	0+-	-5	200	1700
2	++0	0	200	1850
3	+-0	0	20	1850
4	+0+	0	110	2000
5	--0	-10	200	1850
6	0++	-5	200	2000
7	000	-5	110	1850
8	-0-	-10	110	1700
9	--0	-10	20	1850
10	-0+	-10	110	2000
11	0--	-5	20	1700
12	+0-	0	110	1700
13	0-+	-5	20	2000

Figure 4.13 Box-Behnken Design Space Setup

For the computational DOE described in Figure 4.13, there exists nine different combinations of pipe depths with length of pipe-soil contacts; therefore, nine different finite element models were developed for CEL analysis. For each finite element model, grid independence was found for the Eulerian mesh (i.e. the soil). Appendix F lists the

results of the soil grid independence studies for each of the nine finite element models. Additionally, different length of pipe-soil contacts required three pipelines of different lengths (440 inches, 620 inches, and 800 inches). Static grid independence analysis was performed to find the pipeline mesh independence (i.e. where the pipeline's mesh does not have any effect on the final answer). Appendix G lists the results of the pipeline grid independence analysis for each of the three different cases.

5 Summary of Findings

The results of the sensitivity analysis and the computational DOE are presented in this section. Commercial software was used to derive the results from the Box-Behnken design model, and MATLAB was used to determine stress amplitudes based on ASTM's practices for cycle counting in fatigue analysis.

5.1 DOE Screening Results

JMP commercial software has the ability to screen each variable and combination of variables to find the variable that has the maximum effect on the output. As shown in Figure 5.1, pipe depth has the maximum effect on the stress response of the pipeline free span.

4 Contrasts						
Term	Contrast			Lenth	Individual	Simultaneous
				t-Ratio	p-Value	p-Value
Pipe Depth (in)	0.104307			2.36	0.0385*	0.2586
Length of Pipe-Soil Contact (in)	-0.030371			-0.69	0.4886	1.0000
Soil Density (kg/cu.m.)	-0.005361			-0.12	0.9151	1.0000
Pipe Depth (in)*Pipe Depth (in)	0.050921			1.15	0.2349	0.9427
Pipe Depth (in)*Length of Pipe-Soil Contact (in)	0.028643			0.65	0.5406	1.0000
Length of Pipe-Soil Contact (in)*Length of Pipe-Soil Contact (in)	0.047202 *			1.07	0.2679	0.9708
Pipe Depth (in)*Soil Density (kg/cu.m.)	0.000638			0.01	0.9901	1.0000
Length of Pipe-Soil Contact (in)*Soil Density (kg/cu.m.)	-0.006283			-0.14	0.9013	1.0000
Soil Density (kg/cu.m.)*Soil Density (kg/cu.m.)	-0.034713 *			-0.78	0.4124	0.9999

Figure 5.1 Screening Results from Commercial Software

5.2 Findings from DOE Sensitivity Analysis

Findings were determined before the computational design of experiment was performed. In the grid independence studies of the soil, maximum stress responses of the free span trended based on different initial pipe depths and pipe-soil contact lengths, and Figures 5.2 and 5.3 show these results respectively.

According to Figure 5.2, the entrenching of the pipeline mitigates the stress response of the free span; therefore, a free span fully entrenched at the ends is the best case scenario.

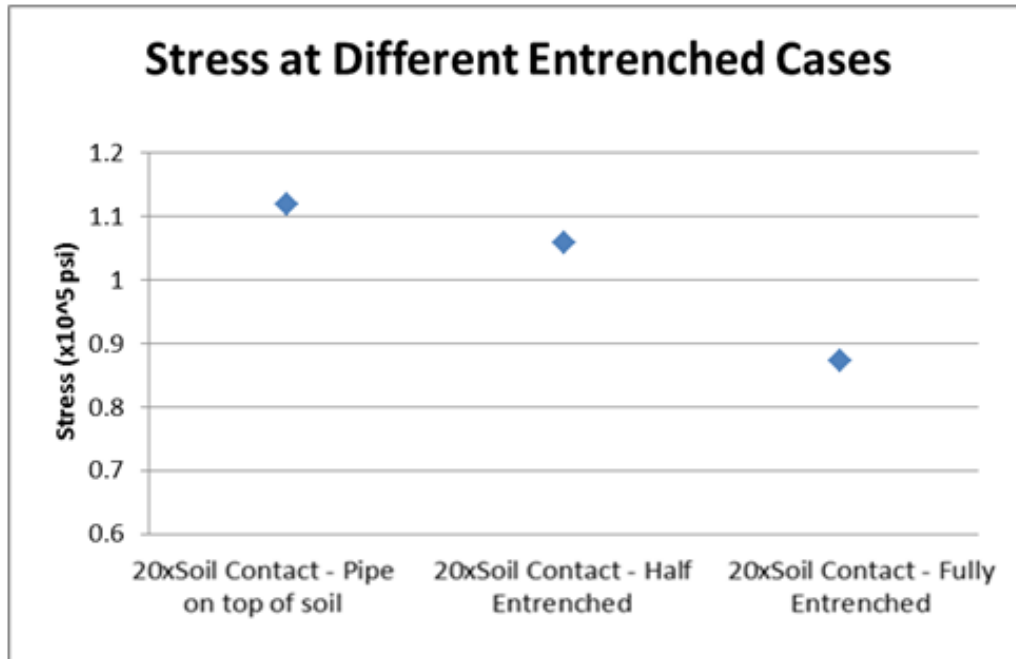


Figure 5.2 Stress Results at Different Pipe Embedment

Figure 5.3 portrays the necessity to model enough soil along the ends of the span in free span analysis; however, it is not necessary to model too much soil along the ends. For the case of the 400 inch free span, 110 inches of soil at either end of the free span is sufficient adequately model the accurate stress response, and 200 inches of soil at either end of the free span is unnecessary.

Extra cases were run for 50 inches and 100 inches of soil at either end of the span. The results (as shown in Figure 5.3) prove a non-linear relationship exists as more soil is modeled along the ends of the span.

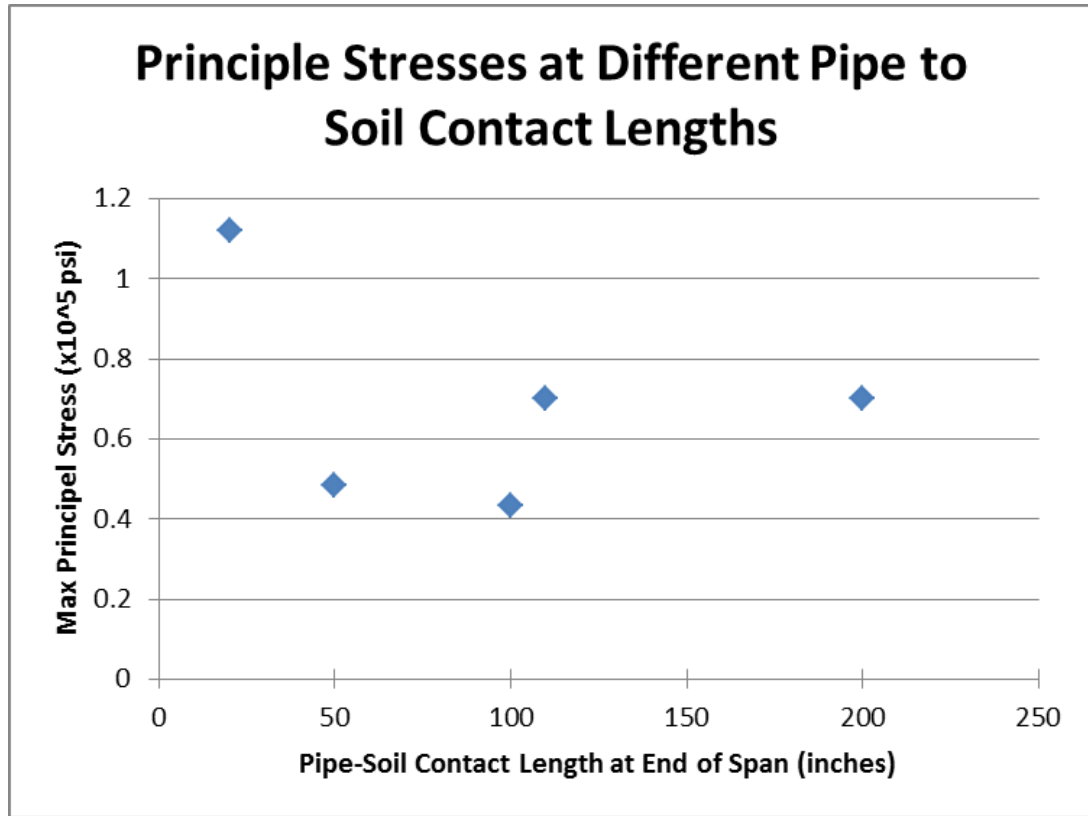


Figure 5.3 Stress Results at Different Pipe-Soil Contact Lengths

5.3 DOE Results

As mentioned in Table 4.4, the disadvantage of the Box-Behnken DOE model is the estimates that it makes at the corners of the design space. Figure 5.4 illustrates the estimates made by the Box-Behnken DOE at the corners.

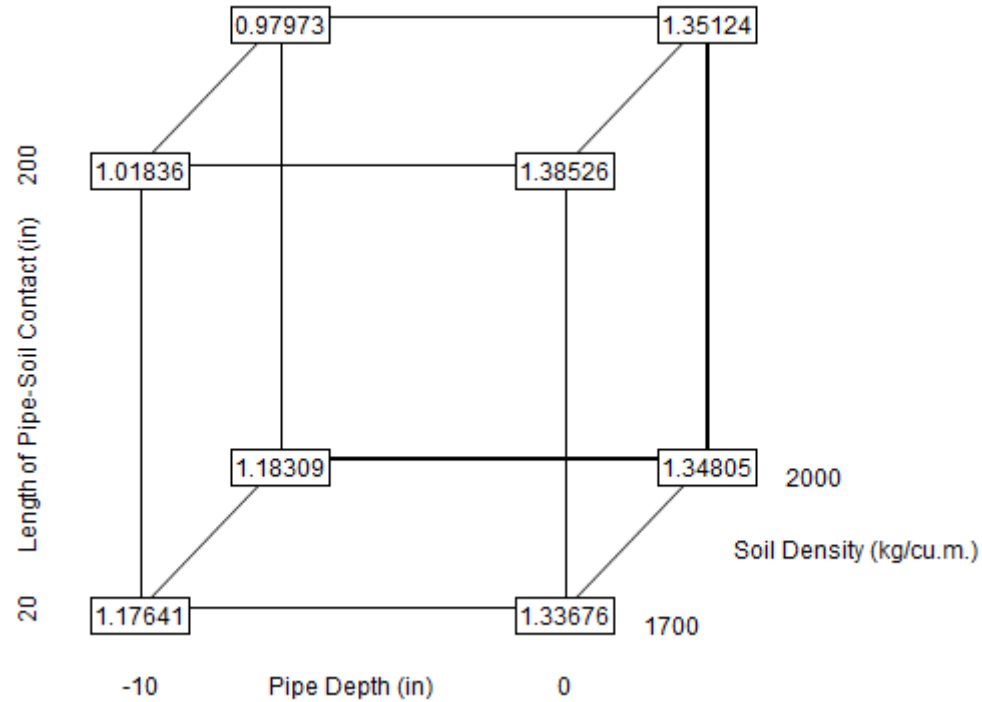


Figure 5.4 Box-Behnken Stress Estimates at the Corners

However, findings and conclusions can be drawn based on these results as well as the profilers from commercial software:

- The pipe depth has the maximum effect on the free span's stress response.
- Increasing the length of pipe-soil contact mitigates stress responses for entrenched spans but not spans on top of the soil.
- Different soil densities have minimal effect on the stress responses when compared to the other two variables.
- According to Figure 5.4, the minimum stress response is when the pipe depth is at minus ten inches, the length of pipe-soil contact is at 200 inches, and soil density is at 2000 kilograms per cubic meter. A prediction profiler can be used to confirm where the minimum stress response occurs.

A prediction profiler is useful for predicting how different input variables effect the output response.

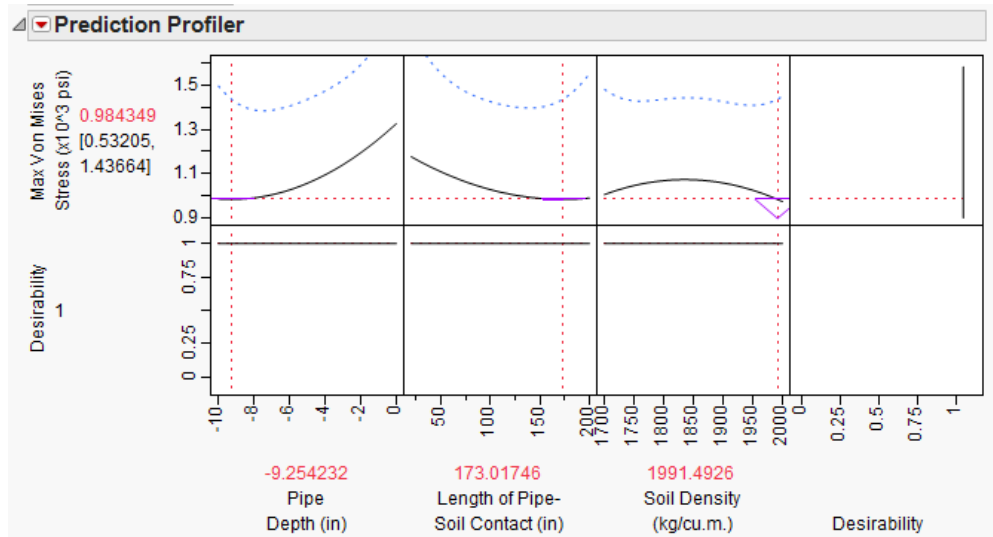


Figure 5.5 Prediction Profiler

As shown in Figure 5.5, the prediction profiler can be used to find maximum desirability (i.e. the point where each variable is set to produce the minimum stress response). The blue dashed lines within the prediction profiler within Figure 5.5 represent confidence levels. The closer the blue dashed lines are to the black lines (i.e. the predicted output response), the more confident the predictions are between design points.

Figure 5.5 shows the setting of each variable where minimum stress response occurs. These settings are similar to run number ten of the Box-Behnken design setup in Figure 4.11; therefore, the stress versus time graph was obtained from this case and is shown in green in Figure 5.6.

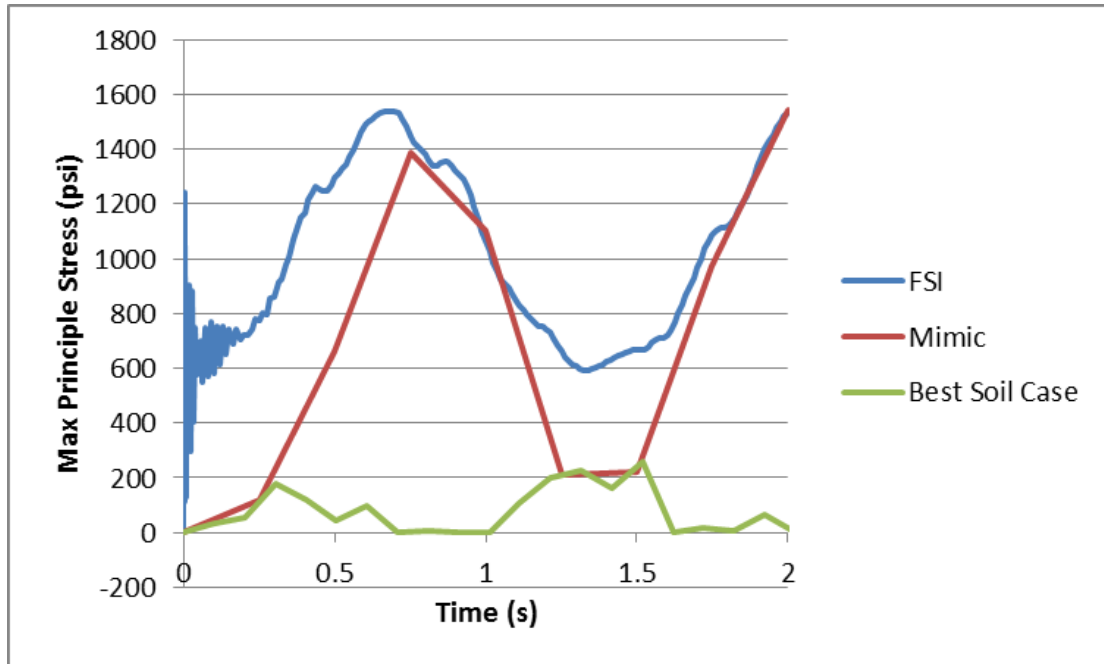


Figure 5.6 Stress vs. Time Graph for Maximum Desirability

When compared to the FSI and Mimic cases, a smaller free span stress response is evident at the location of the end of the effective length.

Another useful profiler is the interaction profiler, which portrays how each variable interacts with each other. Figure 5.7 shows the interaction profiles resulting from the Box-Behnken DOE performed.

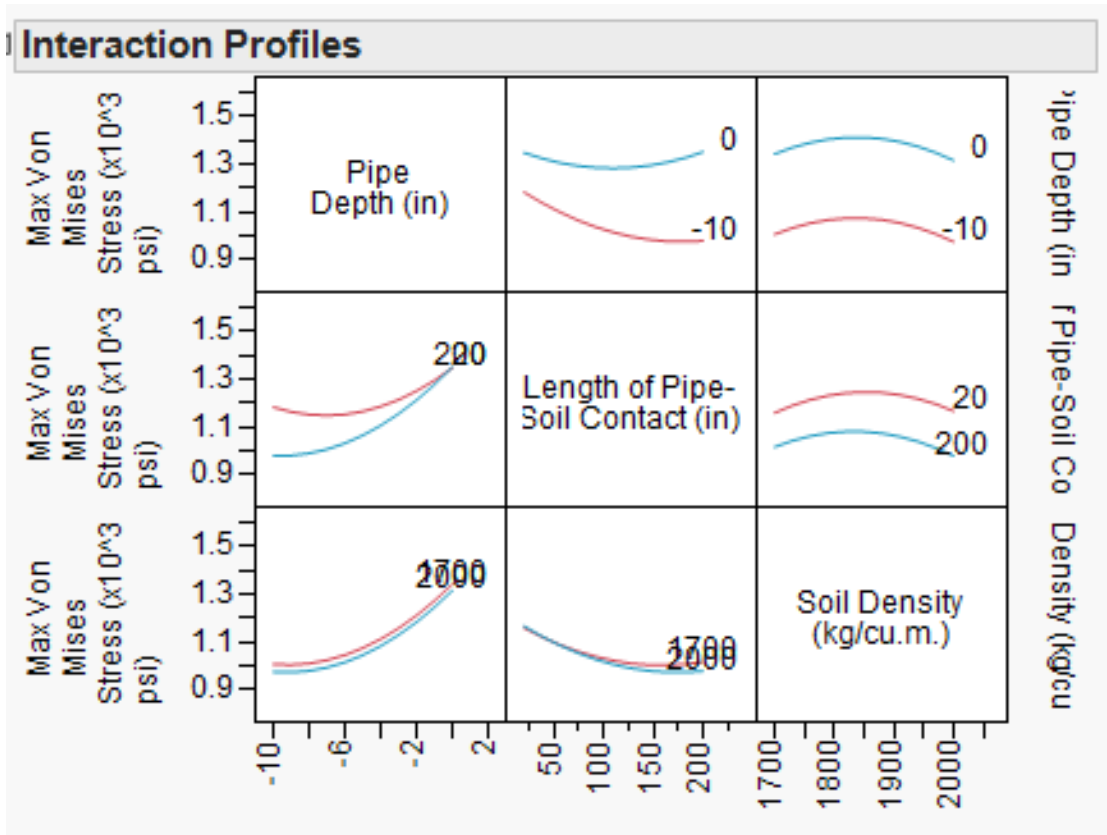


Figure 5.7 Interaction Profiles

The most notable interaction is the length of Pipe-Soil Contact variable with the Pipe Depth variable. At a pipe depth of zero (i.e. the pipe is on top of the soil), the length of pipe-soil contact is not a factor in the stress response.

5.4 Fatigue

The fatigue life of the span could be calculated using the rain flow counting methodology provided by ASTM E1049, and fatigue life can be determined based on S-N curves from DNV-RP-C203 “Fatigue Strength Analysis of Offshore Steel Structures”.

The author recommends analyzing the stresses at both ends of the spans as well the midspan to avoid miscalculations of the fatigue life of the free span.

5.5 The Palmgren-Miner Rule

The Palmgren-Miner Rule is a linear damage rule that calculates fatigue damage based on the sum of number stress cycles at a specific stress range divided by the number of cycles to failure at that stress range:

$$D_{\text{fat}} = \sum \frac{n_i}{N_i}$$

where D_{fat} is the accumulated fatigue damage, n_i is the total number of stress cycles corresponding to the (mid-wall) stress range S_i , and N_i is the number of cycles to failure at stress range S_i (DNV-RP-F105). Along with the rain flow counting procedure, the Palmgren-Miner rule may be used for fatigue life calculations. To obtain a fatigue life, an estimate must be made using any S-N curve (e.g. BS 7608 or DNV C203).

6 Conclusions

The objective of this thesis is to develop a more realistic numerical model than current methodologies for free span stability of submarine pipelines based on fatigue analysis. This was done by using commercial FE and CFD codes to determine the dampening effects from the pipe-soil interaction at the ends of a free span undergoing oscillation due to VIV.

A very challenging aspect in these computational models is effectively and accurately modeling the soil behavior as soil behavior is extremely difficult to predict. The soil density discrepancies in the DOE analysis may be due to the fact that density is not the only parameter that sand and clay have different. Other parameters may include void ratios, angle of friction, cohesion, dilation angle, and drained or undrained conditions, which are further discussed in Appendix K.

The sensitivity results (Figure 5.3) show a non-linear relationship exists as more soil is modeled along the ends of the span. This was not expected as only the elastic response of the soil was modeled. More tests need to be performed to verify if such a non-linear relationship exists before testing the soil's plasticity region.

The DOE screening results (Figure 5.1) suggest that pipe embedment has the most effect on lowering the maximum stress response of the free span undergoing oscillation. The opposite effect was expected, for the soil was thought to act as a fixed end of the pipe at the effective length. If the soil does not have the effect of a fixed boundary condition when the span is entrenched, modeling a free span with fixed boundary conditions at its effective length may lead to unnecessary corrective assessment.

By taking into account the effect of pipe-soil interaction at the end of the free span beyond the effective length, it was found that the soil reduces the magnitude of the stresses at the ends of the free span as shown in Figure 5.6. This newly found mitigation of stresses due to the free span's interaction with the soil at its ends could aid in the design of subsea pipelines and the assessment of free span corrective action.

The methodology proposed in this thesis attempts to more realistically model subsea pipeline free spans, and this methodology may lead to more cost savings for the oil and gas industry if experimental validation proves the stress mitigation effect that the soil has on the free span.

7 Recommendations and Future Work

The thesis provides a computational methodology to analyze free spans while factoring in the effects of pipe-soil interaction. This methodology is not yet validated with benchmark experiments. Limited literature exists studying the incorporating of soil in VIV assessment of free spans. Before improving the methodology described in this thesis and improving computational methods to analyze soil, experiments should be performed to prove or disprove the effect pipe embedment, soil type and amount of soil analyzed along the ends of the pipe have on a free span's stress response to VIV. Limitations of the Mohr-Coulomb model is presented in appendix M. Additional soil parameters must be modeled to more realistically capture soil's permeability and plastic response, so soil may not be able to be realistically modeled with the Mohr-Coulomb model.

After experiments are performed for validating computational models, the combining the FSI and CEL simulations should be the next priority. To accomplish this co-simulation, the CEL soil response has to be calculated at every iteration of the FSI coupling between STAR-CCM+ and ABAQUS. Future analysis should focus on combining the FSI and CEL simulations to more accurately determine the stress results.

Once the FSI and CEL analyses can be fully integrated, future work can include combining the analysis of external flow, pipe-soil interaction and internal flow (see Figure 7.1) on subsea pipelines.

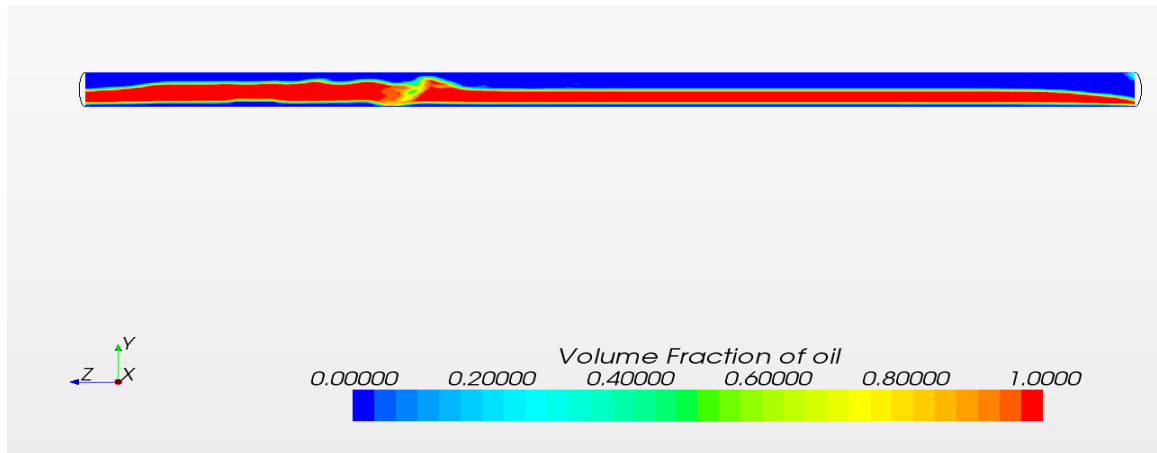


Figure 7.1 Internal Slug Flow within a Subsea Pipeline

References

ABAQUS Version 6.7 Extended Functionality Documentations, 2007.

Abdalla, B., Pike, K., Eltaher, A., Jukes, P., and Duron B. Development and Validation of a Coupled Eulerian Lagrangian Finite Element Ice Scour Model. Proceedings of the ASME 28th International Conference on Offshore Mechanics and Arctic Engineering. (2009): 1-9.

Al-Jamal, Helmi N. Two-Dimensional Numerical Study with LES Modeling of Vortex Induced Vibration of a Circular Cylinder Subjected to a Uniform Flow at a Moderate Reynolds Number. Thesis. University of Houston, 2002.

Bhalla, Kenneth, and Lixin Gong. Managing Vortex Induced Vibration in Well Jumper Systems. Proceedings of the ASME 27th International Conference on Offshore Mechanics and Arctic Engineering. OMAE2008, Estoril, Portugal. Print.

Blevins, Robert D. Flow-induced Vibration. New York: Van Nostrand Reinhold, 1990. Print.

Blevins, Robert D. Formulas for Natural Frequency and Mode Shape. New York: Van Nostrand Reinhold, 1979. Print.

Chica, L., Pascali, R., Jukes, P., Ozturk, B., Gamino, M., and Smith, K. Detailed FSI Analysis Methodology for Subsea Piping Components. Proceedings of the ASME 31st International Conference on Offshore Mechanics and Arctic Engineering. (2012): 1-11.

Cherif, Fares and Pacali, Raresh. Fundamentals of Pipeline Design using Abaqus 6.8.3. University of Houston. 2008.

“Free Spanning Pipelines”. FatFree. Det Norske Veritas. February 2006.

- Helwany, Sam. Applied Soil Mechanics with ABAQUS Applications. Hoboken, New Jersey: John Wiley & Sons, 2007. Print.
- Hesar, M. Pipeline-Seabed Interaction in Soft Clay. Proceedings of the ASME 23rd International Conference on Offshore Mechanics and Arctic Engineering. (2004): 1-9.
- Holmes, Samuel. Et. Al. "Using CFD to study the effects of staggered buoyancy on drilling riser VIV". Proceedings of the ASME 27th International Conference on Offshore Mechanics and Arctic Engineering. OMAE2008, Estoril, Portugal. Print.
- Izarra, Rafael. Second Moment Modelling for the Numerical Simulation of Passive Scalar Dispersion of Air Pollutants in Urban Environments. Diss. Siegen., 2009.
- Jaeger, J. C., N.G.W. Cook, and R.W. Zimmerman. Fundamentals of Rock Mechanics. Malden, MA: Blackwell, 2007. Print
- Lienhard, John H. Synopsis of Lift, Drag, and Vortex Frequency Data for Rigid Circular Cylinders. Pullman, WA: Technical Extension Service, Washington State University, 1966. Print.
- PLAXIS-GiD. Materials Models Manual v1.
- Nair, Aravind, Raj Kadiyala, Alan Whooley, Ayman Eltaher, and Paul Jukes. Vortex Induced Vibration (VIV) Analysis of Multi-planar Jumpers. Tech. no. IOPF 2010:3001. MCS Kenny, Houston, 2010. Web. 14 Dec. 2011. <<http://www.asme-ipti.org/attachments/files/189/Kadiyala--2010-3001.pdf>>.
- Palmer, Andrew Clennel, and Roger A. King. Subsea Pipeline Engineering. Tulsa, Okla: PennWell, 2008.
- Schlichting, Hermann. Boundary-layer Theory. New York: McGraw-Hill, 1968. Print.
- "Shell Perdido." FMC Technologies. Web. 14 Dec. 2011.
<<http://www.fmctechnologies.com/en/SubseaSystems/GlobalProjects/NorthAmerica/US/ShellPerdido.aspx>>.

Silling, S. A. (1993). Simulation of Penetration and Perforation with CTH, Advances in Numerical Simulation Techniques for Penetration and Perforation of Solids. American Society of Mechanical Engineers, Applied Mechanics Division, 57-66.

“Standard Practices for Cycle Counting in Fatigue Analysis.” ASTM E1049 – 85(2011)e1.

Star CCM+ Training. “Lectures CCM+.” CD-Adapco offices. Houston, TX 15 Jul. 2011.

Sumer, B. Mutlu., and Jørgen Fredsøe. Hydrodynamics around Cylindrical Structures. Singapore [u.a.: World Scientific, 1997. Print.

Techet, A. H. "Separated Viscous Flows & Vortex Induced Vibrations." Fall 2005. Lecture.

Timoshenko, Stephen, and J. N. Goodier. Theory of Elasticity. New York: McGraw-Hill, 1970. Print.

Vandiver, K., and Lee, L. SHEAR7 V4.4 Program Theoretical Manual. Massachusetts Institute of Technology, 25 March, 2005.

“Verification Document”. FatFree. Det Norske Veritas. February 2006.

Wang, James F. Wang, Steven, Duan, Gang, and Jukes, Paul. “VIV Analysis of Pipelines under Complex Span Conditions.” Deepwater Offshore Specialty Symposium. 2009.

"Welding Inspection Services, Certified Coating Inspections, NonDestructive Examination and Testing, Pipe Mill Inspections." Engineering Expert Witness Testimony Failure Analysis Litigation Support Texas. Web. 15 Dec. 2011. <<http://www.engineering-experts.com/inspections.html>>.

VIV Equations and Definitions

VIV (Vortex-Induced Vibration): Vibrations caused by forces on the body from the vortices shed from the body, which shed alternatively from top and bottom. “No software or codes exist that accounts for torsional VIV damage assessment” [1], and this torsional stress in multi-planar structures should not be ignored; however, torsion only causes about 7% of damage to studied short jumper systems [1].

Vortices: “are small “eddies” that result in a force on the body” [7]. “When the flow separates, vortices are shed in the wake” [7].

Vortex Shedding Frequency: “vortices are shed alternately at either side of the cylinder at a certain frequency” [6]. The vortex street is laminar for the range of the Reynolds number $40 < Re < 200$, and it does not vary in the spanwise direction [6]. “The transition to turbulence occurs in the wake region” when Re increases beyond 200 [6]. “At $Re = 400$, the vortices, once formed are turbulent” [6]. “For $Re > 300$, the wake is completely turbulent” [6]; however, “the boundary layer over the cylinder surface remains laminar... for increasing Re over a very wide range of Re , namely $300 < Re < 3 \times 10^5$ ” [6]. “This regime is known as the subcritical flow regime” [6]. “With a further increase in Re , transition to turbulence occurs in the boundary layer itself. The transition first takes place at the point where the boundary layer separates, and then the region of transition to turbulence moves upstream over the cylinder surface towards the stagnation point as Re is increased” [6]. “In the narrow Re band $3 \times 10^5 < Re < 3.5 \times 10^5$, the boundary layer becomes turbulent at the separation point, but this occurs only at one side of the cylinder. So the boundary layer separation is turbulent at one side of the cylinder and laminar at the other side. This flow regime is called the critical (or the lower transition) flow regime. The flow asymmetry causes a non-zero mean lift on the cylinder” [6]. “The side at which the separation is turbulent switches from one side to the other occasionally” [6]. “Therefore, the lift changes direction, as the one-sided transition to turbulence changes side, shifting from one side to the other” [6]. “The next Reynolds number regime is the so-called supercritical flow regime where $3.5 \times 10^5 < Re < 1.5 \times 10^6$. In this regime, the boundary layer separation is turbulent on both sides of the cylinder. However, transition to turbulence in the boundary layer has not been completed yet; the region of transition to turbulence is located somewhere between the stagnation point and the separation point” [6]. “The boundary layer on one side becomes fully turbulent when Re reaches the value of about 1.5×10^6 . So, in this flow regime, the boundary layer is completely turbulent on one side of the cylinder and partly laminar and partly turbulent on the other side” [6]. “This type of flow regime, called the upper-transition flow regime, prevails over the range of Re , $1.5 \times 10^6 < Re < 4.5 \times 10^6$ ” [6]. Finally, when Re is increased so that $Re > 4.5 \times 10^6$, the boundary layer over the cylinder surface is virtually turbulent everywhere. This flow regime is called the transcritical flow regime” [6].

VIV Equations and Definitions

Vortex shedding: “The most important feature of the flow regimes described in the previous section is the vortex-shedding phenomenon, which is common to all the flow regimes for $Re > 40$. For these values of Re , the boundary layer over the cylinder surface will separate due to the adverse pressure gradient imposed by the divergent geometry of the flow environment at the rear side of the cylinder. As a result of this, a shear layer is formed” [6]. “The boundary layer formed along the cylinder contains a significant amount of vorticity. This vorticity is fed into the shear layer formed downstream of the separation point and causes the shear layer to roll up into a vortex with a sign identical to that of the incoming vorticity” [6]. “Likewise, a vortex, rotating in the opposite direction, is formed at the other side of the cylinder” [6]. “The larger vortex presumably becomes strong enough to draw the opposing vortex across the wake. The vorticity in Vortex A is in the clockwise direction, while that in Vortex B is in the anti-clockwise direction” [6].

Natural Frequency of the Structure (λ): “The frequency at which a linear elastic structure will tend to vibrate once it has been set into motion. A structure can possess many natural frequencies. The lowest of these is called the fundamental natural frequency. Each natural frequency is associated with a mode shape of deformation. Natural frequency can be defined either in terms of cycle per second (hertz) or radians per second. There are 2π radians per cycle.

Mode Shape (\mathbf{v}): “A function defined over a structure which describes the relative displacement of any point on the structure as the structure vibrates in a single mode. A mode shape is associated with each natural frequency of a structure. If the deflection of a linear vibrating structure in some direction is denoted by $Y(x,t)$, where x is a point on the structure and t is time, then if the structure vibrates only in the k mode, the deflection can be written as

$$Y(x,t) = \tilde{y}_k(x) \tilde{y}_k(t),$$

where $\tilde{y}_k(x)$ is the mode shape, which is a function only of space, and $\tilde{y}_k(t)$ is a function only of time. If the structure vibrates in a number of modes, the total displacement is the sum of the modal displacements:

$$Y(x,t) = \sum_{i=1}^N \tilde{y}_i(x) \tilde{y}_i(t) \quad [7].$$

“likely to be excited by shedding frequencies (current) identified by a velocity screening analysis. Mode shapes [are] classified with respect to the structural planes” [1].

Modal Analysis: identifies a structure’s natural frequency and mode shapes [1].

Eigen Value: See Natural Frequency of the Structure.

Eigen Pair: “Solve $K \cdot \mathbf{v} = \lambda \cdot M \cdot \mathbf{v}$ for each eigenpair” in modal analysis [1].

VIV Equations and Definitions

Eigenvector: See Mode Shape.

Vorticity: a measure of the rotational velocity of fluid elements

- The vorticity vector is the curl of the velocity vector

An ideal fluid: a fluid without viscosity

Inviscid: zero viscosity

Incompressible: constant density

Dot Product: used to obtain the cosine of the angle between two vectors

Cross Product: has a vector as its result, which is perpendicular to both of the vectors being multiplied and normal to the plane containing them. If either of the vectors being multiplied is zero or if the vectors are parallel, then their cross product is zero.

Curl: is a vector operator that represents the exceedingly small rotation of a 3-D vector field.

The motion of ideal fluid in a reservoir is governed by three sets of equations [5]:

1. Equation of continuity (conservation of mass)
2. Euler's equation (conservation of momentum)
3. Boundary conditions as surfaces

Free Spans: caused by:

- Seabed unevenness
- Change of seabed topology (e.g. scouring, sand waves)
- Artificial supports/rock beams etc.
- Strudel scours [2]

Galloping: a hydrodynamic loading phenomena

Net fluid force on a body: “is the sum of the normal pressure and tangential shear stress summed over the surface of the body.”

Added Mass: “largely independent of viscosity” [5] “is the mass of fluid entrained by the cylinder” and it is a component of fluid force on the cylinder” [5]. “Lift in phase with acceleration” [7]. “The fluid added mass increases the effective structural mass for dynamic analysis” [5].

Reduced Velocity: “The reduced velocity parameter relates the current speed with the vibration frequency and diameter of the jumper” [3].

VIV Equations and Definitions

Lock-in Situation: where the natural frequency of the structure equals the vortex shedding frequency, and maximum displacement occurs when this lock-in situation occurs.

Strouhal Number: dictates vortex shedding [7]. It is a dimensionless number describing oscillating flow mechanisms.

Courant number: a lower time step will equal a lower Courant number, and a greater time step will increase the Courant number

Keulegan-Carpenter number: “used for oscillating flow, such as ocean waves” [5]. This number is “identical in form to the reduced velocity but with U defined as the amplitude of velocity of a flow that oscillates with frequency f about a structure of diameter D .”

Reynolds Number: [see equations]

Streamlines: “A streamline is tangent to the flow. No fluid flows across a streamline” [5]. (“The cylinder itself is a streamline. In fact, any of the streamlines can be interpreted as a solid surface” [5])

Sources, sinks, or centers of vorticity: singularities and are “points in the flow field at which the potential function is infinite and its differentials are not defined” [5].

Orthogonal: intersection or lying at right angles

Quasi-static process: a process that happens indefinitely slowly

Discrete vortex method (DVM): a numerical method for modeling two-dimensional, inviscid flows by vortices. Unfortunately, this technique is limited to two-dimensional flows.

Planar Jumpers: Vertical and M shaped jumpers [1].

Gradient: the gradient of a scalar field is a vector field that points in the direction of the greatest rate of increase of the scalar field, and whose magnitude is the greatest rate of change.

Cross Flow Induced Cross Vibration: “amplitudes are in the order of 1 diameter” [1].

Cross Flow Induced Inline Vibration (In-Line Vibration): Vibration amplitudes are typically 30-50% of cross flow induced cross vibration [1].

Pure In-line Vibration (In-Line Vibration): Vibration amplitudes are typically in the order of 10-15% of the diameter [1].

VIV Equations and Definitions

Current Analysis Methods: Response Based Models, Force Based Models (Shear7) and Flow Based Models (CFD) [1].

- Response Based Models
 - Dominated by vortex induced resonance
- Empirical Models (DNV FatFree): Uniform flow around a Cylinder
 - Sheared Flow
- Force Based Models (Shear7): Cross Vibration
 - Morison's equation
 - Inline Vibration
 - Dominated by hydrodynamic loads (eg. Direct wave loads)
- Flow Based Models (CFD):
 - Promising but relatively new
 - Not conservative compared with other prediction models

Fluid Coupling: “fluid provides added mass but also coupling between the structures” when one structure is adjacent to another and fluid fills the gap between the two [5]. “When one structure is set into motion, the adjacent structure tends to vibrate” [5].

Explicit methods: calculate the state of a system at a later time from the state of the system at the current time.

Implicit methods: find a solution by solving an equation involving both the current state of the system and the later one. Implicit methods require extra computation, and they are usually harder to implement. In many cases, an implicit scheme is very complicated and no exact solution exists. Solves for equilibrium.

NO SLIP CONDITION: requires that the velocity of the fluid at the wall matches the velocity of the wall, such that it does not “slip” along the boundary [7].

Friction drag: the drag on the plate (wall) caused by the transfer of momentum between the fluid particles slows the flow down [7].

Form drag (pressure drag): arises because of the form of the object [7]. It opposes forward motion and is a component of the total drag.

VIV Equations and Definitions

References:

- 1.) Nair, Aravind. Et. Al. Vortex Induced Vibration (VIV) Analysis of Multi-Planar Jumpers. MCSKenny. IOPF 2010.
- 2.) Veritas, Det Norske. Free Spanning Pipelines. DNV. February 2006.
- 3.) Bhalla, Kenneth. Gong, Lixin. Managing Vortex Induced Vibration in Well Jumper Systems. OMAE2008-57026.
- 4.) Holmes, Samuel. Et. Al. Using CFD to study the effects of staggered buoyancy on drilling riser VIV. OMAE2008-57434.
- 5.) Blevins, Robert D. Flow-Induced Vibration. 2nd Ed. Van Nostrand Reinhold, New York. 1990.
- 6.) Sumer, B. Mutlu., and Jørgen Fredsøe. Hydrodynamics around Cylindrical Structures. Singapore: World Scientific, 1997. Print.
- 7.) Techet, A.H. Separated Viscous Flows & Vortex Induced Vibrations. Fall 2005.
- 8.) Blevins, Robert D. Formulas for Natural Frequency and Mode Shape. Van Nostrand Reinhold Company. Litton Educational Publishing, Inc. 1979.

VIV Equations and Definitions

Fineness ratio: $\frac{l}{D} = \frac{\text{length}}{\text{width}}$

Aspect ratio: $\frac{\text{length in the third dimension}}{\text{width}}$

Reduced velocity: $\frac{U}{fD} = \frac{\text{path length per cycle}}{\text{model width}}$

Where:

- U = the free stream velocity
- f = the frequency of vibration
- * the inverse of reduced velocity is the Nondimensional frequency
- * if reduced velocity is between 2 and 8, then the model often interacts strongly with vortex shedding in its own wake.
- * “The two nondimensional parameters that are closely related to reduced velocity are Keulegan-Carpenter number and Strouhal number” [5].

Dimensionless amplitude: $\frac{A_y}{D} = \frac{\text{vibration frequency}}{\text{model width}}$

Where:

- A_y = the amplitude of the vibration

Strouhal number: $S = \frac{f_s D}{U}$

Where:

- “ f_s is the frequency of periodic vortex shedding from a structure of diameter D in a steady flow of velocity U” [5].

Mass Ratio: $\frac{m}{\rho D^2} = \frac{\text{mass per unit length of model}}{\text{fluid density} \times \text{model width}^2}$

Where:

- M ordinarily includes structural mass and the “added mass” of fluid entrained (i.e. pulled or drawn in along after itself) by the moving model
- *the mass ratio “is a measure of the relative importance of buoyancy and added mass effects on the model” [5].
- *the mass ratio “is often used to measure the susceptibility of lightweight structures to flow-induced vibration” [5].
- * “As the ratio of fluid mass to structural mass increases, so does the propensity of flow-induced vibration” [5].

VIV Equations and Definitions

Reynolds Number: $\frac{UD}{\nu} = \frac{\text{inertial force}}{\text{viscous force}}$

Where:

- ν = “the kinematic viscosity of the fluid and is equal to the absolute viscosity divided by the density” [5].
- The viscous forces retard the boundary layer next to the structure (slows it down)
- * “The Reynolds number, abbreviated Re, scales the boundary layer thickness and transition from laminar to turbulent flow” [5].

Mach Number: $\frac{U}{c} = \frac{\text{fluid velocity}}{\text{speed of sound}}$

Where:

- c = the speed of sound in the fluid
- Mach number measures the tendency of fluid to compress as it encounters a structure

Turbulence Intensity: $\frac{u_{rms}}{U} = \frac{\text{root mean square turbulence}}{\text{free stream fluid velocity}}$

Where:

- The Turbulence intensity measures the turbulence in the flow

Damping factor: $\zeta = \frac{\text{energy dissipated per cycle}}{4\pi \times \text{total energy of structure}}$

Where:

- The energy dissipated by a structure as it vibrates is characterized by its damping factor

Mass damping (a.k.a. reduced damping or Scruton number) can be formed by the product of mass ratio and the damping factor:

$$\text{Reduced damping} = \frac{2m(2\pi\zeta)}{\rho D^2}$$

Where:

- “Increasing reduced damping ordinarily reduces the amplitude of flow-induced vibrations”

Added mass for lateral acceleration for a Circular cylinder of radius “a” = $\rho\pi a^2 b$

The velocity vector is the gradient of the velocity potential [5]

$$\mathbf{V} = \vec{\nabla} \phi$$

VIV Equations and Definitions

“This equation implies that lines of constant ϕ (potential lines) are normal to the velocity vector” [5].

Vorticity: a measure of the rotational velocity of fluid elements [5]

The vorticity vector is the curl of the velocity vector [5]

$$\omega = \bar{V} \times V$$

*The vorticity vector in a potential flow is zero since the curl of the gradient of any continuous, differentiable function is identically zero [5]:

$$\bar{V} \times V = \bar{V} \times (\bar{V} \phi) = 0$$

*Singular points are associated with sources of vorticity [5]

Wall shear stress:

$$\tau_w = \mu \frac{\delta u}{\delta y} \big|_{y=0}$$

Friction Drag Coefficient:

$$C_f = \frac{F}{\frac{1}{2} \rho U^2 A_w}$$

Reynolds number of a boundary layer:

$$Re_x = \frac{Ux}{\nu}$$

Drag Force on the body due to viscous effects:

$$F_D = \frac{1}{2} \rho C_D A U^2$$

Where:

- C_D is found empirically through experimentation, depends on Reynolds number, and is quite different in laminar vs. turbulent flows [7].
- A is profile (frontal) area

VIV Equations and Definitions

Vortex Shedding frequency

$$\omega_v = 2\pi f_v = 2\pi S_t(U/d)$$

OR

$$f_s = \frac{S*U}{D}$$

Where:

- f_s = the shedding frequency
- d = outside diameter

Natural frequency of oscillation

$$\omega_n = \sqrt{\frac{k}{m + m_a}}$$

Pressure Coefficient

$$C_p = \frac{p - p_\infty}{\frac{1}{2}\rho_\infty V_\infty^2}$$

p = the pressure at the point where the pressure coefficient is being evaluated

p_{infinite} = the pressure in the freestream

ρ_{infinite} = freestream fluid density

V_{infinite} = the freestream velocity of the fluid

$$\text{Courant Number} = \frac{(u)(\Delta t)}{(\Delta x)}$$

Where:

- u = is the velocity
- Δt = the time step
- Δx = the length interval

VIV Equations and Definitions

Turbulent energy (k)

$$k = \frac{3}{2} (UI)^2$$

Where:

U = the mean flow velocity

I = the turbulence intensity

Specific Turbulent Dissipation Rate (ω)

$$\omega = \frac{\sqrt{k}}{l}$$

Where:

k = turbulent energy

l = turbulent length scale

Dissipation rate (ε)

$$\varepsilon = C_u \left(\frac{k^{3/2}}{l} \right)$$

Where:

C_u = a turbulence model constant which usually has a value of 0.09

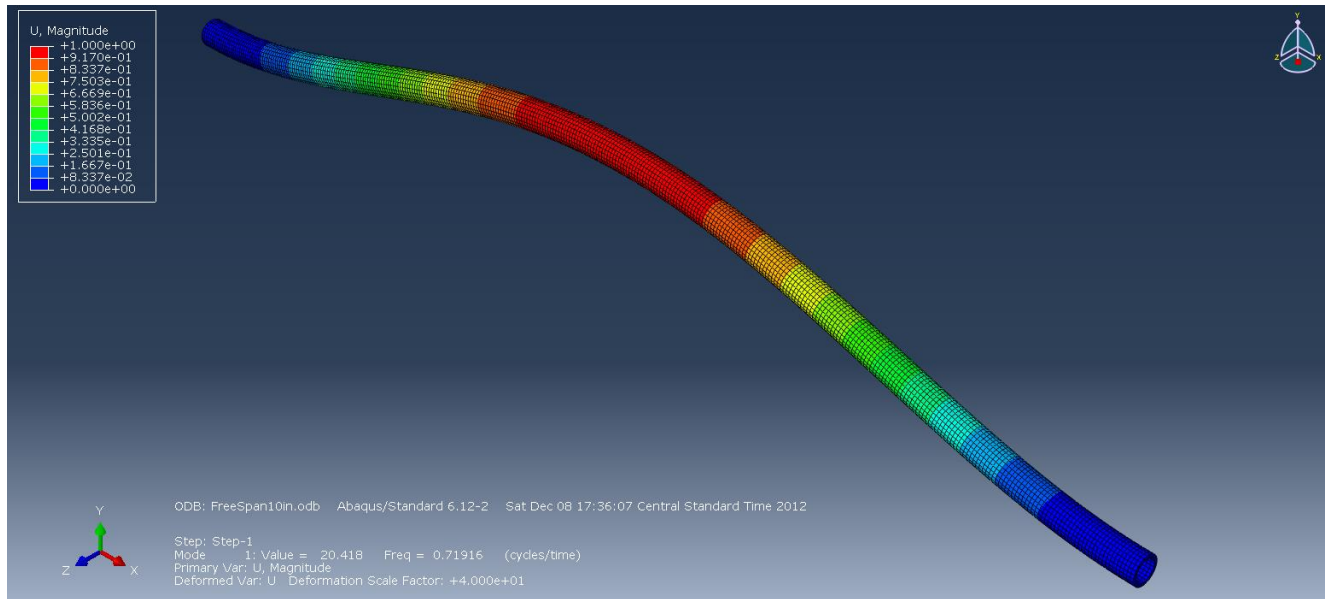
VIV Equations and Definitions

References:

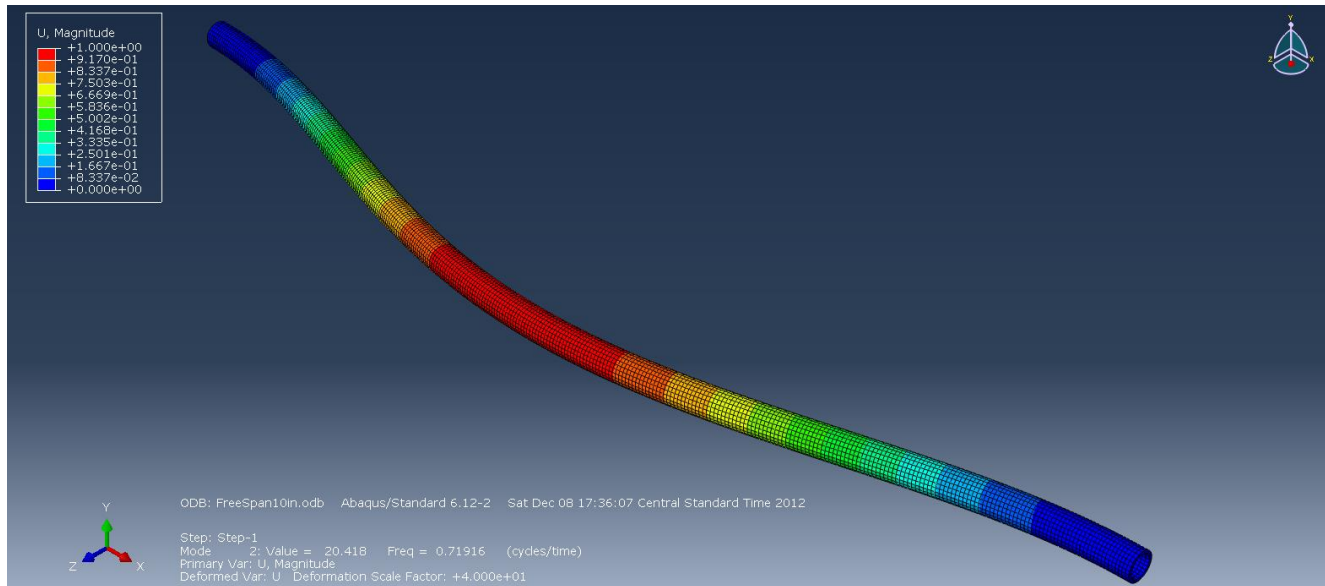
- 9.) Nair, Aravind. Et. Al. Vortex Induced Vibration (VIV) Analysis of Multi-Planar Jumpers. MCSKenny. IOPF 2010.
- 10.) Veritas, Det Norske. Free Spanning Pipelines. DNV. February 2006.
- 11.) Bhalla, Kenneth. Gong, Lixin. Managing Vortex Induced Vibration in Well Jumper Systems. OMAE2008-57026.
- 12.) Holmes, Samuel. Et. Al. Using CFD to study the effects of staggered buoyancy on drilling riser VIV. OMAE2008-57434.
- 13.) Blevins, Robert D. Flow-Induced Vibration. 2nd Ed. Van Nostrand Reinhold, New York. 1990.
- 14.) Sumer, B. Mutlu., and Jørgen Fredsøe. Hydrodynamics around Cylindrical Structures. Singapore: World Scientific, 1997. Print.
- 15.) Techet, A.H. Separated Viscous Flows & Vortex Induced Vibrations. Fall 2005.

Natural Frequency Results from ABAQUS

Mode 1:

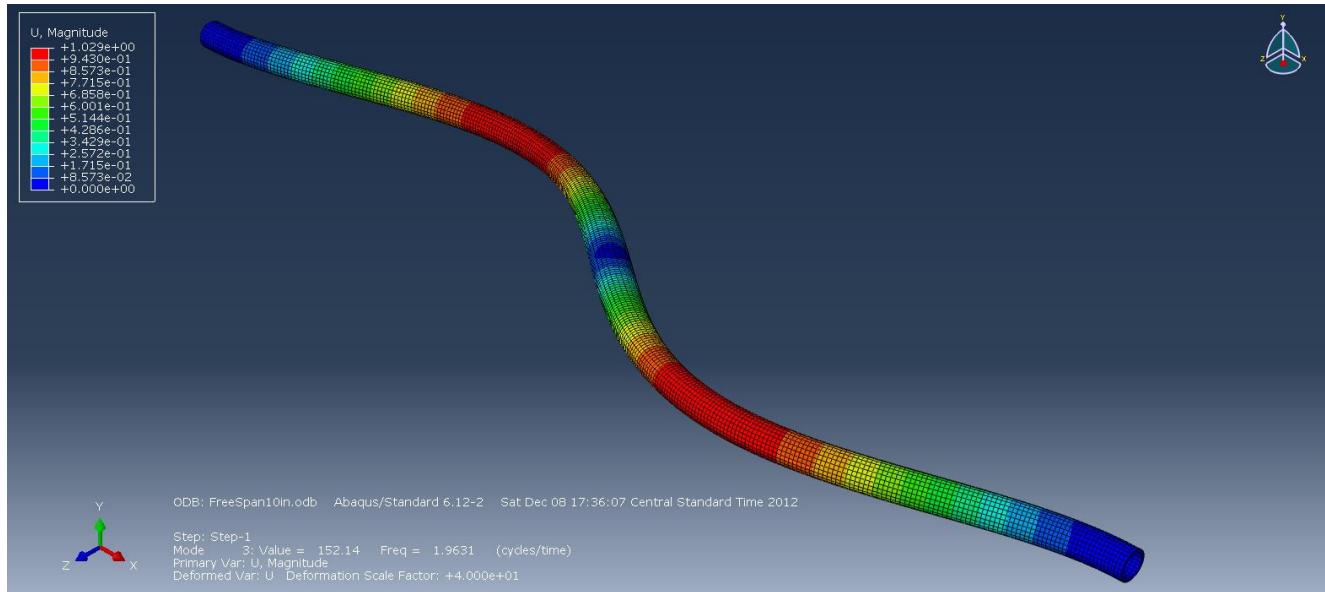


Mode 2:

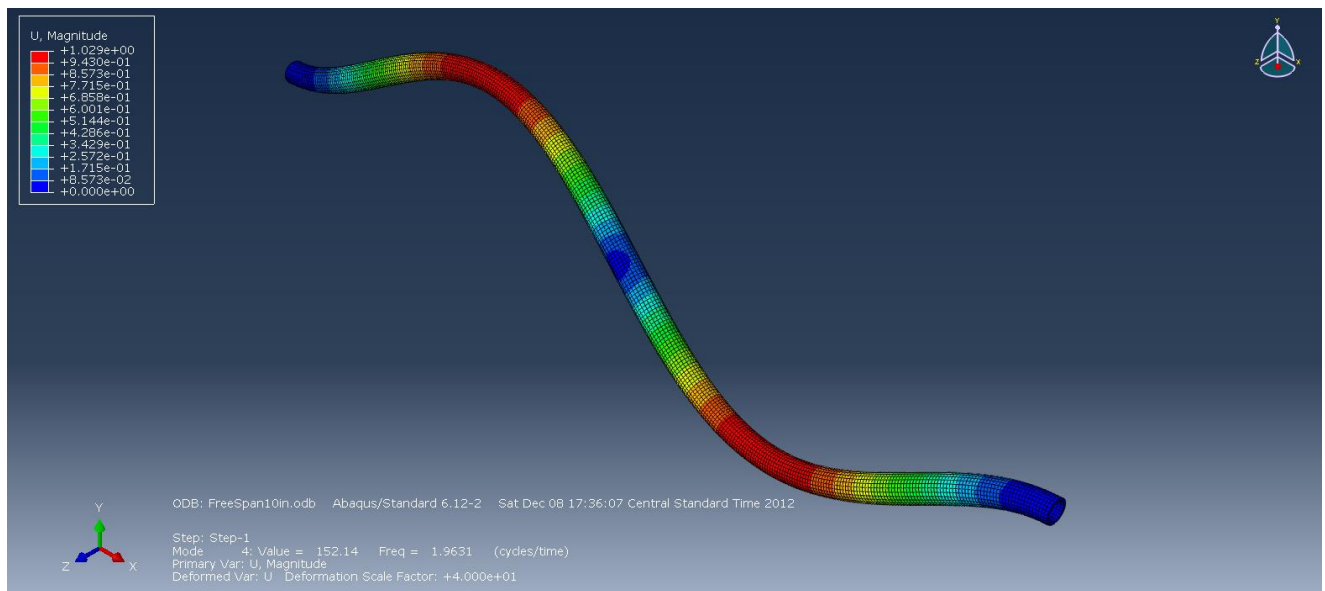


Natural Frequency Results from ABAQUS

Mode 3:

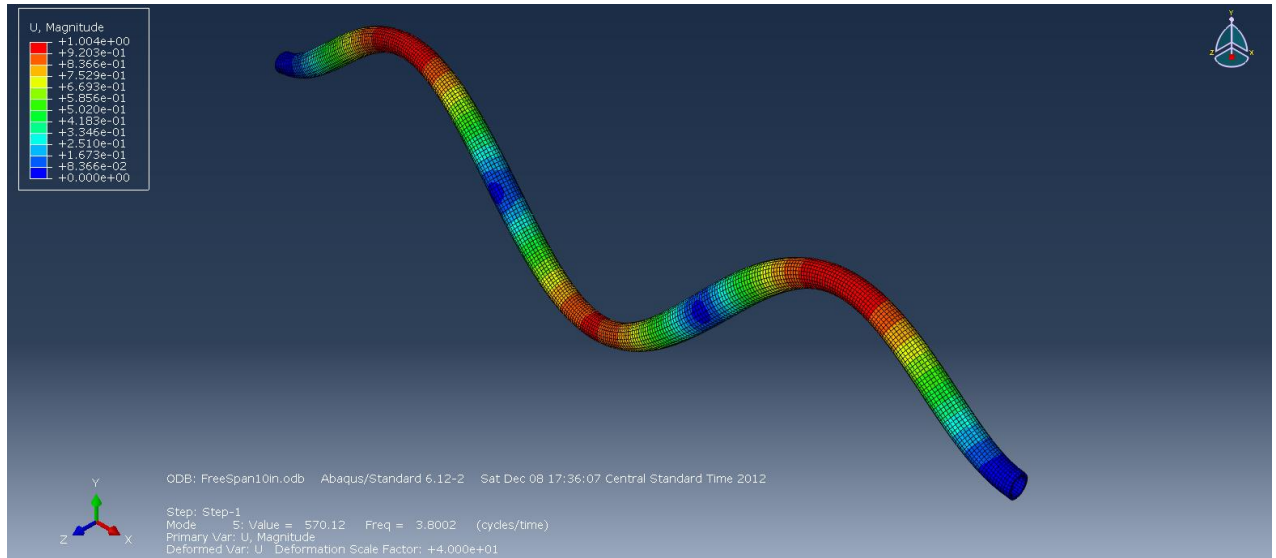


Mode 4:



Natural Frequency Results from ABAQUS

Mode 5:



Mode	Natural Frequency (cycles/time)
1	0.71916
2	0.71916
3	1.9361
4	1.9631
5	3.8002

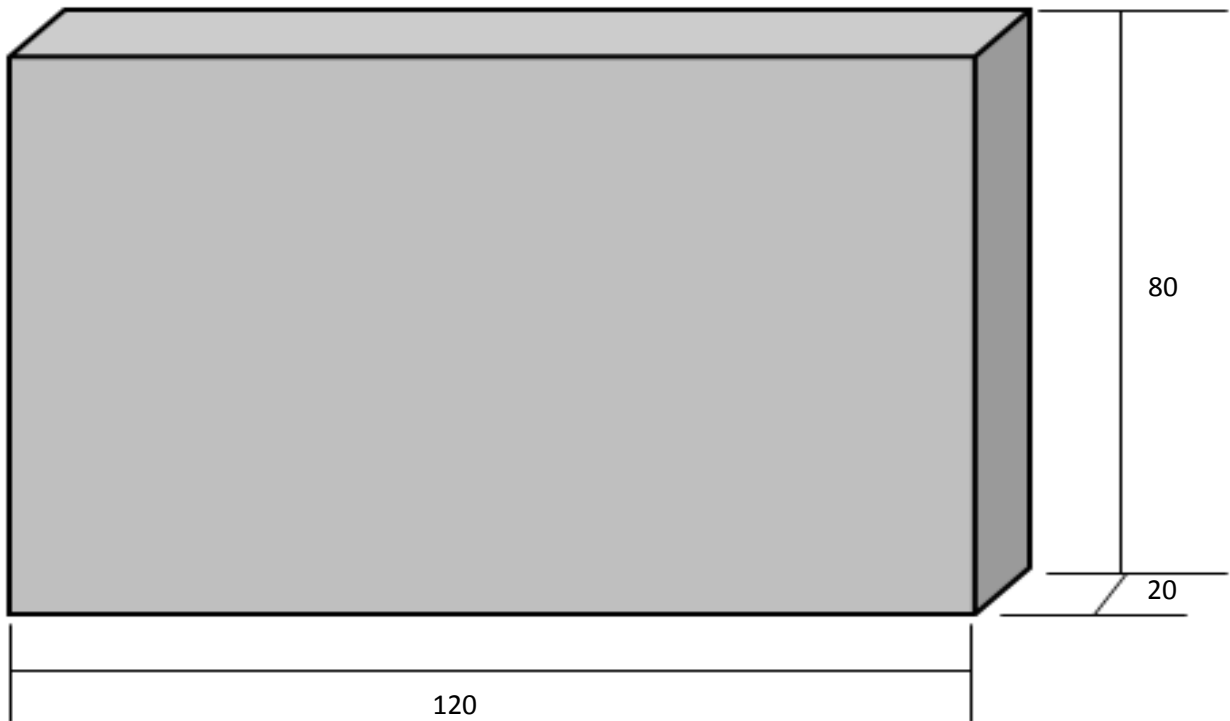
Final X, Y, and Z Displacement Data from FSI Simulations

The following data was prescribed on the center of span within the CEL simulations:

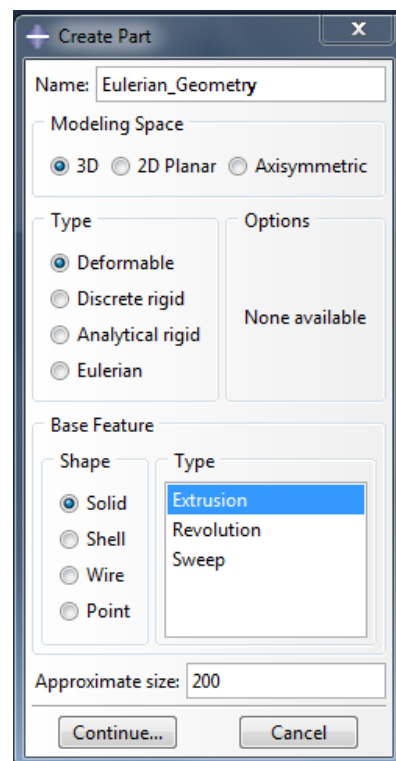
Time	Amp-1x	Time	Amp-1y	Time	Amp-1z
0	0	0	0	0	0
0.00951	-1.95E-05	9.51E-03	9.12E-06	0.00951	2.26E-06
0.0563	-0.000161	0.0563	0.000678	0.0563	3.22E-05
0.15	-0.000912	0.15	0.005	0.15	3.17E-05
0.275	-0.00276	0.275	0.0177	0.275	0.00011
0.4	-0.00282	0.4	0.0314	0.4	0.000103
0.525	-0.00269	0.525	0.0447	0.525	9.74E-05
0.65	-0.000753	0.65	0.0505	0.65	0.000115
0.775	0.000863	0.775	0.0499	0.775	0.00016
0.9	0.00296	0.9	0.0403	0.9	0.000121
1.025	0.00372	1.025	0.0272	1.025	5.97E-05
1.15	0.00391	1.15	0.0126	1.15	3.30E-05
1.275	0.00275	1.275	0.00278	1.275	6.34E-05
1.4	0.000979	1.4	-0.000476	1.4	5.03E-05
1.525	-0.00101	1.525	0.00474	1.525	2.61E-05
1.65	-0.00269	1.65	0.0164	1.65	4.69E-05
1.775	-0.00311	1.775	0.0307	1.775	0.000114
1.9	-0.00293	1.9	0.044	1.9	0.000144
2.025	-0.00126	2.025	0.0508	2.025	0.000113

Benchmark Pipe-Soil Interaction Procedure

Step 1: Create the Eulerian Geometry



*Create a 3D Eulerian Extruded Solid



Benchmark Pipe-Soil Interaction Procedure

Step 2: Create Eulerian materials (the soil)

“The model requires inputting the following input parameters: modulus of elasticity E , the Poisson ratio, angle of internal friction and cohesion. The latter two parameters serve to define the yield condition. The formulation of constitutive equations assumes effective parameters of angle of internal friction ϕ_{eff} and cohesion c_{eff} . The angle of dilation must also be specified” (“Angle of Dilation.” *Fine – Civil Engineering Software*. N.p., n.d. Web. 12 Dec. 2012.).

Material name: Soft_Clay

Density: 0.06684psi

Young’s Modulus 2175.56607psi

Poisson’s Ratio: 0.49

Friction Angle: 0°

*The friction angle represents at which angle an object begins to slide.

Dilation Angle: 0

*Necessary for non-cohesive soils. This angle controls an amount of plastic volumetric strain developed during plastic shearing and is assumed constant during plastic yielding. The value of $\psi = 0$ for the dilation angle corresponds to the volume preserving deformation while in shear. (“Angle of Dilation.” *Fine – Civil Engineering Software*. N.p., n.d. Web. 12 Dec. 2012.)

Cohesion = 0.0145psi

*represents the cohesion between particles and is a stress independent component.

Abs Plastic Strain: 0

*absolute value of the corresponding plastic strain. (The first tabular value entered must always be zero in Abaqus.)

Step 3: Create the Pipe

Outside Radius: 5in

Inside Radius: 4in

Extrude Depth: 10in



Benchmark Pipe-Soil Interaction Procedure

Step 4: Create the Pipe Material

Material Name: Steel

Density: 0.284psi

Young's Modulus: 30E6psi

Poisson's Ratio: 0.3

Step 5: Assign the Materials

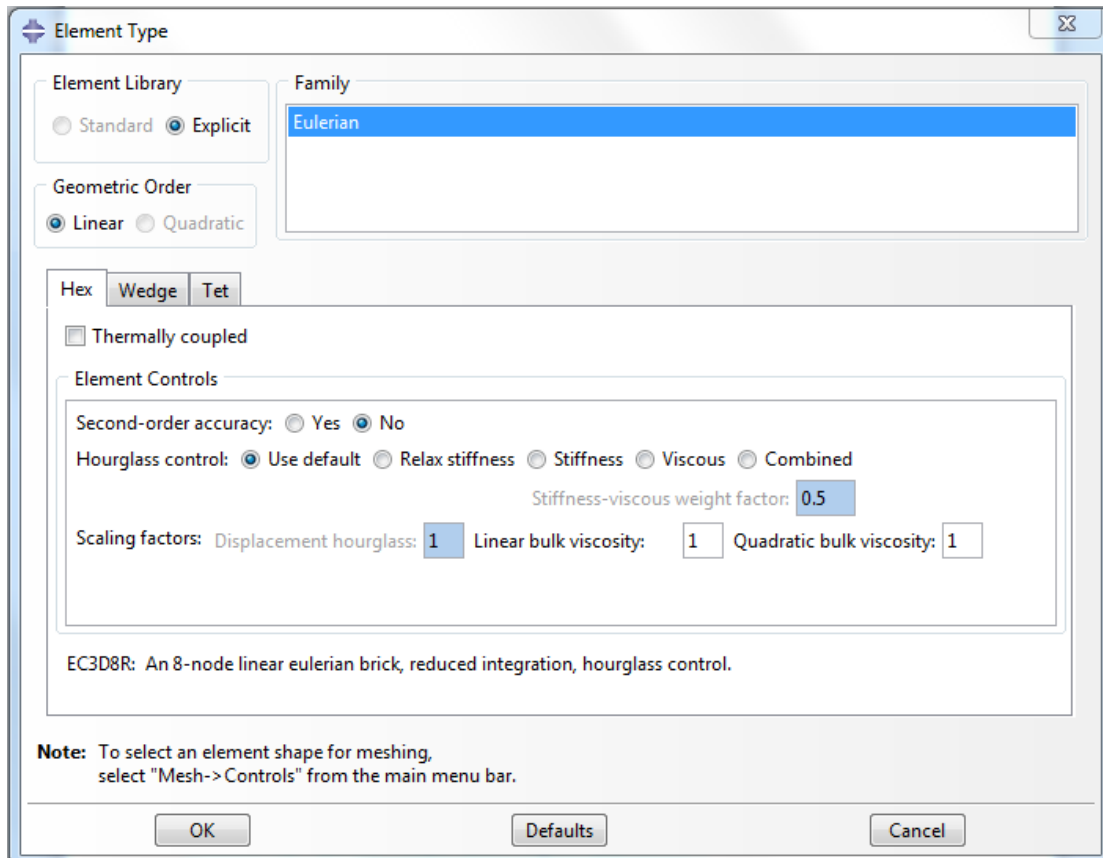
Section Assignments

Step 6: Mesh the Parts as Dependent (within the Parts folder)

Eulerian Mesh: (**Change Global Seed Size from 12 to 2.32 - # of nodes should be around 18,500)

*Use EC3D8R Brick Elements

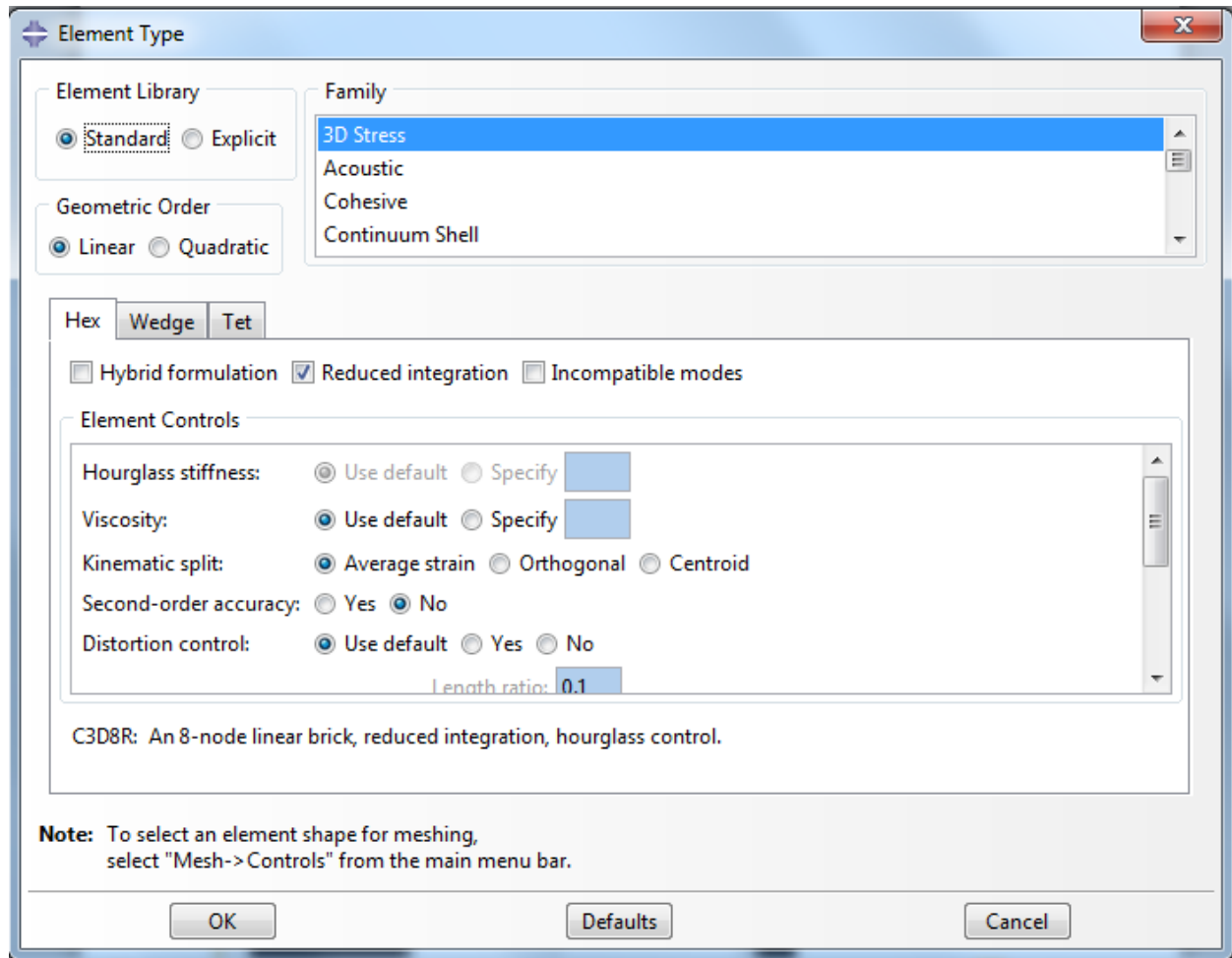
Benchmark Pipe-Soil Interaction Procedure



Pipe Mesh:

*Use C3D8R Brick Elements

Benchmark Pipe-Soil Interaction Procedure



Seed Edges 34 by number

Should have around 1000 nodes.

Benchmark Pipe-Soil Interaction Procedure

Step 7: Create the Dependent Part Instances

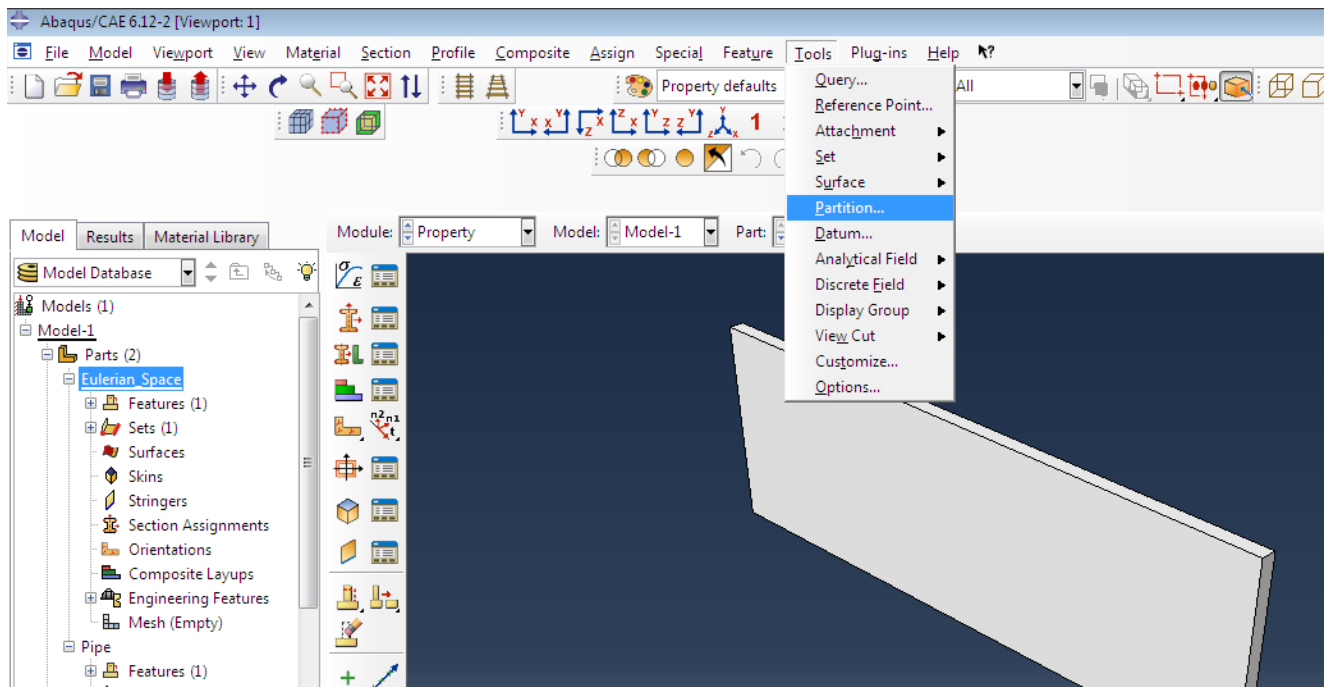


*Translate the Pipe 60inches in the positive X-direction, 5inches in the negative Y-direction, and 5inches in the positive Z-direction

Step 8: Partition the Eulerian Domain in two sections (Tools>Partition)

Partitioning the Eulerian Geometry

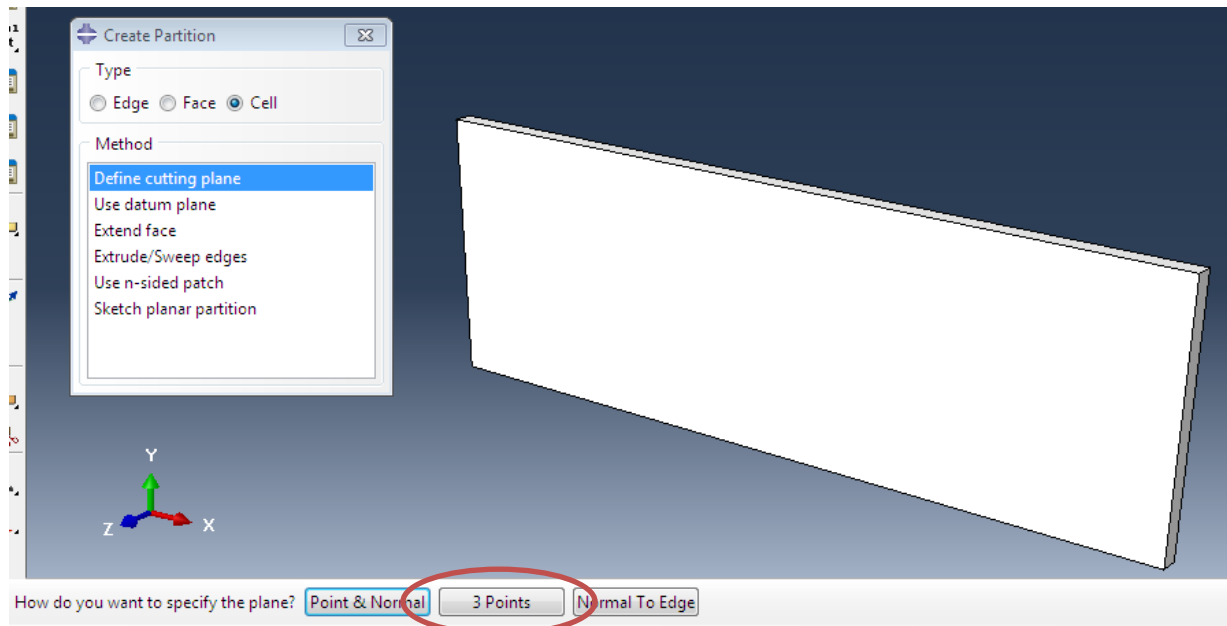
Tools>Partition



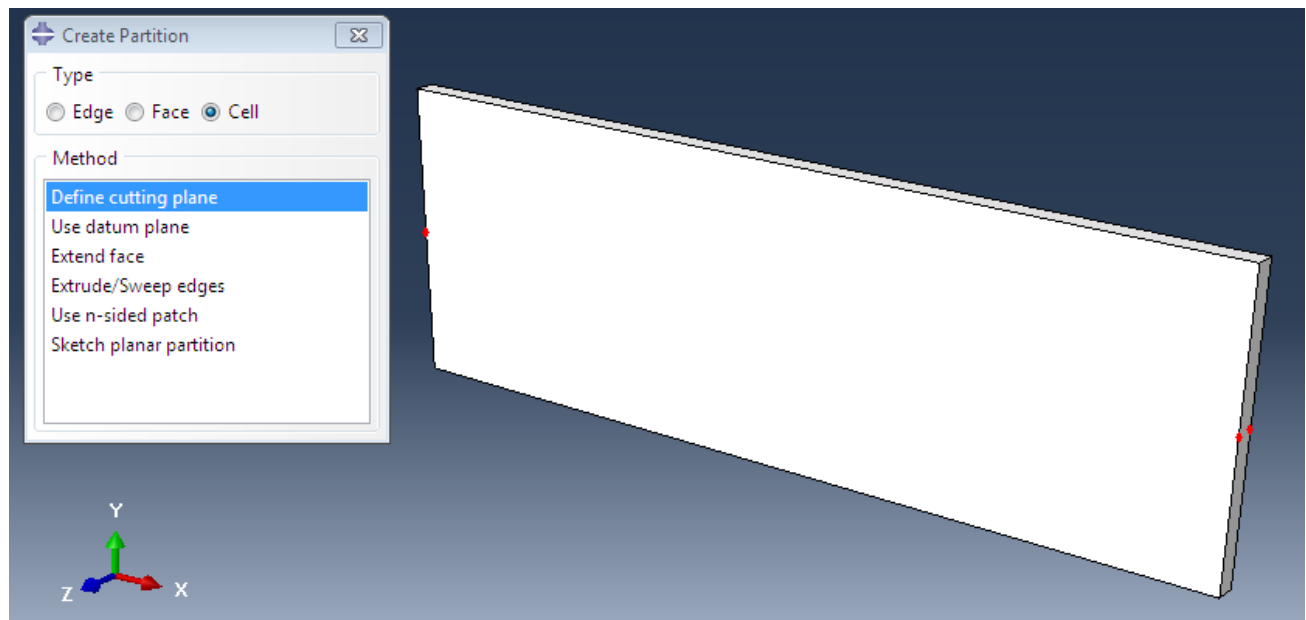
Benchmark Pipe-Soil Interaction Procedure

Select Cell

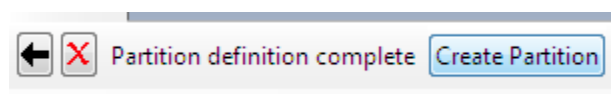
Partition with 3 points:



Select 3 points on the center of the outer edges as shown:



Select Create Partition>Done

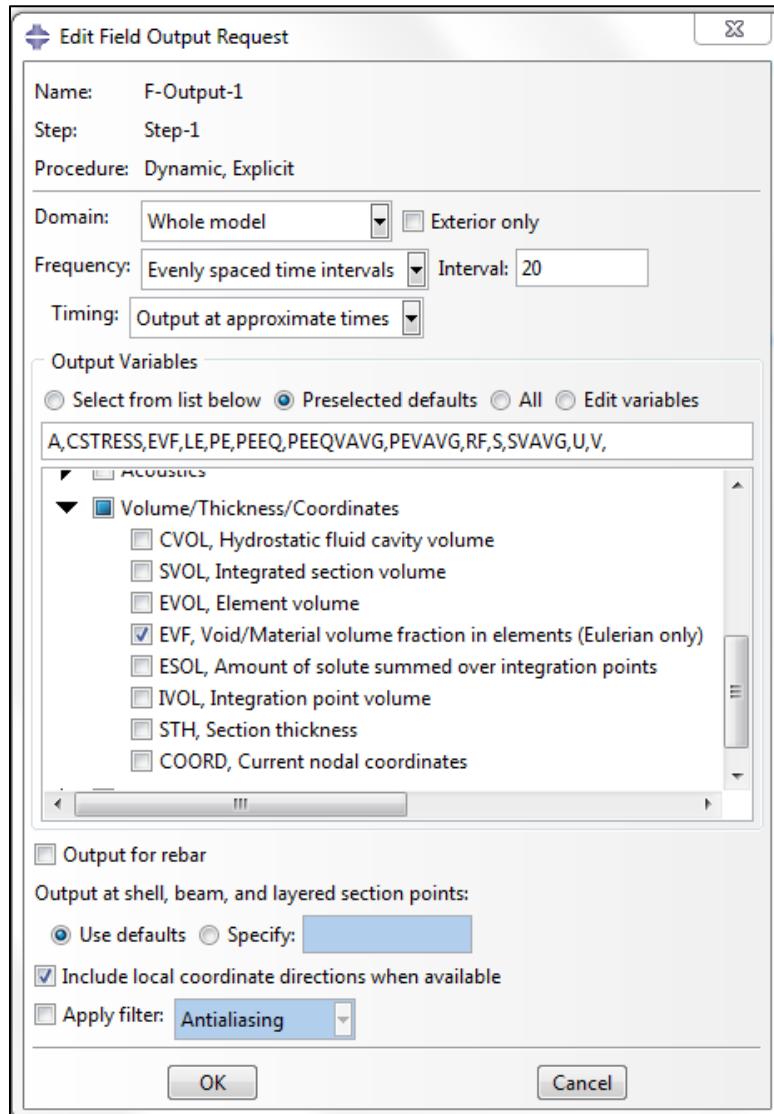


Benchmark Pipe-Soil Interaction Procedure

Step 9: Create 2 new sets (one for the upper half of the Eulerian domain, and one for the bottom half)

Step 10: Create a new Dynamic Explicit Analysis with a set time period

Step 11: Enable EVF within the Field Output Request Window:



Benchmark Pipe-Soil Interaction Procedure

Step 12: Set Interaction Properties:

Edit Contact Property

Name: IntProp-1

Contact Property Options

Tangential Behavior

Mechanical Thermal Electrical

Tangential Behavior

Friction formulation: Penalty

Friction Shear Stress Elastic Slip

Directionality: ☒ Isotropic ☐ Anisotropic (Standard only)

☐ Use slip-rate-dependent data

☐ Use contact-pressure-dependent data

☐ Use temperature-dependent data

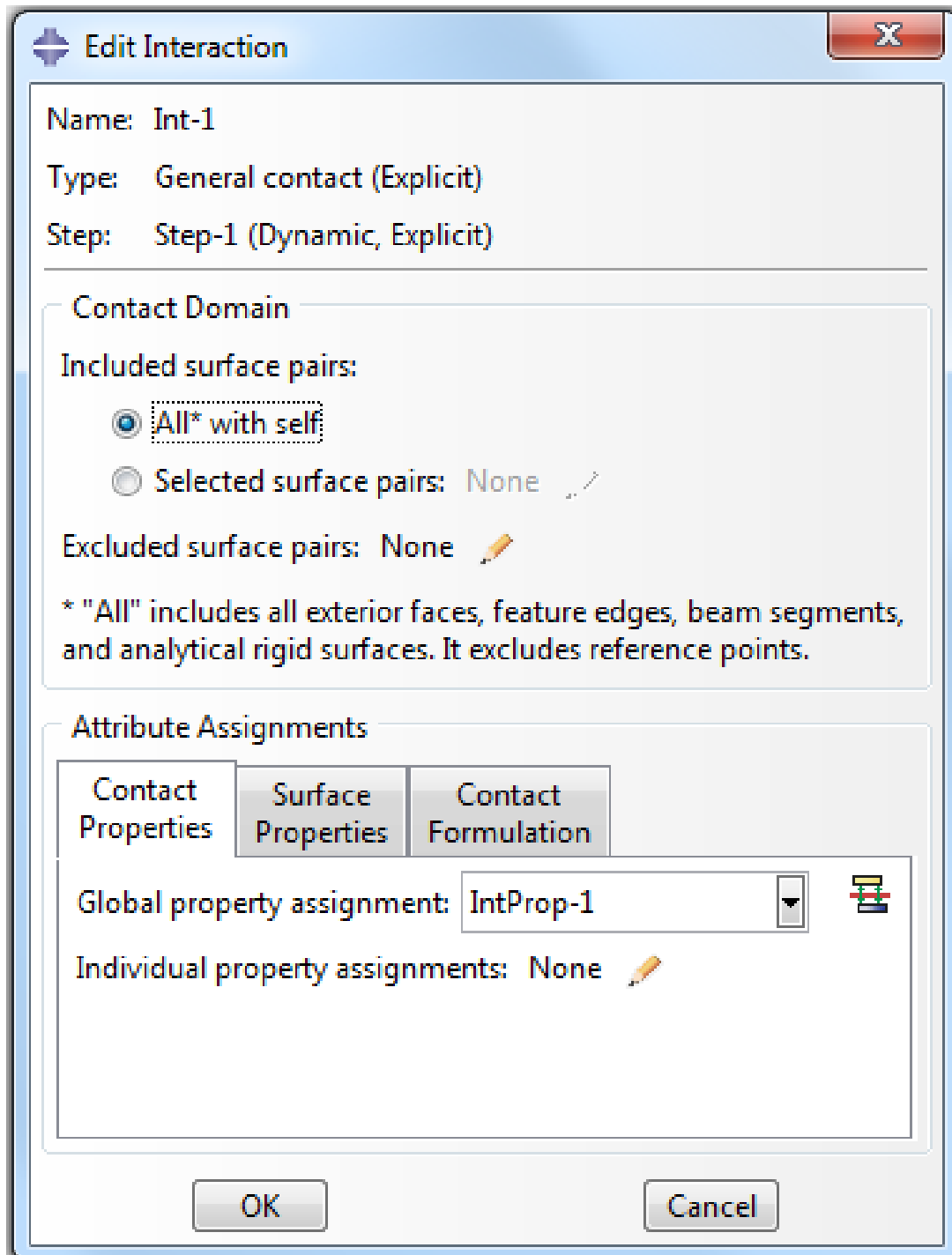
Number of field variables: 0

Friction Coeff
0.32

OK Cancel

Benchmark Pipe-Soil Interaction Procedure

Step 13: Set Interactions (Contact – All with Self)



The image shows a software dialog box titled "Edit Interaction". It contains fields for Name, Type, and Step. The "Contact Domain" section has radio buttons for "All* with self" (selected) and "Selected surface pairs: None". The "Excluded surface pairs" is set to "None". A note explains that "All" includes exterior faces, feature edges, beam segments, and analytical rigid surfaces, but excludes reference points. The "Attribute Assignments" section has tabs for "Contact Properties", "Surface Properties", and "Contact Formulation". Below these, "Global property assignment" is set to "IntProp-1" and "Individual property assignments" is set to "None". "OK" and "Cancel" buttons are at the bottom.

Edit Interaction

Name: Int-1

Type: General contact (Explicit)

Step: Step-1 (Dynamic, Explicit)

Contact Domain

Included surface pairs:

☒ All* with self

☐ Selected surface pairs: None

Excluded surface pairs: None

* "All" includes all exterior faces, feature edges, beam segments, and analytical rigid surfaces. It excludes reference points.

Attribute Assignments

Contact Properties | Surface Properties | Contact Formulation

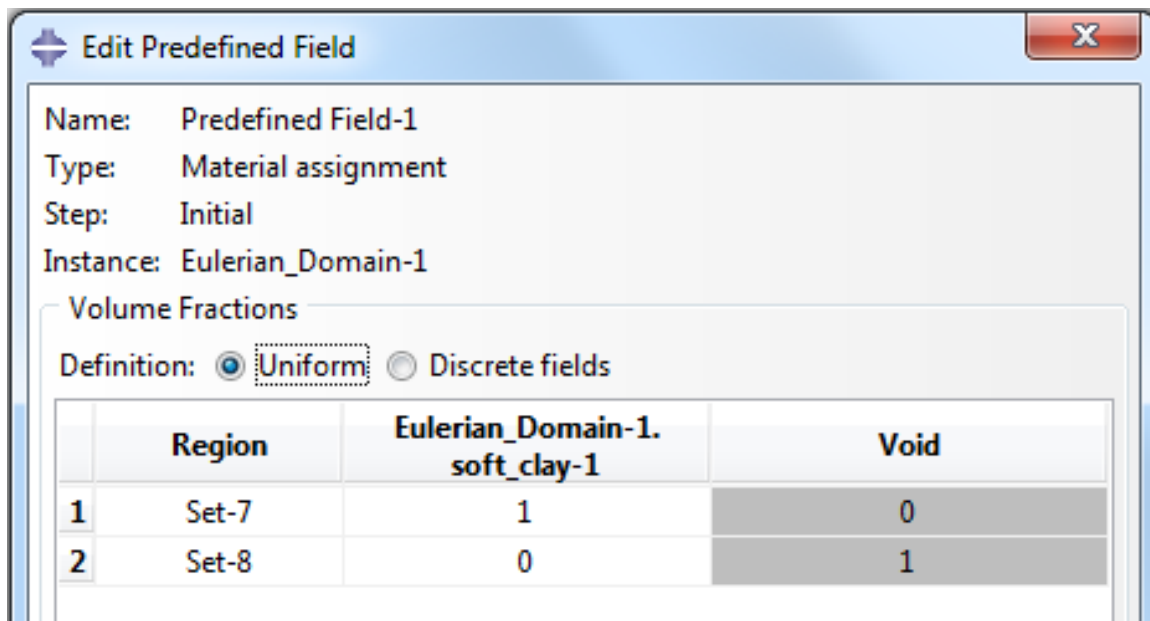
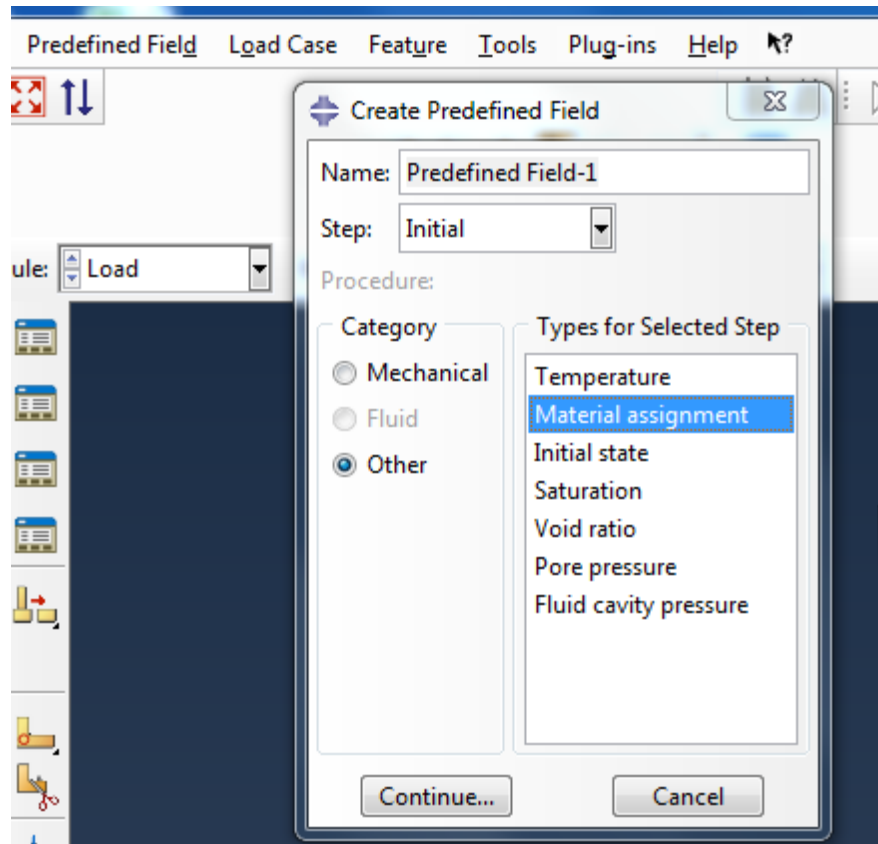
Global property assignment: IntProp-1

Individual property assignments: None

OK Cancel

Benchmark Pipe-Soil Interaction Procedure

Step 14: Create Uniform Predefined Fields (other>material assignment)



*Set-7 equals bottom half of Eulerian Domain, and Set-8 equals top half of Eulerian Domain

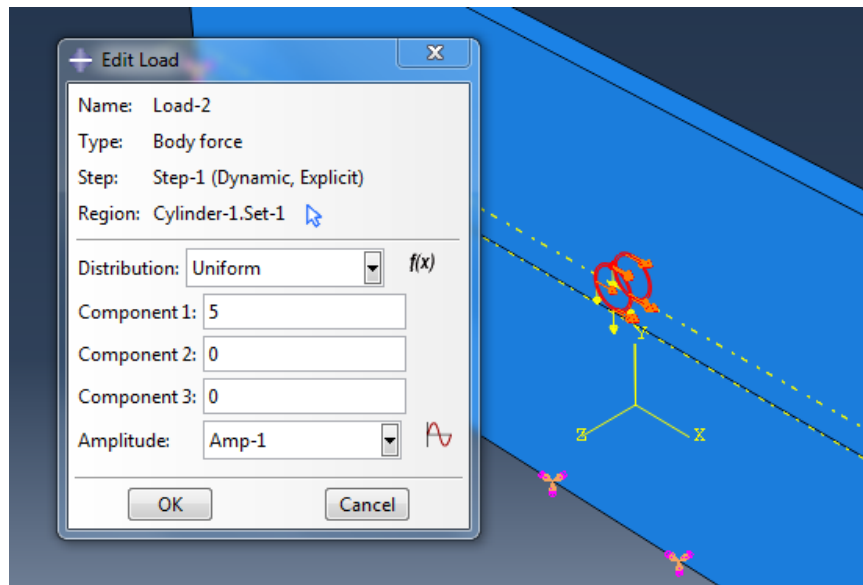
Benchmark Pipe-Soil Interaction Procedure

Step 15: Enable Boundary conditions:

Set zero velocity boundary conditions in the planes normal to the cross-section of the pipe (X-Y Planes in this case).

Step 16: Create Loads in X and Y

Example:



Step 17: Create the Job and Run the Analysis

Soil Sensitivity Studies

Pipe-Soil

Case1: 20xSoil Contact - Pipe on top of soil

Trial	Mesh Strategy	# of nodes	# of elements	Run Time (hours)	Max VM Stress (x10 ⁵ psi)	Location
1	Seed Part: 6	4144	3066	0.05	1.309	Near Mid-Boundary Condition
					1.273	Near End of Span
					1.1186	At Effective Length Location (approx. 20 in from end)
2	Seed Part: 2	97461	88000	0.25	1.379	Near Mid-Boundary Condition
					1.2456	Near End of Span
					1.1192	At Effective Length Location (approx. 20 in from end)
3	Seed Part:1.8	129605	118096	0.3	1.379	Near Mid-Boundary Condition
					1.2451	Near End of Span
					1.1204	At Effective Length Location (approx. 20 in from end)

Soil Sensitivity Studies

Pipe-Soil
Case2: 20xSoil Contact - Half Entrenched

Trial	Mesh Strategy	# of nodes	# of elements	Run Time (hours)	Max VM Stress (x10 ⁵ psi)	
1	1	1093	680	0.33	1.317	
2	2	3759	2320	1.5	1.43	
3	2+3	51069	45952	Does not run		
4	4	104975	92400	0.583	0.88357 1.32184 1.05619	Near Mid-Boundary Condition Near End of Span At Effective Length Location (approx. 20 in from end)
5	5	127155	111906	0.833	0.935659 1.30775 1.05188	Near Mid-Boundary Condition Near End of Span At Effective Length Location (approx. 20 in from end)
6	6	717948	668800	2	0.94369 1.3069 1.05978	Near Mid-Boundary Condition Near End of Span At Effective Length Location (approx. 20 in from end)

Mesh Strategies:

1- None

2 - Partition Eulerian Space every 1-inch along the X-axis

3 - Partition Eulerian Space every 1-inch along the Y-axis

4- Seed Part: 2

5- Seed Part: 1.8

6- Seed Part: 1

Soil Sensitivity Studies

Pipe-Soil

Case3: 20xSoil Contact - Fully Entrenched

Trial	Mesh Strategy	# of nodes	# of elements	Run Time (hours)	Max VM Stress (x10 ⁵ psi)	
1	1	148835	118020	3.83	1.483	
2	2	212160	192280	Does not Run		
3	3	399449	349680	7.75	1.487	
4	2+3	970411	921360	72	4.2*	
5	4	41898	22227	0.5	1.02153	Near Mid-Boundary Condition
					1.495	Near End of Span
					0.927765	At Effective Length Location (approx. 20 in from end)
6	5	112931	100100	2.383	1.09155	Near Mid-Boundary Condition
					1.46936	Near End of Span
					0.9543	At Effective Length Location (approx. 20 in from end)
7	6	129850	114924	2.433	1.0301	Near Mid-Boundary Condition
					1.52457	Near End of Span
					0.989489	At Effective Length Location (approx. 20 in from end)

Mesh Strategies:

1- None

2 - Partition Eulerian Space every 1-inch along the X-axis

3 - Partition Eulerian Space every 0.5-inch along the Y-axis

4- Seed Part: 6

5- Seed Part: 2

6- Seed Part: 1.8

*over 7000 distorted elements by the end of the run

Soil Sensitivity Studies

Pipe-Soil

Case4: 110xSoil Contact - Pipe on top of soil

Trial	Mesh Strategy	# of nodes	# of elements	Run Time (hours)	Max VM Stress (x10 ⁵ psi)	Location
1	Seed Part: 6	18496	10646	0.067	0.601 1.6996 0.70082	Near Mid-Boundary Condition Near End of Span At Effective Length Location (approx. 110 in from end)
2	Seed Part: 2	149823	130320	0.367	0.657745 1.8073 0.69414	Near Mid-Boundary Condition Near End of Span At Effective Length Location (approx. 110 in from end)
3	Seed Part:1.8	182505	166496	0.45	0.63538 1.80587 0.6997	Near Mid-Boundary Condition Near End of Span At Effective Length Location (approx. 110 in from end)

Soil Sensitivity Studies

Pipe-Soil Case5: 110xSoil Contact - Half Entrenched						
Trial	Mesh Strategy	# of nodes	# of elements	Run Time (hours)	Max VM Stress ($\times 10^5$ psi)	Location
1	Seed Part: 20	12045	6176	0.4	0.683488	Near Mid-Boundary Condition
					0.32706	Near End of Span
					0.534479	At Effective Length Location (approx. 110 in from end)
2	Seed Part: 6	158349	135480	1	0.402795	Near Mid-Boundary Condition
					0.532535	Near End of Span
					0.4368	At Effective Length Location (approx. 110 in from end)
3	Seed Part:1	1010988	942400	6.5	0.405357	Near Mid-Boundary Condition
					0.480091	Near End of Span
					0.41877	At Effective Length Location (approx. 110 in from end)

Soil Sensitivity Studies

Pipe-Soil Case 6:		110xSoil Contact - Fully Entrenched				
Trial	Mesh Strategy	# of nodes	# of elements	Run Time (hours)	Max VM Stress (x10 ⁵ psi)	Location
1	Seed Part: 6				Did Not Converge!	Near Mid-Boundary Condition Near End of Span At Effective Length Location (approx. 110 in from end)
2	Seed Part: 1.8	206536	172464	2.4167	0.560835 0.30306 0.420334	Near Mid-Boundary Condition Near End of Span At Effective Length Location (approx. 110 in from end)
3	Seed Part:1	1018873	939816	7.4333	0.555218 0.221912 0.395184	Near Mid-Boundary Condition Near End of Span At Effective Length Location (approx. 110 in from end)

Soil Sensitivity Studies

Pipe-Soil Case 7: 200xSoil Contact - Pipe on top of soil						
Trial	Mesh Strategy	# of nodes	# of elements	Run Time (hours)	Max VM Stress ($\times 10^5$ psi)	Location
1	Seed Part: 6	7504	5586	0.0833	0.879197 1.28029 0.69914	Near Mid-Boundary Condition Near End of Span At Effective Length Location (approx. 200 in from end)
2	Seed Part: 2	176841	160000	0.5167	0.88454 1.28542 0.699699	Near Mid-Boundary Condition Near End of Span At Effective Length Location (approx. 200 in from end)
3	Seed Part:1.8	235405	214896	0.6333	0.885069 1.28587 0.70046	Near Mid-Boundary Condition Near End of Span At Effective Length Location (approx. 200 in from end)

Soil Sensitivity Studies

Pipe-Soil Case 8: 200xSoil Contact - Half Entrenched						
Trial	Mesh Strategy	# of nodes	# of elements	Run Time (hours)	Max VM Stress (x10 ⁵ psi)	Location
1	Seed Part: 6	15765	8096	0.5	0.63878	Near Mid-Boundary Condition
					0.213295	Near End of Span
					0.491555	At Effective Length Location (approx. 20 in from end)
2	Seed Part: 2	179247	157600	2.7	0.412323	Near Mid-Boundary Condition
					0.288071	Near End of Span
					0.416393	At Effective Length Location (approx. 20 in from end)
3	Seed Part:1.8	244907	210740	3.183	0.429915	Near Mid-Boundary Condition
					0.344792	Near End of Span
					0.44164	At Effective Length Location (approx. 20 in from end)

Soil Sensitivity Studies

Pipe-Soil
Case 9: 200xSoil Contact - Fully Entrenched

Trial	Mesh Strategy	# of nodes	# of elements	Run Time (hours)	Max VM Stress (x10 ⁵ psi)	Location
1	Seed Part: 6	46926	25720	failed at 0.96 seconds physical time		Near Mid-Boundary Condition Near End of Span At Effective Length Location (approx. 200 in from end)
2	Seed Part: 2	215855	175872	2.7	0.139871 0.483809 0.554244	Near Mid-Boundary Condition Near End of Span At Effective Length Location (approx. 200 in from end)
3	Seed Part:1.8	231400	205128	3.18	0.559125 0.14053 0.3952	Near Mid-Boundary Condition Near End of Span At Effective Length Location (approx. 200 in from end)

Free Span Sensitivity Studies

Displacement Case 1: 440 inch

Displacement Test Sensitivity Results	Case	Number of Nodes	Number of Elements	Run Time (min)	Max VM Stress (x10 ⁴ psi)	Max Displacement	Mesh Strategy
Displacement Trial 1:	440 inch	15800	9450	1	2.387	1.501	Seed Part: 1
Displacement Trial 2:	440 inch	36162	23321	1	2.475	1.482	Seed Part: 6
Displacement Trial 3:	440 inch	164747	114400	1	2.571	1.463	Seed Part: 5
Displacement Trial 4:	440 inch	247687	185820	2	2.641	1.462	Seed Part: 4.5

Free Span Sensitivity Studies

Displacement Case 2: 620 inch

Displacement Test Sensitivity Results	Case	Number of Nodes	Number of Elements	Run Time (min)	Max VM Stress ($\times 10^4$ psi)	Max Displacement	Mesh Strategy
Displacement Trial 1:	620 inch	169576	120861	1	3.618	4.076	Seed Part: 6
Displacement Trial 2:	620 inch	348887	261820	2	3.7	4.068	Seed Part: 5
Displacement Trial 3:	620 inch	446976	335016	4	3.851	4.065	Seed Part: 4.5

Free Span Sensitivity Studies

Displacement Case 3: 800 inch

Displacement Test Sensitivity Results	Case	Number of Nodes	Number of Elements	Run Time (min)	Max VM Stress (x10 ⁴ psi)	Max Displacement	Mesh Strategy
Displacement Trial 1:	800 inch	218776	155961	1	4.653	8.739	Seed Part: 6
Displacement Trial 2:	800 inch	299387	208000	1	4.635	8.73	Seed Part: 5
Displacement Trial 3:	800 inch	450087	337820	2	4.758	8.721	Seed Part: 4.5
Displacement Trial 4:	800 inch	576576	432216	21	4.951	8.715	Seed Part: 4

DOE Model Evaluation

The results of the space-filling design will depend on the input variables of outside diameter, current velocity, and fluid density. Three different statistical models were chosen to analyze the design space: a space-filling design, a full factorial design at the corners, and a surface response design. For each design, screening was conducted to determine which main effect or combination of effects had the greatest influence on the maximum amplitude of displacement.

Space-filling Design:

The initial model used for this computational experiment was a space-filling design. As mentioned in table 3.4, the advantage of a space-filling design is the even spread of all design points for each input. Figure H1 illustrates an example of the even spread of all design points. As depicted in figure H1, no design point shares the same row or column with another design point.

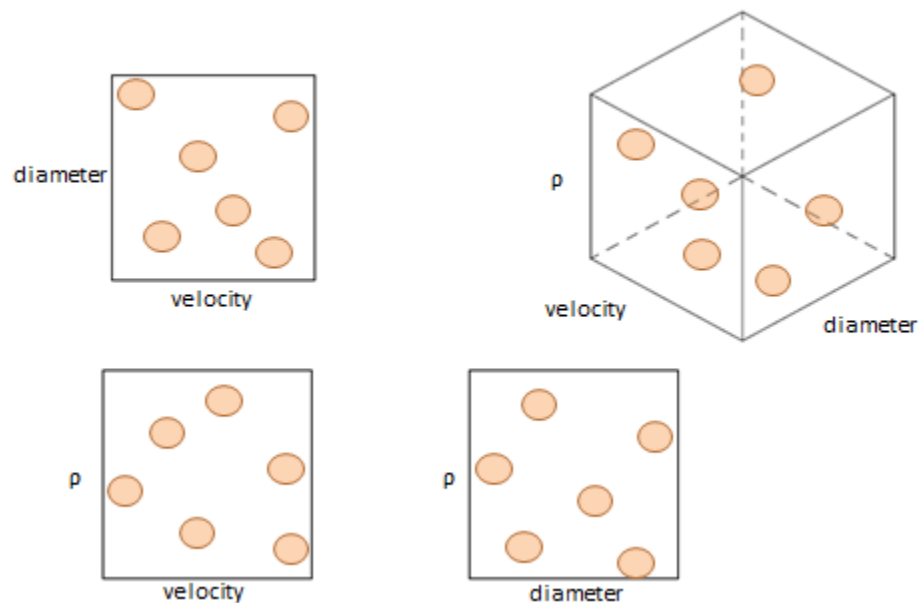


Figure H1: The Spread of the Design Points within a Space-filling Design

After obtaining the design point from JMP, the six FSI simulations were ran and produced the displacement results shown in table 5 on the subsequent page.

DOE Model Evaluation

Table H1: Design Points and Displacement Results from the Space-Filling Design

Run	Pipe Diameter (in.)	Fluid Velocity (m/s)	Density (kg/m ³)	Displacement (in.)
1	12	1.1	937.2758	1.978×10^{-2}
2	8	0.8	876.9906	2.215×10^{-2}
3	11.2	2	816.7054	3.851×10^{-2}
4	10.4	0.5	756.4202	0.7909×10^{-2}
5	8.8	1.4	696.135	3.326×10^{-2}
6	9.6	1.7	997.561	4.816×10^{-2}

The results of the screening for this model showed fluid velocity (i.e. current velocity) has the greatest influence on the maximum amplitude of displacement. Figure H2 reinforces the screening results by illustrating fluid velocity has the greatest effect on the range of displacement versus pipe diameter or density.

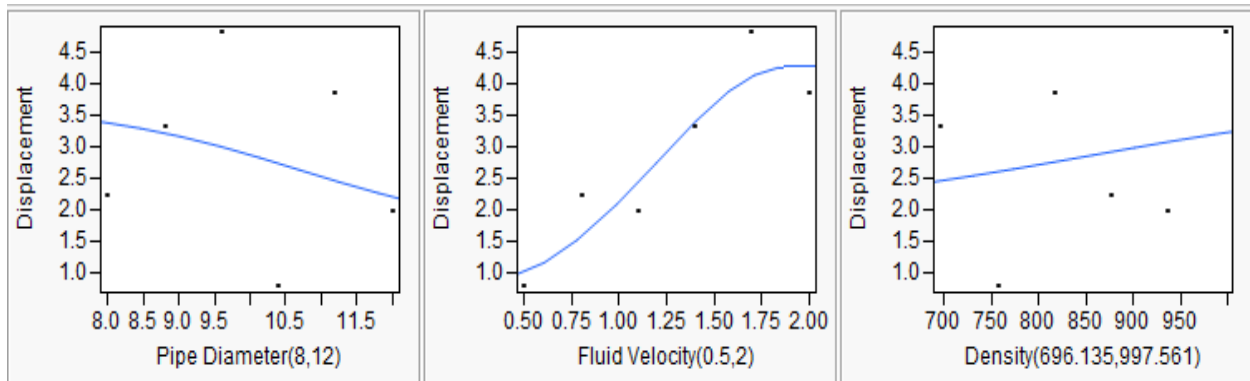


Figure H2: The Effects of Each Input on the Range of Displacement

Table H2 shows the maximum and minimum values of displacement obtained from the JMP software results for the space-filling design. These values will be compared to the maximum and minimum results from the other two DOE models (full factorial at the corners and surface response).

DOE Model Evaluation

Table H2: Maximum and Minimum Displacements from the Space-filling Design Results

Value	Displacement (in)
Maximum	5.086×10^{-2}
Minimum	0.5945×10^{-2}

Further look into the interactions and trends of the three inputs and their effects on displacement can be found in appendix A.

Full Factorial Design at the Corners:

The second model used for this computational experiment was a full factorial design. As mentioned in table 3.4, the advantage of a full factorial design at the corners is the ability to find responses at the maximum and minimum ranges of each design input. Figure H3 illustrates how the nine design points were distributed for this model.

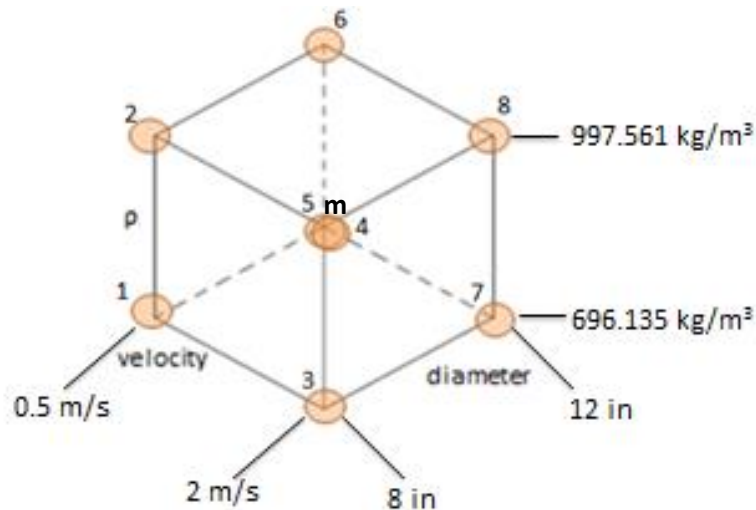


Figure H3: Location of the Nine Design Points for the Full Factorial Design

DOE Model Evaluation

Table H3: Design Points and Displacement Results from the Full Factorial Design

	D_o (in)	v (m/s)	ρ (kg/m³)	Displacement(x10⁻² in)
1	8	0.5	696.135	2.215
2	8	0.5	997.561	1.334
3	8	2	696.135	7.238
4	8	2	997.561	10.36
5	12	0.5	696.135	0.6279
6	12	0.5	997.561	0.8991
7	12	2	696.135	2.943
8	12	2	997.561	4.208
M	10	1.25	846.848	2.615

Table H3 in the previous page shows the displacement response for each design point in the full factorial design. The trends arising from the results of the full factorial design show an increase in displacement as diameter decreases, velocity increases, and as density increases. However, as shown in table H3, there is a discrepancy between the displacement values of design point 1 and 2. As density increases from design point one to design point two, displacement decreases. Further insight into this discrepancy is discussed in the “Discussion of Results” section.

The interactions between the three inputs are illustrated in figure H4. The discrepancy previously discussed at design point 1 and 2 causes an intersection between densities when looked at from the fluid velocity perspective.

DOE Model Evaluation

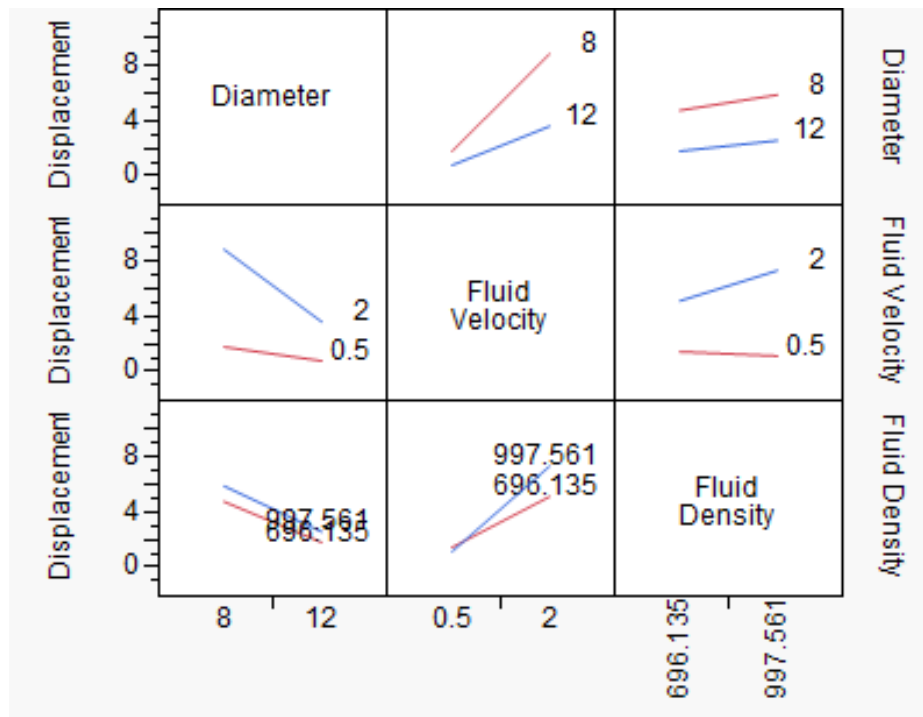


Figure H4: Interaction Results of the Full Factorial Design from JMP

Surface Response Design (Box-Behnken):

The final model used for this computational experiment was surface response design based on the Box-Behnkin. As mentioned in table 3.4, the advantage of surface response designs is the ability to interpret nonlinear responses throughout the design space.

DOE Model Evaluation

Table H4 shows the displacement response for each design point in the Box-Behnken design.

Table H4: Design Points and Displacement Results from the Surface Response Design

Run	Pattern	Pipe Diameter (in.)	Fluid Velocity (m/s)	Density (kg/m ³)	Displacement (in.)
1	--0	8	0.5	846.848	1.133×10^{-2}
2	-+0	8	2	846.848	8.801×10^{-2}
3	+ -0	12	0.5	846.848	0.7626×10^{-2}
4	++0	12	2	846.848	3.573×10^{-2}
5	0--	10	0.5	696.135	0.7458×10^{-2}
6	0-+	10	0.5	997.561	1.066×10^{-2}
7	0+-	10	2	696.135	4.855×10^{-2}
8	0++	10	2	997.561	6.951×10^{-2}
9	-0-	8	1.25	696.135	3.412×10^{-2}
10	+0-	12	1.25	696.135	1.699×10^{-2}
11	-0+	8	1.25	997.561	4.888×10^{-2}
12	+0+	12	1.25	997.561	2.429×10^{-2}
13	000 (midpoint)	10	1.25	846.848	2.615×10^{-2}

The interactions between the three inputs are illustrated in figure H5.

DOE Model Evaluation

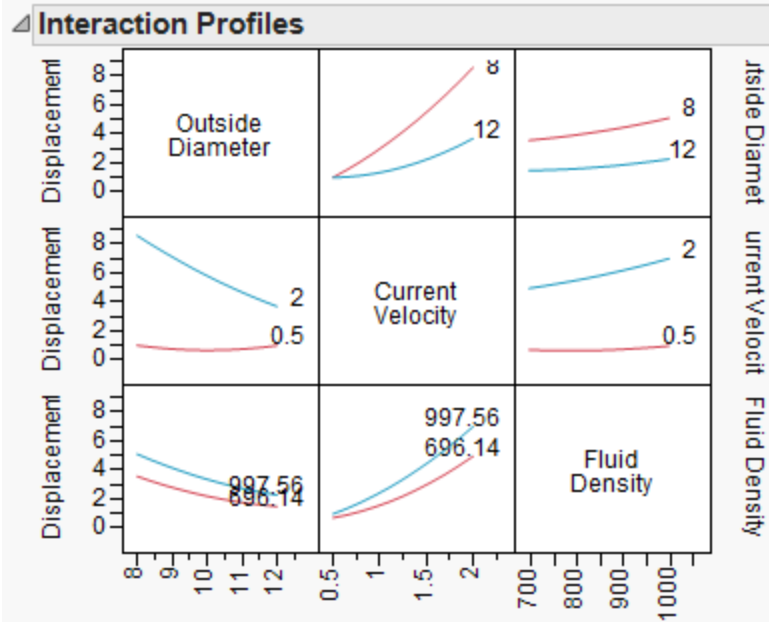


Figure H5: Interaction Results of the Box-Behnkin Design from JMP

The Table H5 shows the maximum and minimum values of displacement obtained from the JMP software results for the Box-Behnkin design. These values will be compared to the maximum and minimum results from the other two DOE models (full factorial at the corners and space-filling response).

Table H5: Maximum and Minimum Displacements from the Box-Behnkin Design Results

Value	Displacement (in)
Maximum	9.935×10^{-2}
Minimum	1.219×10^{-2}

Best Design Model for this Experiment

According to the findings, the best design model of the three chosen is the Box-Behnken Surface Response Design due to its ability to determine the nonlinearity of response along the range of each input. Figure H6 validates this reasoning, for the confidence levels (i.e. the blue lines in figure H6) are close to the predicted values of displacement; in addition, curvature is noticeable in this prediction profiler.

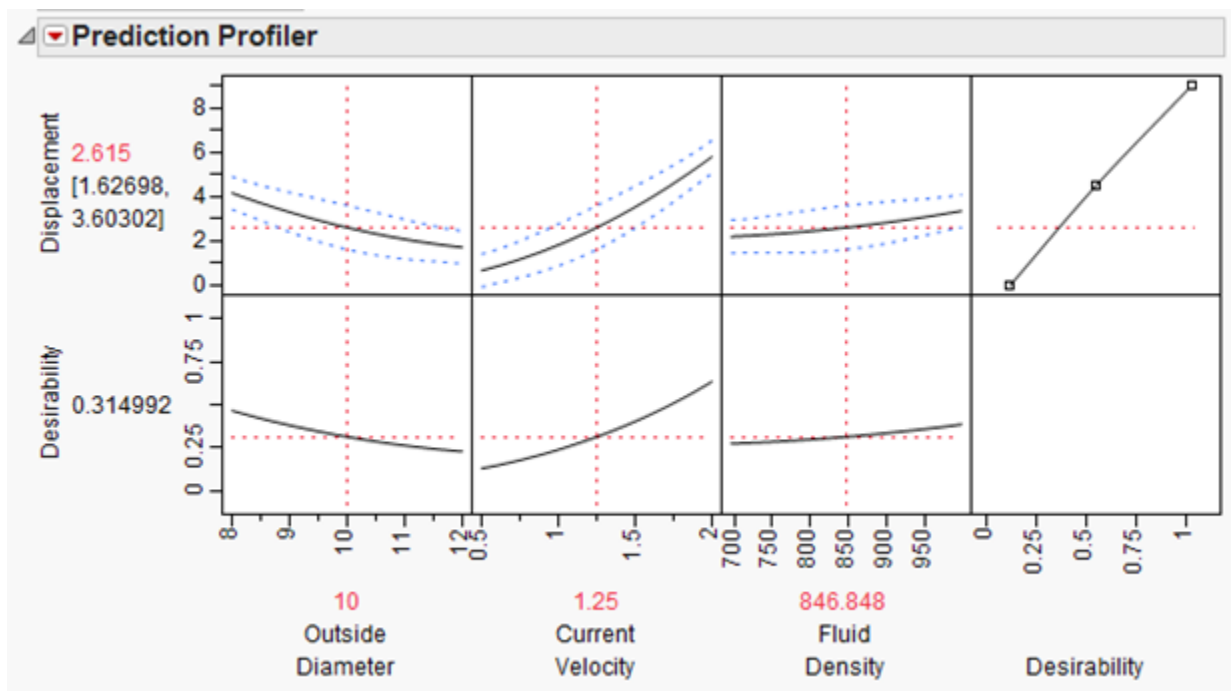


Figure H6: The Prediction Profiler of the Box-Behnken Design from JMP

Maximum and minimum displacements were found at the corners for the space-filling design and the Box-Behnken designs and compared to the maximum and minimum displacement found at the same corners in the full-factorial design. The minimum displacement value for the Box-Behnken Design at 8.621 % error was closer than the space-filing design at 55.43 % error; in addition, the maximum displacement value for the Box-Behnken Design at 4.102 % error was much closer to the actual value than the space-filling design at 50.91% error.

Illustration of Input Ranges for Final Box-Behnken DOE

Entrench Depth Input:

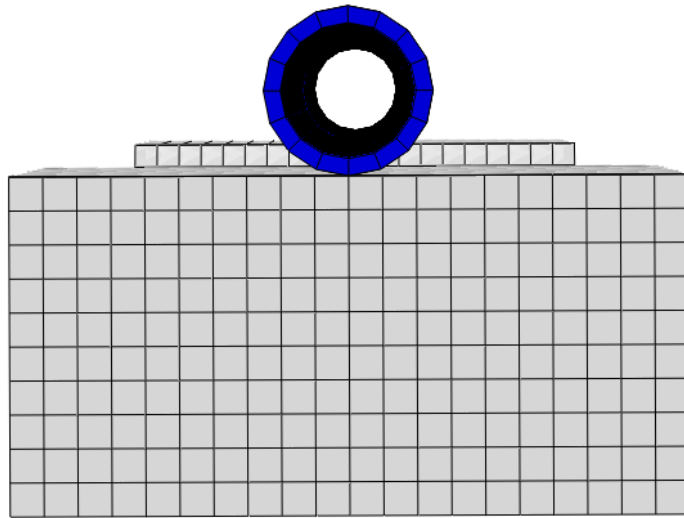


Figure I1: Pipe Initially on Top of Soil

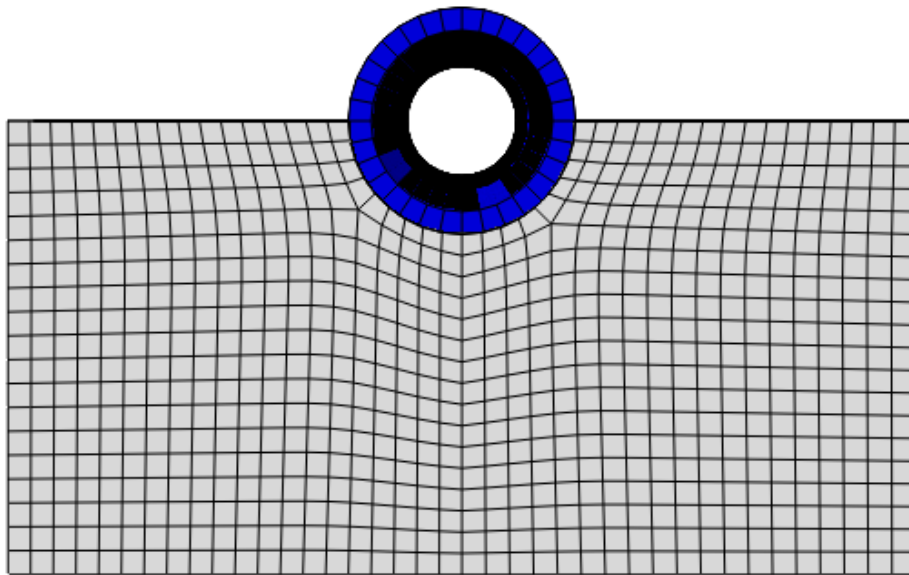
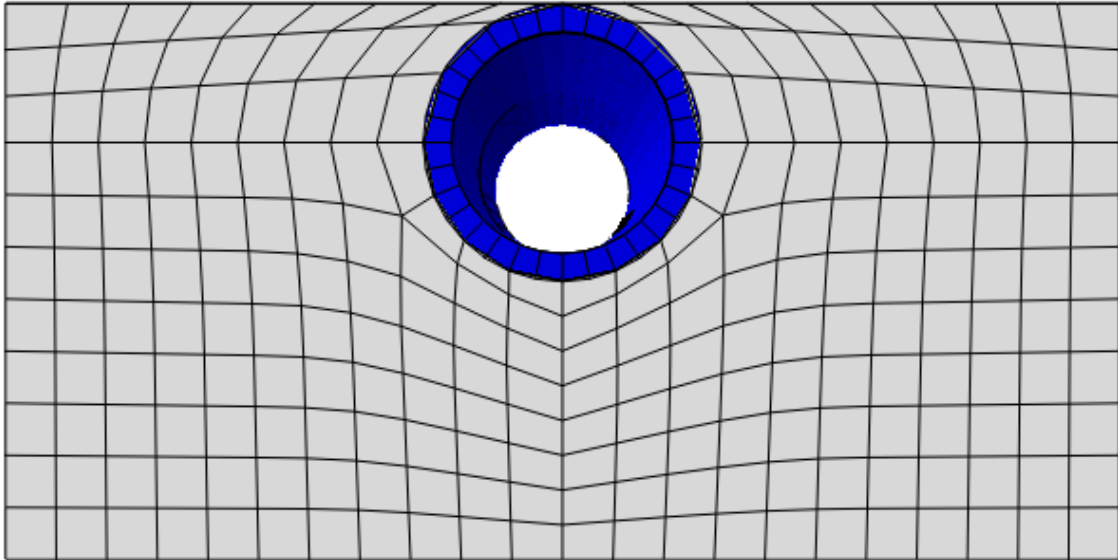


Figure I2: Pipe Initially Half Entrenched in Soil

Illustration of Input Ranges for Final Box-Behnken DOE

Figure I3: Pipe Initially Fully Entrenched in Soil



Amount of Soil Contact with Pipe Input:



Figure I4: 20x Soil Contact with Pipe



Figure I5: 110x Soil Contact with Pipe



Figure I6: 200x Soil Contact with Pipe

Detailed Final Box-Behnken DOE Results

BB Run 1	200xSoil Contact - Pipe half entrenched (low density)			
Trial	Run Time (hours)	Max VM Stress (x10 ³ psi)	Max Principle Stress (x10 ³ psi)	Location
1	4.5833	1.39702		Near Mid-Boundary Condition
		1.09046		Near End of Span
		0.712644	0.717157	At Effective Length Location (approx. 200 in from end)
BB Run 2	200xSoil Contact - Pipe on Top of Soil (Mid Density)			
Trial	Run Time (hours)	Max VM Stress (x10 ³ psi)	Max Principle Stress (x10 ³ psi)	Location
1	1.1333	1.82636		Near Mid-Boundary Condition
		1.56701		Near End of Span
		0.930867	0.933286	At Effective Length Location (approx. 200 in from end)
BB Run 3	20xSoil Contact - Pipe on Top of Soil (Mid Density)			
Trial	Run Time (hours)	Max VM Stress (x10 ³ psi)	Max Principle Stress (x10 ³ psi)	Location
1	0.6167	0.804392		Near Mid-Boundary Condition
		1.50928		Near End of Span
		0.805825	0.801518	At Effective Length Location (approx. 20 in from end)
BB Run 4	110xSoil Contact - Pipe on Top of Soil (High Density)			
Trial	Run Time (hours)	Max VM Stress (x10 ³ psi)	Max Principle Stress (x10 ³ psi)	Location
1	0.7333	0.735058		Near Mid-Boundary Condition
		1.18768		Near End of Span
		0.259806	0.233492	At Effective Length Location (approx. 110 in from end)
BB Run 5	200xSoil Contact - Pipe Fully Entrenched- Mid Density			
Trial	Run Time (hours)	Max VM Stress (x10 ³ psi)	Max Principle Stress (x10 ³ psi)	Location
1	22.5	1.19246		Near Mid-Boundary Condition
		0.99774		Near End of Span
		0.635267	0.616354	At Effective Length Location (approx. 200 in from end)
BB Run 6	200xSoil Contact - Pipe Half Entrenched (High Density)			
Trial	Run Time (hours)	Max VM Stress (x10 ³ psi)	Max Principle Stress (x10 ³ psi)	Location
1	4	1.41367		Near Mid-Boundary Condition
		1.04555		Near End of Span
		0.644866	0.648382	At Effective Length Location (approx. 200 in from end)
BB Run 7	110xSoil Contact - Pipe Half Entrenched (Mid Density)			
Trial	Run Time (hours)	Max VM Stress (x10 ³ psi)	Max Principle Stress (x10 ³ psi)	Location
1	17.5	0.607578		Near Mid-Boundary Condition
		1.13922		Near End of Span
		0.275151	0.276416	At Effective Length Location (approx. 110 in from end)
BB Run 8	110xSoil Contact - Pipe Fully Entrenched (Low Density)			
Trial	Run Time (hours)	Max VM Stress (x10 ³ psi)	Max Principle Stress (x10 ³ psi)	Location
2	4.8333	0.632943		Near Mid-Boundary Condition
		1.12689		Near End of Span
		0.262532	0.262814	At Effective Length Location (approx. 110 in from end)
BB Run 9	20xSoil Contact - Pipe Fully Entrenched (Mid Density)			
Trial	Run Time (hours)	Max VM Stress (psi)	Max Principle Stress (x10 ³ psi)	Location
1	4	0.782066		Near Mid-Boundary Condition
		1.14656		Near End of Span
		0.981805	0.954913	At Effective Length Location (approx. 20 in from end)

Detailed Final Box-Behnken DOE Results

BB Run 10	110xSoil Contact - Pipe Fully Entrenched (High Density)			
Trial	Run Time (hours)	Max VM Stress (x10 ³ psi)	Max Principle Stress (x10 ³ psi)	Location
2	4.833	0.627167		Near Mid-Boundary Condition
		1.11951		Near End of Span
		0.257326	0.257992	At Effective Length Location (approx. 110 in from end)
BB Run 11	20xSoil Contact - Pipe Half Entrenched (Low Density)			
Trial	Run Time (hours)	Max VM Stress (x10 ³ psi)	Max Principle Stress (x10 ³ psi)	Location
1	5	0.777659		Near Mid-Boundary Condition
		1.17712		Near End of Span
		0.985886	0.960699	At Effective Length Location (approx. 20 in from end)
BB Run 12	110xSoil Contact - Pipe on Top of Soil (Low Density)			
Trial	Run Time (hours)	Max VM Stress (x10 ³ psi)	Max Principle Stress (x10 ³ psi)	Location
1	0.75	0.741027		Near Mid-Boundary Condition
		1.19046		Near End of Span
		0.262185	0.261093	At Effective Length Location (approx. 110 in from end)
BB Run 13	20xSoil Contact - Pipe Half Entrenched (High Density)			
Trial	Run Time (hours)	Max VM Stress (x10 ³ psi)	Max Principle Stress (x10 ³ psi)	Location
1	15.5	0.777336		Near Mid-Boundary Condition
		1.17752		Near End of Span
		0.985086	0.959994	At Effective Length Location (approx. 20 in from end)

Drained vs. Undrained Conditions of Soil

Soil can be divided up in two categories: drained and undrained. The Triaxial test was created for the purpose of testing the drained and undrained conditions of soil. The Triaxial test apparatus used for this testing is pictured in the figure below:

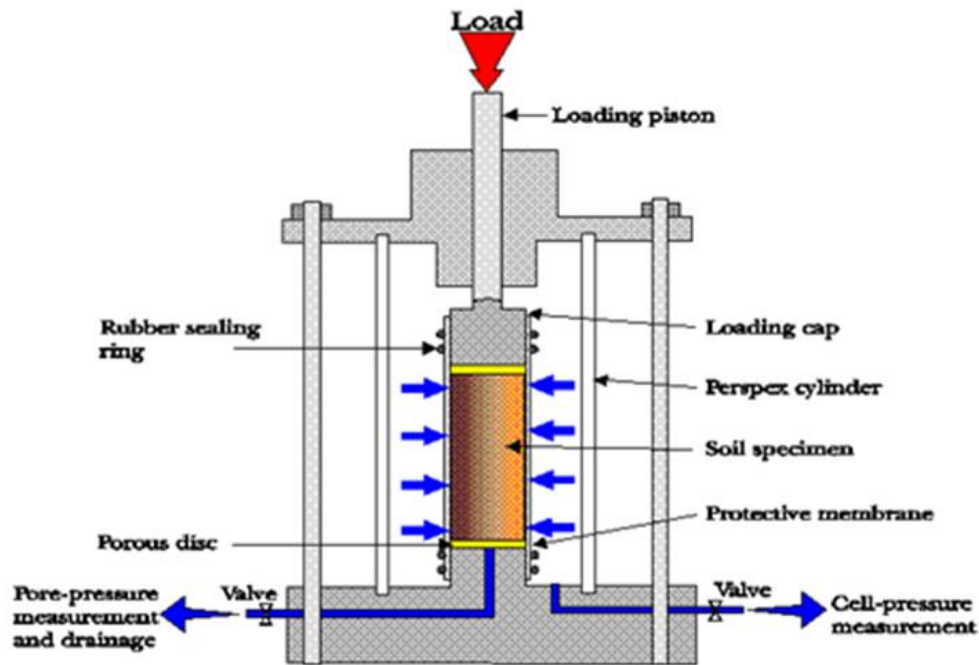
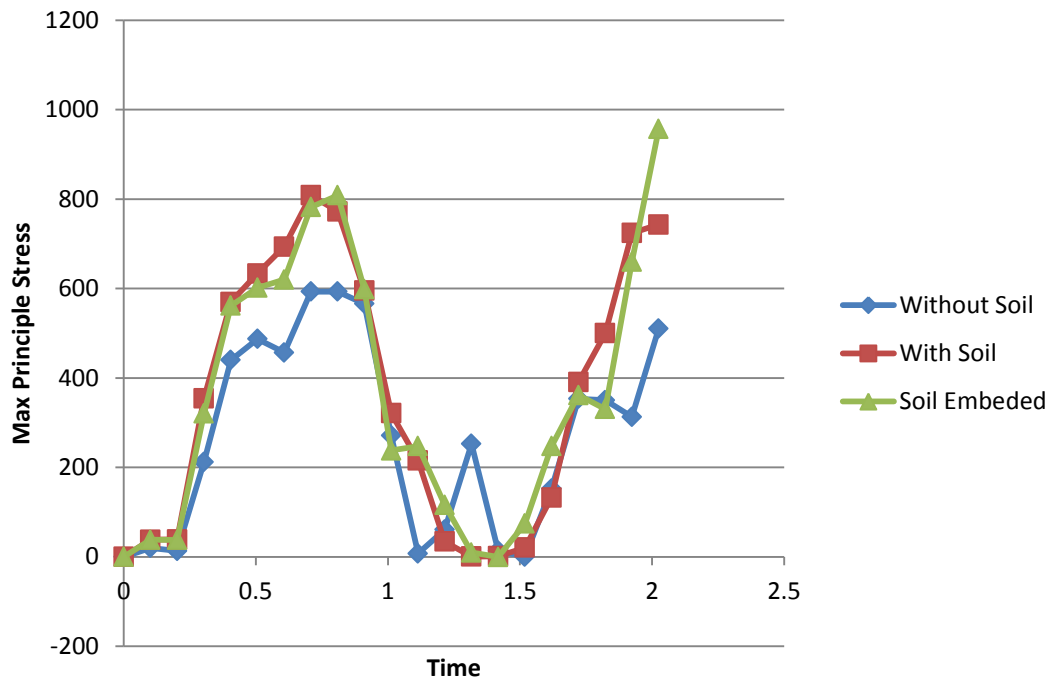


Figure K1: Triaxial Apparatus
www.environment.uwe.ac.uk

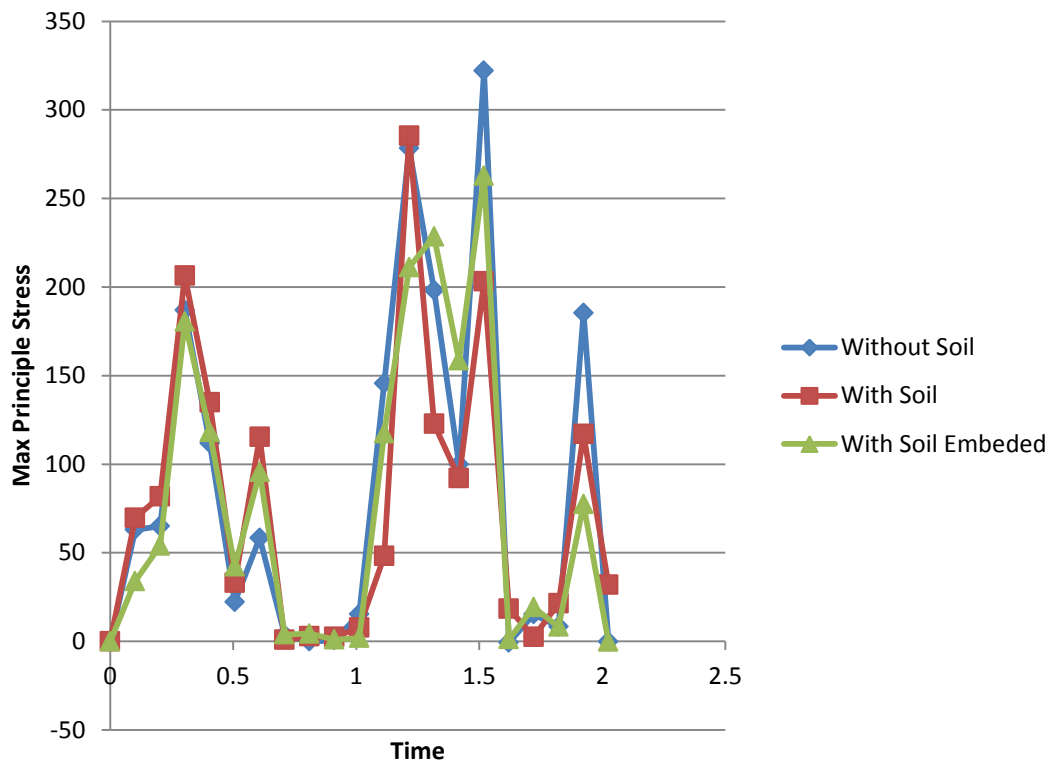
The Triaxial test apparatus has valves on the side to allow water to escape the test chamber as the load is applied from the loading piston. If the valves are closed, the soil conditions are said to be undrained. If the valves are open, the soil conditions are said to be drained, for water is allowed to be drained out of the test chamber. Sand is modeled under drained conditions due to its permeability (i.e. the permeability does not allow fluid to become entrapped in the sand). Clay is modeled under undrained conditions, for clay does not have the level of permeability as sand and entraps the fluid within itself in the short-term. For long-term periods, clay should be modeled with drained conditions.

Validation of Soil Effects

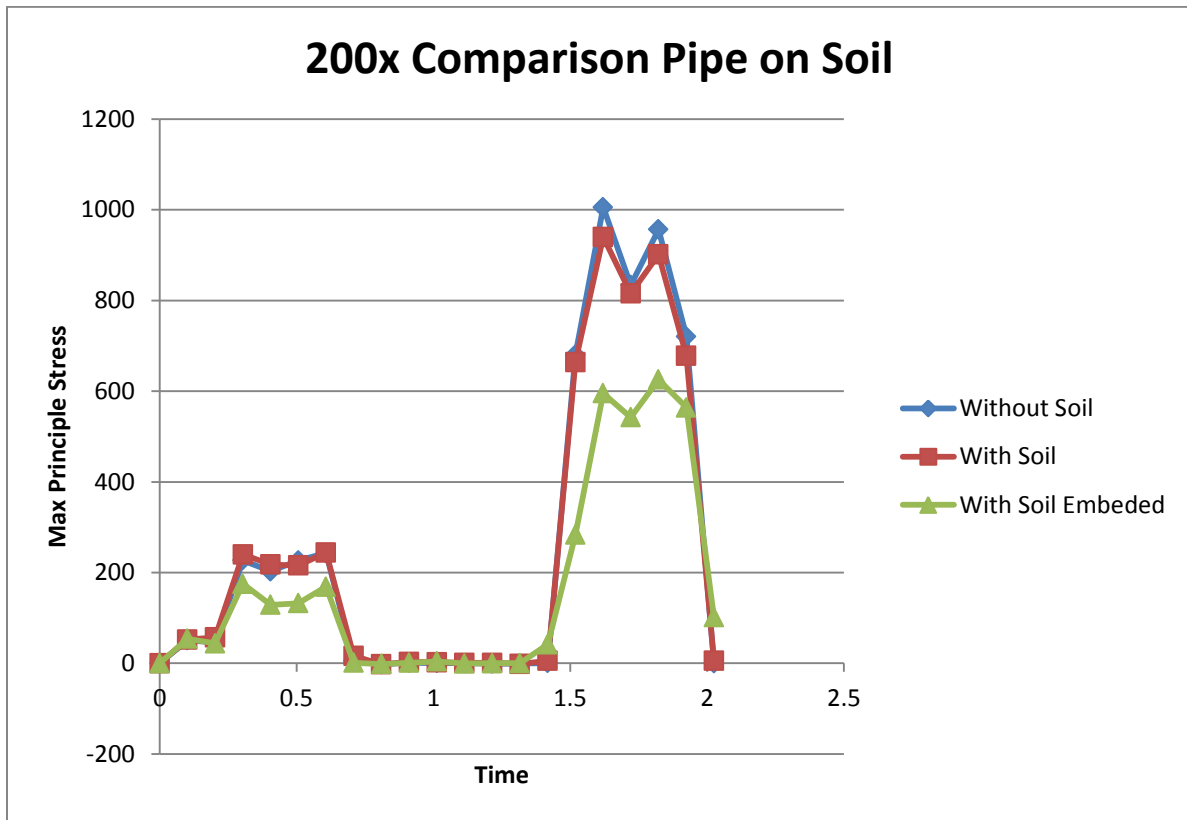
20x Comparison Pipe on Soil



110x Comparison Pipe



Validation of Soil Effects



Limitations of the Mohr-Coulomb Model

The Mohr-Coulomb Model has several limitations, which include:

- 1.) It assumes an elastic-perfectly plastic relationship:

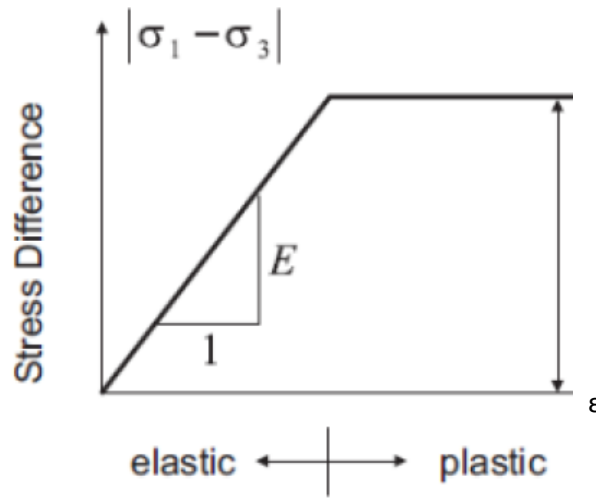


Figure M1: Elastic-Perfect Plastic Relationship

<http://www.civil.utah.edu>

- a. This relationship may not realistically predict the plastic deformation of clay and sand.
- 2.) Does not model the void ratios within the model.
 - a. It is difficult for any model to predict the pockets of void and/or fluid within soil.
- 3.) Does not take into account the direction of flow deformation of the soil
- 4.) The Mohr-Coulomb model predicts continuous dilation.